New Analytical Tools for Native Mass Spectrometry and Ion Mobility Mass Spectrometry Analysis of Intact Proteins

Seoyeon Hong

A dissertation

submitted in partial fulfillment of the

requirements for the degree of

Doctor of Philosophy

University of Washington

2020

Reading Committee:

Matthew F. Bush, Chair

Robert E. Synovec

Frantisek Tureček

Program Authorized to Offer Degree:

Chemistry

University of Washington

Abstract

New Analytical Tools for Native Mass Spectrometry and Ion Mobility Mass Spectrometry Analysis of Intact Proteins

Seoyeon Hong

Chair of Supervisory Committee:

Associate Professor Matthew F. Bush

Department of Chemistry

Native mass spectrometry (MS) is a structural biology tool that probes proteins and protein complexes in the gas phase. In native MS, electrospray ionization (ESI) of protein samples are prepared in nondenaturing conditions and generate "native-like" protein ions, which retain noncovalent interactions observed in solution. Therefore, native MS is useful to provide information about the stoichiometry, topology, and ligand binding of protein complexes. Native MS coupled with ion mobility (IM) provides the momentum transfer collision cross section (**Ω**), which is indicative of the size and shape of ions. Collision-induced unfolding (CIU) is an energy-dependent IM-MS technique that probes the unfolding of protein structures monitored by **Ω** as a function of energy. This dissertation explores the utility of native MS and IM-MS analysis to study protein complexes. First, native MS analysis is used to investigate the stoichiometry of iron and sulfur in the endogenous Fe-S clusters binding to the F-box and leucine-rich protein 5

(FBXL5) and Skp1 from the Skp1-Cul1-Fbox (SCF) ubiquitin ligase in Chapter 2. The thermal activation in solution prior to ESI in combination with instrumental activation effectively elucidates the binding of [2Fe-2S] to FBXL5-Skp1 by reducing the presence of nonspecifically binding adducts (NSA).

The effects of polarity on native-like avidin tetramers are characterized using native MS and IM-MS analysis in Chapter 3. The native MS of native-like avidin tetramer shows that the average charge state distribution is different between the cations and the anions. The native IM-MS results show that the Ω of native-like avidin tetramer is similar regardless of the charge state and polarity. However, the CIU results display differences due to the charge state and polarity. In particular, the differences between the CIU results of 14+ and 14− avidin ions indicate that CIU analysis of the avidin ions is sensitive to solely polarity. In order to quantitatively compare the CIU results of 14+ and 14− avidin ions, a similarity score is developed. Similarity score analysis comparing the 14+ and 14− ions indicates that the largest difference in Ω is observed at near 800 eV, while the greatest similarity is observed at low energy range (56 to ~400 eV).

The utility of native MS and IM-MS analysis is explored to characterize antibodies (Abs) using two IgG2 samples (^{S}IgG2 and ^{A}IgG2) in Chapter 4. These two samples are from the same subclass (IgG2), have the κ light chain and were each purified from human myeloma plasma, but were from different manufacturing origins. Native MS results of the two samples indicate that the two Abs display vastly different apparent mass (^{S}IgG2: ~154 kDa and ^{A}IgG2: 157, 159 kDa respectively) and the relative mass heterogeneity based on the peak width and shape. The IM-MS analysis demonstrates that the Ω of the native-like Abs depends on the *z*, which contrasts from the Ω of most proteins. The strong dependence of Ω on *z* may be due to large differences in structural populations and/or the presence of flexible hinge region. The CIU analysis of ^{S}IgG2

and ^{A}IgG2 demonstrates that the greatest difference in Ω between the two Abs is present at low energy with greater difference for anions than for cations. Overall, these results indicate that anions and low energy may preferentially provide significant differences when comparing similar proteins using native IM-MS and CIU analysis.

Collision-induced unfolding (CIU) is increasingly used to study the effects of ligand binding to proteins and protein complexes. In chapter 5, a workflow is developed to more accurately assess the effects of ligand binding on the CIU stability. Mass spectra of the quadrupole-selected precursor ions at varying collision-energy display signals indicate that the precursor ions for CIU analysis is interfered by the presence of NSA despite extensive buffer exchange. Therefore, $S_{relative}$ method is developed to determine the minimum collision-energy threshold at which all of the apparent NSA are removed from the initial *m*/*z* window of the precursor ions. More generally, $S_{relative}$ may be used for quality control of CIU analysis.

Dedication

To God in heaven, my family and friends.

Acknowledgements

Graduate school has been an incredible chapter of my life that helped me grow a lot as a person and a scientist. First, I would like to thank my advisor, Prof. Matthew F. Bush, for providing consistent guidance as my mentor for these past five years. When I first decided to pursue my research interest in mass spectrometry, I knew very little to nothing about mass spectrometry. Matt provided me opportunities to learn and grow as a scientist with a great deal of freedom. In addition, I would like to thank Prof. Rebert Synovec, Frantisek Turecek, Ashleigh Theberge, Gabriele Varani, and James Bruce for serving as my current and/or past academic committees. It was very evident that they were excited about my research. The questions and feedback that I have received from my committee members were truly insightful and tremendously helped my graduate research.

I would also like to thank Prof. Rachel Klevit (Department of Biochemistry at UW) and present or past fellow graduate students, Christ Wood (Department of Biochemistry at UW) and Scott Delbecq (Department of Biochemistry at UW). I have received mammalian small heat protein (HSPB5) samples that were used for my research described in Chapter 5. Additionally, they provided insights into important considerations for the experiments.

I would like to thank Prof. Ning Zheng (Department of Pharmacology at UW) and a senior scientist in the Zheng group, Dr. Hui Wang (Department of Pharmacology at UW). They provided their scientific insights and biological samples (Fbox-Skp1) used for my research in Chapter 2.

Many members of the chemistry department at UW have helped over the past years. I would like to thank Christine Gormley (Graduate Program Advisor) for helping me organize administrative duties for my thesis defense. I would like to thank Diana Knight (Assistant to the

Chair) for kindly answering many questions since the beginning of my graduate program and also giving me the opportunity to write articles for the quarterly Chem Letter for the department. I thank Lochlan Hickok (Chemistry Research Stockroom Manager) for his help with getting the shipments and also always kindly helping me with any questions about the stockroom items, the cold room and the chemical inventory. I would like to thank Thomas Leach (former laboratory technician) for helping me teach CHEM 321 for several quarters and for being such a supportive colleague and for willingly reading my manuscript. I would like to thank Martin Sadelik (Facility Manager) for teaching me how to use the mass spectrometers in the core facility for CHEM 428 for several quarters and for organizing the Pacific Northwest Mass Spectrometry Group, PacMass. I would also like to thank Krista Holden (previous Graduate Program Coordinator), Ashley Zigler (previous Graduate Program Coordinator), Kimberly Quigley (Director of Personnel), Gretchen (Littell) Shauger (Payroll Coordinator) and Hong Sze (Travel and Reimbursements) for answering my administrative questions.

I would like to give thanks to all of the current and past members of the Bush lab. I was fortunate to be a part of such a positive and supportive lab. I want to highlight some of the members who have helped me immensely during my graduate career. I sincerely thank Kimberly Davidson for being such a kind and helpful senior graduate student who taught me how to use G2 instrument and helped troubleshooting many experiments using G2. I enjoyed much needed coffee breaks with Kim. I would like to thank Samuel Allen for answering a lot of my questions about how to use the G2 instrument. I am also grateful for Sam's critical insights into my research. I am inspired by his dedication and excitement about science. I would like to thank Ken Laszlo for passing down a wealth of knowledge about mass spectrometry by introducing many useful articles. Ken also provided useful insights into how to adjust the G2 instrument settings

that are optimal for my experiments when I first joined the lab. I was inspired by Ken's enthusiasm for science as well as his experiences and perspectives toward research as a senior graduate student. I would like to thank Meagan Gadzuk-Shea for helping me with cation-to-anion-proton-transfer (CAPTR) experiments for my research and for sharing insights into how to troubleshoot the size exclusion chromatography instrument. Also, I am grateful to Meagan for letting me pet or feed Misa. I would like to thank Rae Eaton for initiating many coffee breaks, for being a great of example of work ethic and passion for science, for helping me realize the importance of communicating science or my research and for voluntarily bringing baked goods to support the members of the Bush lab including me on many occasions. I would like to thank Daniele Canzani for frequently helping me to open the gas cylinder, for sharing collaborative efforts to troubleshoot the G2 instrument particularly when the pump malfunctioned for a period of time and for bringing amazing donuts to the lab. I would like to thank Theresa Gozzo for exchanging research knowledge about monoclonal antibody, for kindly writing a protocol for CAPTR experiments and for her example of hard work and excitement about science.

I would like to thank Dr. Paul Agris (advisor at University at Albany) who mentored me prior to joining the graduate program at UW chemistry. He offered nothing short of full support, encouragement and opportunities to learn and grow as a scientist.

I have been surrounded by so many amazing individuals in my personal life. I would like to express my gratitude for God in heaven for providing me for everything and for being so faithful all the time. I would like to thank my parents. They have been an inspiration of great work ethic and pursuing a higher education.

I have been blessed with many friends who have been supportive of me during my graduate careers. I would like to thank a few amongst many: Nikki Carter, Shenea Crawford,

Sara Felushko, Noelle Everage and Myriam Pierre. Thanks for being great friends, having fun times together and giving me a lot of support.

Nomenclature

Ab	Antibody
CAPTR	Cation-to-Anion Proton Transfer Reaction
CID	Collision-Induced Dissociation
CIU	Collision-Induced Unfolding
Da	Dalton, the unified atomic mass unit
DC	Direct Current
DT	Drift tube, in reference to ion mobility instrument
e	elementary charge, 1.6021766208(98) x 10^{-19} C
E	Electric Field
$E{\cdot}P^{-1}$	drift field strength: electric field divided by pressure, V·cm^{-1}·Torr^{-1}
ESI	Electrospray Ionization
Fe:S	Stoichiometry of Fe and S in Fe-S cluster
Fe-S	Iron-sulfur cluster
H	Proton
He	helium, in reference to IM buffer gas
IgG	Immunoglobulin G
IM	Ion Mobility
k_B	Boltzmann's constant, 1.38064852(79) x 10^{-23} J·K^{-1}
m/z	mass-to-charge ratio, the standard measurement unit in MS
mAb	Monoclonal antibody
MS	Mass Spectrometry
nESI	nano-electrospray ionization

NSA	Nonspecifically binding adducts
rf	Radio-Frequency, referring to the frequency of AC potentials
t_D	drift time
ToF	time-of-flight, an MS analyzer
z	ion charge state
μ	reduced mass, often between ion and neutral masses
Ω	momentum transfer collision cross section
$\widetilde{\Omega}$	Median collision cross section

Table of Contents

Chapter 1: Introduction

1.1 Mass Spectrometry

Mass spectrometry (MS) separates gas-phase ions based on mass-to-charge ratio (*m*/*z*). Typically, a mass spectrometer consists of at least an ion source, a mass analyzer and a detector. Matrix assisted laser desorption ionization (MALDI) (1) and electrospray ionization (ESI) (2, 3) are soft ionization techniques that are commonly used for MS analysis of biomolecules. MS analysis of biomolecules benefits from relatively high speed, sensitivity, and selectivity. Samples for most MS analyses are prepared in denaturing solvent (*i.e.*, acidified or organic solvent). The ionization of MALDI typically involves a dry analyte on a crystallized metal plate (matrix) consisting of small organic compounds (*e.g.*, nicotinic acid) and a laser that irradiates the analyte on the matrix (4). Ions formed from MALDI are typically singly charged (z=1).

ESI transfers ions directly from the liquid phase. An electrical circuit is established between an ESI capillary and the mass spectrometer. A voltage is applied to the sample containing the analyte placed in the capillary. The potential bias (between the capillary and the nearby electrode, *e.g.*, the sampling cone) causes the emission of a highly charged jet, called a Taylor cone (5) at the tip of the capillary, which breaks into a spray of charged droplets (6) containing the analyte. Through a series of solvent evaporation and coulombic fission (7), multiply-charged ions in the gas phase are generated (2, 3). Though the exact mechanisms of ESI remain elusive, the ion emission model (8, 9) generally describes low molecular weight ions, the charged residue (9, 10) and combined charge-residue and field emission models (11–13) are attributed to large globular ions such as proteins, and disordered polymers are related to chain ejection models (9). The multiply charged protein ions from ESI are detected in a relatively low *m*/*z* range (compared

to singly charged ions) and are amenable for most mass analyzers, making ESI a well-suited ionization technique for the analysis of biomolecules.

1.2 Native Mass Spectrometry

1.2.1 Native Mass Spectrometry of Biomolecules

In native MS, native-like gas phase ions are generated from ESI or nanoelectrospray ionization (nESI) of samples prepared using nondenaturing solvent such as aqueous ammonium acetate. In native-like protein ions, noncovalent interactions from solution are preserved including stoichiometry (14–16), ligand binding (14–16), dynamics and topology (17–19) in solution. In particular, native MS is useful for providing insights about proteins and protein complexes that are too small, large (20–22), heterogeneous (20, 22), dynamic (21, 22), or have low copy numbers (23), which are properties that can make these analytes unamenable to conventional structural biology techniques *e.g.*, nuclear magnetic resonance, X-ray crystallography, cryo-electron microscopy. For example, the Norwalk virus capsid (or also known as Norovirus) has a large molecular weight (in MDa range) and can form multiple populations. The native MS results of the Norwalk virus capsid provides insights into the intact assembly that consists of 180 and 240 monomers, which corresponds to 3 and 4 MDa respectively (20).

Native MS analysis of proteins and protein complexes displays lower and narrower charge state distributions compared to MS analysis of proteins under denaturing conditions (24–30). The relatively low and narrow charge state distributions are partly attributed to the folded conformations accompanied by limited access to the ionizable sites (*e.g.*, basic sites or acidic sites) (31–34) and increased charge stabilizing interactions such as hydrogen bonding (33) and salt-bridges (33) by the folded three-dimensional structures. As a comparison, ions generated

from denaturing conditions display higher charge states of most protein ions and the higher charge states are associated with unfolding of protein structures via coulombic repulsion (25).

1.2.2 Noncovalent Interactions with Small Ligand Interactions

Ligand binding to proteins and protein complexes plays an important role in the stability, structure and function of proteins (35–38). Native MS of protein-ligand complexes has been used to determine the identity of ligands (39–41), the relative or direct thermodynamic parameters such as K_d and K_a (14, 15, 42, 43), and stoichiometry (44). Optimal sample preparation (*e.g.*, purification (45) or titration (45, 46)) and accurate mass measurement may enhance the MS analysis of ligand binding. For instance, MS analysis of insulin titrated with Zn(II) and phenol at pH 8.0 showed that the insulin hexamer ions are formed via chelation of Zn(II) and phenol. The accurate mass measurement unambiguously determined the stoichiometry of two Zn(II) binding (atomic mass of Zn(II): 65.38 Da) per one hexamer insulin (mass of insulin hexamer: 34.6 kDa) consistent with solution and crystal structures (46). Additionally, ESI-Fourier-Transform Ion Cyclotron Resonance (FTICR)-MS analysis exhibits mass resolution of 1 Da accuracy and was used to determine the oxidation state of [4Fe-4S] binding to the high potential iron-sulfur protein (HiPIP) from *Chromatium vinosum* (*C. vinosum*) by determining the number of protons and the charge state of the apo and holo HiPIP (47).

In addition to specifically binding ligand interactions, nonspecifically binding ligand interactions are observed within the native-like gas phase protein ions. In native MS, nonspecifically binding ligands are often nonvolatile buffer molecules or adducts (*e.g.*, Na^+, K^+) attributed to insufficient buffer exchange or inevitable exposure to a surface containing the adducts. Nonspecific binding interactions are induced during the ESI (48). The extent of nonspecific interaction depends on the size of the droplets formed from ESI (48, 49), the

electrospray current (48), and the flow rate (48). The presence of nonspecifically interacting adducts may exhibit signals at the same or similar *m*/*z* values as protein-ligand complexes of interest and so may interfere with the MS analysis.

Instrumental activation is useful to remove nonspecifically binding adducts and to study protein-ligand complexes (50). For example, the ligand binding study of the deglycosylated antigen-binding groove of recombinant soluble human cluster of differentiation 1 protein (shCD1b) was hindered by nonspecific binding interactions at low desolvation energy (44); however, the endogenous ligands, phosphatidylcholine (PC) and unknown ligands (UL), were identified upon increasing activation energy. Alternatively, mathematical frameworks have been developed to probe ligand binding interactions despite the interference by nonspecific binding (15, 51). For instance, El-Hawiet et al.(15) reported a combined mathematical-experimental framework, namely, the *proxy protein* ESI-MS method, which implements competitive ligand binding to determine the association constant (K_a) for specific binding interactions directly from ESI-MS.

1.3 IM-MS

1.3.1 First Principles of IM

Ion mobility (IM) separates ions based on their size, shape and charge (52). In IM, ions under the influence of an applied electric field traverse an IM cell filled with a neutral background gas (*e.g.*, N_2 or He) (53). The key outputs from an IM measurement are the mobilities of the ions. Based on the theory reported by Mason and McDaniel et al. in 1988 (54), the mobility of an ion is related to the momentum transfer collision cross section, **Ω**, of the interactions between the ion and a background gas molecule, which approximates the projected surface area of an orientationally averaged ion-neutral pair.

In drift tube (DT) IM, the IM cell consists of stacked ring electrodes throughout which a constant electric field is applied (53). The constant electric field enables direct measurement of the mobilities of ions derived from the drift time. In DTIM, ions are pulled by the electric field along the axis towards detection but this is balanced by a drag force of the same magnitude in the opposite direction due to collisions and momentum transfer to the gas molecules. As a result, the ions reach a constant steady-state velocity (v_D), and they are separated by their shape, size, and charge. For example, ions with extended conformations display longer drift times than those with compact conformations due to greater interactions with the background gas molecules.

1.3.2 Ω Calculation using DTIM

The Ω may be determined using DTIM results from multiple field strengths (55) or a single-field strength (55). In this report, all Ω are obtained using multiple field strengths; therefore, the following describes the determination of Ω using multiple field strengths. The steady-state velocity (v_D) of the ions is as the following:

$$v_D = KE = K\frac{V}{L} \tag{1.1}$$

where *K* is the mobility of the ion, *E* is the field strength, which is equal to the applied drift voltage (*V*) over a specific length of the drift tube (*L*). Since the v_D is $\frac{L}{t_D}$ where t_D is the experimentally measured drift time of the ion, equation (1.1) is rearranged as the following:

$$t_D = \frac{L^2}{K}\frac{1}{V} \tag{1.2}$$

K is independent of applied drift voltage within the low field limit (54); therefore, the linear regression of t_D as a function of $\frac{1}{V}$ over a range of *V* results in the slope, $\frac{L^2}{K}$ (equation 1.2). The *K* is used to determine the Ω using the Mason-Schamp equation (54) as the following:

$$\Omega = \frac{3ez}{16N}\left(\frac{2\pi}{\mu k_B T}\right)^{1/2}\frac{1}{K} \quad (1.3)$$

where *e* is the elementary charge, *z* is the charge of the ion, *N* is the buffer gas density, μ is the reduced mass of the ion and the neutral buffer gas, k_B is the Boltzmann constant and *T* is the temperature of the drift-gas.

1.3.3 Mass Analyzers used for IM-MS

IM coupled with MS provides an additional separation dimension (56, 57). In addition, the IM-MS analysis has been used as a structural biology tool to study intact protein systems using Ω since the 1990s (58). To date, IM has been coupled with several types of mass analyzers (59) including magnetic sector instruments (60, 61), quadrupoles (62), Time-of-flight (ToF) (63, 64), and more recently, ion traps (65) and FTICR (66). The quadrupole mass analyzer prior to IM-MS analysis enables a selection of ions of a specific *m*/*z* range prior to the IM analysis (67, 68) and enhances IM-MS analysis of complexed intact proteins (*e.g.*, intact analysis of cell). Most IM devices are coupled to ToF mass analyzers due to the short time scale (μs) per ToF cycle that enables several hundreds of mass spectra per IM cycle (typically, in ms timescale). Additionally, ToF is suitable for efficient sampling for continuous ionization methods such as ESI (69).

1.3.4 Instrumentation

One of the first commercial IM-MS instruments was the Waters Synapt HDMS commercialized in 2005 (70). The commercial Synapt HDMS consists of an ion source, quadrupole, trap cell, traveling wave ion mobility (TWIM) cell, transfer cell, and a ToF. TWIM comprises a stacked ring ion guide in which opposite phases of radio-frequency (rf) voltages are applied to adjacent ring electrodes, confining ions that would otherwise likely spread radially

(71). A direct current (DC) potential pulse is superimposed with rf, and the combination of DC and rf generates a moving electric field or T-wave (71). TWIM effectively separates intact protein complexes (72). The Ω is determined based on the calibration of ions with the known Ω using TWIM (73).

The commercially available Synapt G1 HDMS has been modified by replacing the TWIM with an rf-confining drift cell in order to directly measure the absolute Ω (74). The IM-MS results in this book are acquired from the Waters Synapt G2 HDMS with the rf-confining DT (75). The current DTIM incorporates a uniform DC gradient and alternating rf current (relative to the adjacent electrode). The rf current confines the ions into the center and increases their transmission. The effects of the electrodynamics (*e.g.*, the rf, range of *E*/*P* and inner diameter (i.d.) electrodes) of the rf-confining drift cell on the effective temperature, transmission, and drift time provide insights into the optimal conditions to directly measure the mobilities of ions and thus the absolute Ω of native-like proteins (74–76).

1.4 Native IM-MS

In Native IM-MS analysis, Ω are measured under native-like conditions *i.e.* the samples are prepared with nondenaturing solution and/or no thermal and kinetic activation by the instrumental conditions. The Ω obtained from native IM-MS analysis provides insights into the size and shape of proteins and protein complexes (52, 77). For instance, the Ω of native-like tryptophan RNA binding protein (TRAP) is consistent with the Ω derived from x-ray crystallography (78). Typically, charge state or polarity do not affect the Ω of native-like proteins for most globular proteins from small to large sizes (30) and non-globular proteins such as the pentameric serum amyloid P (SAP) containing a large central cavity (34).

1.5 Energy Dependent IM-MS

1.5.1 Mechanism of CIU of Protein Ions

Collision-induced unfolding (CIU) is a slow heating method that has been used to study the unfolding of protein ions in the gas phase. CIU enables gas phase ions to overcome the energy barriers to access various free energy landscapes of folding and unfolding (79) which are associated with Coulombic repulsion and structural components of the ions (80). In CIU, selected ions are accelerated into the trap cell containing background gas molecules at varying trap injection voltages. The varying kinetic energies of ions are converted into internal energy, which causes the unfolding, upon several thousand collisions with the background gas molecules (81–83) prior to IM-MS analysis. The unfolding of protein typically results in a larger conformation *i.e.* larger Ω; however, CIU results in further compaction in some cases (34, 79).

The extensive CIU energy eventually leads to collision-induced dissociation (CID) of protein complexes. Previous studies show that CID of protein ions ejects one of the subunits with a disproportionally large amount of charge concomitant with extensive unfolding of the ejected subunit via Coulombic repulsion (82, 84–86). This phenomenon is referred to as asymmetrical charge partitioning and is observed with other slow heating activation of gas phase protein ions (87). Recent computational approaches (88, 89) incorporate mobile charges via mobile protons within coarse-grain models and support asymmetric charge partitioning as the primary mechanism of CID.

1.5.2 CIU Analysis of Proteins

CIU analysis has been used to classify or characterize protein ions by subclass (90), isoform (91), ligand binding (92), the number of domains (90), and other structural characteristics such as the presence of internal cavities (78). In addition, CIU is sensitive to

structural characteristics that may be highly localized and may be above the resolution of the current native IM-MS analysis (93, 94). For example, conformational states of Abelson protein tyrosine kinase (Abl) is predicted to display less than 1% difference in terms of native Ω (95). However, the isoforms of Abl are differentiated using CIU analysis (94).

Interactions between proteins and buffer ions in the gas phase has been investigated using CIU analysis (86, 96, 97). The binding of nonvolatile buffer ions to proteins in the gas phase increases the CIU stability (86, 96, 97). The extent of increase in the CIU/CID stability differs by the identity of the buffer ions including whether the ions are cations or anions. The binding of cations generally appears to induce greater stability against CID compared to the equivalent amount of anion binding (86, 97). Conversely, the binding of anions more effectively stabilizes protein ions against CIU compared to the equivalent amount of cations (86, 97). The binding of cations stabilizes protein ions by limiting the charge mobility (86). For example, cations can tether multiple groups in proteins via multidentate interactions, or they can replace mobile protons with less mobile cations. The binding of anions increases the stability of protein via dissociative cooling *i.e.* dissociation of the protein-anion complex as neutral molecules to stabilize the complex (97).

1.5.3 Analysis of CIU Data

CIU analysis holds promise for inclusion in high throughput applications including drug binding screening (94, 98, 99) and sequence variant analyses (91, 100). Several efforts have been reported to quantitatively analyze and visualize CIU data in automated fashions (101, 102). For many automated or semi-automated analyses, CIU data is compiled in a matrix format that consists of several mobility results varied by the activation energy (101, 102). One of the most common ways to report CIU results is in the form of a heat map with additional features

including normalization, interpolation, and smoothing (102). Quantitative classifications of analytes based on CIU results have been implemented using various machine learning algorithms and statistical models (102). Quantitative comparisons between CIU results have been reported in terms of root-mean-square-deviation (RMSD) (102) or an in-house developed score, notably, the similarity score (93).

1.6 Analysis of Native-like Antibody Biotherapeutics

Biotherapeutics are drug therapy products produced from a biological source *e.g.*, living cells. Monoclonal antibodies (mAbs) are one of the fastest growing drug classes that are currently in development or are recently approved (103–105). The need for analytical techniques to characterize and standardize mAbs for quality control is rapidly growing. The challenges of developing analytical techniques for mAbs are their relatively large size (~ 150 kDa), heterogeneity, and dynamic nature. To the best of my knowledge, there are only a few structures of full-length mAbs determined from x-ray crystallography (106–108). Traditionally, MS or tandem MS (MS/MS) in combination with liquid chromatography (LC) is used to analyze mAb biotherapeutics. For example, this LC-MS/MS approach is commonly applied to obtain the sequence of a mAb (109). Additionally, LC-MS is used to quantify mAbs in terms of the ratio of the intact light and heavy chain (109) and drug-to-antibody conjugates (110).

Native MS provides insights into the apparent mass (111), mass heterogeneity (111), glycan analysis (111), stability (112) and antibody:antigen stoichiometry (113) of the intact mAb. The accurate mass information may be enhanced with high mass resolution mass analyzers such as the ion trap mass analyzer (114). The IM analysis of native-like mAbs is sensitive to the conformational heterogeneity induced by varying types of disulfide connectivity (115). The Ω of mAbs depends on the z (21, 116) in contrast to other proteins that do not contain the flexible

hinge region (30, 34). The absolute Ω of native-like mAb cations is lower than the Ω determined from x-ray crystallography (21). A molecular dynamics (MD) study supported that the compaction is attributed to the presence of flexible hinge region of mAbs (116).

CIU analysis of mAbs is sensitive to the number and connectivity of disulfide bonds (90), mutation (100), and glycosylation or deglycosylation (90) of mAbs. Recently, CIU was used to compare Inflectra/Remsima (Celltrion), the biosimilar approved by the Food and Drug Administration based off the original product Remicade (infliximab, Janssen) (117). The difference between the CIU results was similar to "levels reported for replicates of the mAb (90)." Additionally, the CIU results comparing the different lots of Remsima exhibited noticeable differences in the low energy range attributed to possible variance by glycoforms.

1.7 Polarity of "Native-like" Protein Ions

Ions formed from ESI are generated from electrolytic reactions (118). The electrolytic reactions depend on polarity; positive ion mode induces oxidation while negative ion mode induces reduction, generating or eliminating H^+ or OH^- or other acidic or basic species. As a result, positive and negative ion mode induce acidic and basic solution respectively (118), resulting in a different pH compared to the initial pH. The extent of the effects of electrolytic reaction varies by several MS parameters including solution flow rate, ES current, metal components of the capillary (*e.g.*, Pt capillary), metal contact to the solution (*e.g.*, Pt wire), and the initial solution conditions including solvents, pH, and buffering capacity (118).

In native MS, positively charged protein ions formed from ESI contain excess protons, $[M+nH]^{n+}$, while the anions are proton deficient $[M-nH]^{n-}$. Typically, native anions display larger extents of nonspecifically binding adducts indicated by broader peaks (30). The average charge state of anions is lower than the cations (30). This has been attributed to the lower

emission energy of anions by the charge residue-field emission model (13). The Ω of most native-like proteins is independent of *z* and polarity despite differences in the number of protons (30, 93). This indicates that the structural differences between the anions and cations are highly localized and may be above the resolution of the current IM-MS analysis.

Though most MS or native MS analyses of proteins are performed in positive ion mode, some studies suggest that anions of native-like proteins may be beneficial. For example, native MS analysis of a tetrameric membrane protein, AqpZ, displays that the anions better preserved the quaternary structure and that peak resolution is enhanced compared to the cations (119). Additionally, the lower average charge state distributions of anions increase the spectral resolution by increasing the *m*/*z* spacing of ions of similar mass. This may be useful to analyze species that appear at similar *m*/*z* [113] *i.e.* proteins of varying oligomeric states or binding of small-molecules [114].

1.8 Outline of the Present Study

The present thesis primarily discusses native MS and IM-MS analysis of protein ions.

Chapter 2 investigates the stoichiometry of Fe:S in the endogenous Fe-S cluster that binds to the complex of the F-box and leucine-rich protein 5 (Fbox) and Skp1 (Fbox-Skp1) using native MS. The native MS of Fbox-Skp1 exhibited broad peaks indicating that both the current TOF mass resolution and nonspecifically binding adducts interfere with the signal. Instrumental and thermal activation in solution prior to nESI are applied to unambiguously understand the Fe-S cluster binding. The thermal activation in solution prior to nESI combined with the instrumental activation is a facile way to sufficiently release nonspecifically boundadducts. The MS analysis with the thermal and instrumental activation demonstrates that Fbox-Skp1 binds primarily to [2Fe-2S].

Chapter 3 discusses the effects of polarity on native MS, native IM-MS, and CIU of the avidin tetramer. First, the effects of polarity on the apparent mass, apparent peak width, and the charge state distributions are compared using native MS. The native-like anions exhibit lower average charge state distributions and a greater extent of nonspecifically bound adducts, though the apparent mass information is consistent with the cations. In addition, the IM-MS analysis demonstrates that the apparent Ω of native-like avidin ions are independent of *z* and polarity. CIU analysis exhibits differences based on the native *z* and solely polarity. A similarity score system is developed to quantitatively compare the CIU results as a function of laboratory frame energy. The similarity score analysis comparing 14+ and 14– avidin indicates that the cations and anions exhibit the largest difference in their Ω distributions near 800 eV. Lastly, the CID efficiency of avidin tetramer ions appears to be slightly greater for the cations than the anions.

Chapter 4 discusses native MS, native IM-MS, and CIU analysis of antibodies (Abs) using two Abs, ^{S}IgG2 and ^{A}IgG2. ^{S}IgG2 and ^{A}IgG2 are the same subclass of IgG purified from human myeloma plasma with the same type of light chain (κ) produced and manufactured from different vendors (Millipore Sigma-Aldrich and Athens Research and Technology respectively). ^{S}IgG2 and ^{A}IgG2 are used as model systems to evaluate native MS, native IM-MS, and CIU techniques for differentiating similar proteins such as monoclonal antibodies (mAbs) and/or biosimilar mAbs. Native MS analysis of the intact antibodies provides insights into the apparent mass and relative mass heterogeneity. In addition, the MS analysis is used to investigate the glycosylation of the intact antibodies. The deglycosylated MS of ^{S}IgG2 and ^{A}IgG2 was deconvoluted by using cation-to-anion proton-transfer reactions (CAPTR) (120). This study is useful to understand the extent of glycosylation and the heterogeneity of the overall mass attributed to glycosylation. The effects of *z* and polarity on structures of Abs are explored using

IM-MS analysis. The results show that the Ω of the native-like Abs is sensitive to *z* and polarity. Furthermore, the extent of the dependence of apparent Ω on *z* and polarity varies by the type of Abs. The CIU of ^{S}IgG2 and ^{A}IgG2 are quantitatively compared using the similarity score (first reported in Chapter 3). The similarity score analysis shows that the comparison between antibody ions is sensitive to energy, polarity, and *z*.

Chapter 5 investigates CIU analysis of protein-ligand complex of interest in the presence of nonspecifically binding adducts. The precursor peak for CIU analysis is selected based on the *m*/*z* of the protein-ligand complex of interest. The precursor selection includes both the protein-ligand of interest and proteins bound by nonspecifically binding adducts despite extensive buffer exchange. The presence of nonspecifically bound adducts increases the CIU stability (96) and may interfere with the effects of the ligand binding of interest; therefore, an energy threshold is determined using $S_{relative}$. This approach may be used more generally for the quality control of CIU analysis.

1.9 References

1. Michael. Karas, Franz. Hillenkamp, Laser desorption ionization of proteins with molecular masses exceeding 10,000 daltons. *Anal. Chem.* **60**, 2299–2301 (1988).
2. J. B. Fenn, M. Mann, C. K. Meng, S. F. Wong, C. M. Whitehouse, Electrospray ionization for mass spectrometry of large biomolecules. *Science* **246**, 64–71 (1989).
3. C. K. Meng, M. Mann, J. B. Fenn, Of protons or proteins. *Z. Für Phys. At. Mol. Clust.* **10**, 361–368 (1988).
4. M. Karas, R. Krüger, Ion Formation in MALDI: The Cluster Ionization Mechanism. *Chem. Rev.* **103**, 427–440 (2003).
5. G. I. Taylor, Disintegration of water drops in an electric field. *Proc. R. Soc. Lond. Ser. Math. Phys. Sci.* **280**, 383–397 (1964).
6. J. Fernandez De La Mora, J. Navascues, F. Fernandez, J. Rosell-Llompart, Generation of submicron monodisperse aerosols in electrosprays. *J. Aerosol Sci.* **21**, S673–S676 (1990).
7. P. Kebarle, U. H. Verkerk, Electrospray: from ions in solution to ions in the gas phase, what we know now. *Mass Spectrom. Rev.* **28**, 898–917 (2009).
8. J. V. Iribarne, B. A. Thomson, On the evaporation of small ions from charged droplets. *J. Chem. Phys.* **64**, 2287–2294 (1976).

9. L. Konermann, E. Ahadi, A. D. Rodriguez, S. Vahidi, Unraveling the Mechanism of Electrospray Ionization. *Anal. Chem.* **85**, 2–9 (2013).
10. J. Fernandez de la Mora, Electrospray ionization of large multiply charged species proceeds via Dole's charged residue mechanism. *Anal. Chim. Acta* **406**, 93–104 (2000).
11. C. J. Hogan, J. A. Carroll, H. W. Rohrs, P. Biswas, M. L. Gross, A Combined Charged Residue-Field Emission Model of Macromolecular Electrospray Ionization. *Anal. Chem.* **81**, 369–377 (2009).
12. C. J. Hogan, J. A. Carroll, H. W. Rohrs, P. Biswas, M. L. Gross, Charge Carrier Field Emission Determines the Number of Charges on Native State Proteins in Electrospray Ionization. *J. Am. Chem. Soc.* **130**, 6926–6927 (2008).
13. C. J. Hogan, J. A. Carroll, H. W. Rohrs, P. Biswas, M. L. Gross, Combined Charged Residue-Field Emission Model of Macromolecular Electrospray Ionization. *Anal. Chem.* **81**, 369–377 (2009).
14. D. Cubrilovic, *et al.*, Determination of Protein–Ligand Binding Constants of a Cooperatively Regulated Tetrameric Enzyme Using Electrospray Mass Spectrometry. *ACS Chem. Biol.* **9**, 218–226 (2014).
15. A. El-Hawiet, *et al.*, Quantifying Ligand Binding to Large Protein Complexes Using Electrospray Ionization Mass Spectrometry. *Anal. Chem.* **84**, 3867–3870 (2012).
16. M. Zhou, *et al.*, Mass spectrometry of intact V-type ATPases reveals bound lipids and the effects of nucleotide binding. *Science* **334**, 380–385 (2011).
17. A. A. Rostom, *et al.*, Detection and selective dissociation of intact ribosomes in a mass spectrometer. *Proc. Natl. Acad. Sci.* **97**, 5185–5190 (2000).
18. D. R. Benjamin, C. V. Robinson, J. P. Hendrick, F. U. Hartl, C. M. Dobson, Mass spectrometry of ribosomes and ribosomal subunits. *Proc. Natl. Acad. Sci.* **95**, 7391–7395 (1998).
19. W. J. van Berkel, R. H. van den Heuvel, C. Versluis, A. J. Heck, Detection of intact megaDalton protein assemblies of vanillyl-alcohol oxidase by mass spectrometry. *Protein Sci. Publ. Protein Soc.* **9**, 435–439 (2000).
20. C. Uetrecht, I. M. Barbu, G. K. Shoemaker, E. van Duijn, A. J. R. Heck, Interrogating viral capsid assembly with ion mobility–mass spectrometry. *Nat. Chem.* **3**, 126–132 (2011).
21. I. D. G. Campuzano, C. Larriba, D. Bagal, P. D. Schnier, "Ion Mobility and Mass Spectrometry Measurements of the Humanized IgGk NIST Monoclonal Antibody" in *State-of-the-Art and Emerging Technologies for Therapeutic Monoclonal Antibody Characterization Volume 3. Defining the Next Generation of Analytical and Biophysical Techniques*, ACS Symposium Series., (American Chemical Society, 2015), pp. 75–112.
22. J. A. Aquilina, J. L. P. Benesch, O. A. Bateman, C. Slingsby, C. V. Robinson, Polydispersity of a mammalian chaperone: Mass spectrometry reveals the population of oligomers in αB-crystallin. *Proc. Natl. Acad. Sci.* **100**, 10611–10616 (2003).
23. V. Franc, J. Zhu, A. J. R. Heck, Comprehensive Proteoform Characterization of Plasma Complement Component C8αβγ by Hybrid Mass Spectrometry Approaches. *J. Am. Soc. Mass Spectrom.* **29**, 1099–1110 (2018).
24. U. A. Mirza, S. L. Cohen, B. T. Chait, Heat-induced conformational changes in proteins studied by electrospray ionization mass spectrometry. *Anal. Chem.* **65**, 1–6 (1993).
25. L. Konermann, D. J. Douglas, Unfolding of proteins monitored by electrospray ionization mass spectrometry: a comparison of positive and negative ion modes. *J. Am. Soc. Mass Spectrom.* **9**, 1248–1254 (1998).

26. L. Konermann, F. I. Rosell, A. G. Mauk, D. J. Douglas, Acid-Induced Denaturation of Myoglobin Studied by Time-Resolved Electrospray Ionization Mass Spectrometry. *Biochemistry* **36**, 6448–6454 (1997).
27. C. C. Going, E. R. Williams, Supercharging with m-Nitrobenzyl Alcohol and Propylene Carbonate: Forming Highly Charged Ions with Extended, Near-Linear Conformations. *Anal. Chem.* **87**, 3973–3980 (2015).
28. J. O. Kafader, *et al.*, Native vs Denatured: An in Depth Investigation of Charge State and Isotope Distributions. *J. Am. Soc. Mass Spectrom.* **31**, 574–581 (2020).
29. J. A. Loo, C. G. Edmonds, H. R. Udseth, R. D. Smith, Effect of reducing disulfide-containing proteins on electrospray ionization mass spectra. *Anal. Chem.* **62**, 693–698 (1990).
30. S. J. Allen, A. M. Schwartz, M. F. Bush, Effects of Polarity on the Structures and Charge States of Native-Like Proteins and Protein Complexes in the Gas Phase. *Anal. Chem.* **85**, 12055–12061 (2013).
31. H. J. Yoo, N. Wang, S. Zhuang, H. Song, K. Håkansson, Negative-Ion Electron Capture Dissociation: Radical-Driven Fragmentation of Charge-Increased Gaseous Peptide Anions. *J. Am. Chem. Soc.* **133**, 16790–16793 (2011).
32. M. W. Forbes, *et al.*, Infrared Spectroscopy of Arginine Cation Complexes: Direct Observation of Gas-Phase Zwitterions. *J. Phys. Chem. A* **111**, 11759–11770 (2007).
33. L. Konermann, Molecular Dynamics Simulations on Gas-Phase Proteins with Mobile Protons: Inclusion of All-Atom Charge Solvation. *J. Phys. Chem. B* **121**, 8102–8112 (2017).
34. Z. Hall, A. Politis, M. F. Bush, L. J. Smith, C. V. Robinson, Charge-state dependent compaction and dissociation of protein complexes: insights from ion mobility and molecular dynamics. *J. Am. Chem. Soc.* **134**, 3429–3438 (2012).
35. M. Majewski, S. Ruiz-Carmona, X. Barril, An investigation of structural stability in protein-ligand complexes reveals the balance between order and disorder. *Commun. Chem.* **2**, 1–8 (2019).
36. D. L. Mobley, K. A. Dill, Binding of Small-Molecule Ligands to Proteins: "What You See" Is Not Always "What You Get." *Struct. Lond. Engl. 1993* **17**, 489–498 (2009).
37. P. Wu, Inhibition of RNA-binding proteins with small molecules. *Nat. Rev. Chem.*, 1–18 (2020).
38. A. P. Davenport, C. C. G. Scully, C. de Graaf, A. J. H. Brown, J. J. Maguire, Advances in therapeutic peptides targeting G protein-coupled receptors. *Nat. Rev. Drug Discov.* **19**, 389–413 (2020).
39. J. Marcoux, *et al.*, Mass spectrometry reveals synergistic effects of nucleotides, lipids, and drugs binding to a multidrug resistance efflux pump. *Proc. Natl. Acad. Sci. U. S. A.* **110**, 9704–9709 (2013).
40. G. D. Tocchini-Valentini, *et al.*, Structural and Functional Insights into the Ligand-binding Domain of a Nonduplicated Retinoid X Nuclear Receptor from the Invertebrate Chordate Amphioxus. *J. Biol. Chem.* **284**, 1938–1948 (2009).
41. H.-Y. Yen, *et al.*, Ligand binding to a G protein–coupled receptor captured in a mass spectrometer. *Sci. Adv.* **3**, e1701016 (2017).
42. A. F. M. Gavriilidou, F. P. Holding, J. E. Coyle, R. Zenobi, Application of Native ESI-MS to Characterize Interactions between Compounds Derived from Fragment-Based Discovery Campaigns and Two Pharmaceutically Relevant Proteins. *SLAS Discov. Adv. Sci. Drug Discov.* **23**, 951–959 (2018).

43. L. Deng, N. Sun, E. N. Kitova, J. S. Klassen, Direct Quantification of Protein−Metal Ion Affinities by Electrospray Ionization Mass Spectrometry. *Anal. Chem.* **82**, 2170–2174 (2010).
44. L. F. Garcia-Alles, *et al.*, Endogenous phosphatidylcholine and a long spacer ligand stabilize the lipid-binding groove of CD1b. *EMBO J.* **25**, 3684–3692 (2006).
45. Peifeng. Hu, Q.-Zhuang. Ye, J. A. Loo, Calcium Stoichiometry Determination for Calcium Binding Proteins by Electrospray Ionization Mass Spectrometry. *Anal. Chem.* **66**, 4190–4194 (1994).
46. D. Fabris, C. Fenselau, Characterization of Allosteric Insulin Hexamers by Electrospray Ionization Mass Spectrometry. *Anal. Chem.* **71**, 384–387 (1999).
47. K. A. Johnson, I. J. Amster, First observation by mass spectrometry of a 3+ oxidation state for a [4Fe-4S] metalloprotein: an ESI-FTICR mass spectrometry study of the high potential iron-sulfur protein from Chromatium vinosum. *J. Am. Soc. Mass Spectrom.* **12**, 819–825 (2001).
48. K. L. Davidson, D. R. Oberreit, C. J. Hogan, M. F. Bush, Nonspecific aggregation in native electrokinetic nanoelectrospray ionization. *Int. J. Mass Spectrom.* **420**, 35–42 (2017).
49. J. Hu, *et al.*, Effect of Nanoemitters on Suppressing the Formation of Metal Adduct Ions in Electrospray Ionization Mass Spectrometry. *Anal. Chem.* **89**, 1838–1845 (2017).
50. M. Landreh, *et al.*, Controlling release, unfolding and dissociation of membrane protein complexes in the gas phase through collisional cooling†. *Chem. Commun. Camb. Engl.* **51**, 15582–15584 (2015).
51. J. Sun, E. N. Kitova, W. Wang, J. S. Klassen, Method for Distinguishing Specific from Nonspecific Protein−Ligand Complexes in Nanoelectrospray Ionization Mass Spectrometry. *Anal. Chem.* **78**, 3010–3018 (2006).
52. T. Wyttenbach, C. Bleiholder, M. T. Bowers, Factors Contributing to the Collision Cross Section of Polyatomic Ions in the Kilodalton to Gigadalton Range: Application to Ion Mobility Measurements. *Anal. Chem.* **85**, 2191–2199 (2013).
53. R. Cumeras, E. Figueras, C. E. Davis, J. I. Baumbach, I. Gràcia, Review on Ion Mobility Spectrometry. Part 1: Current Instrumentation. *The Analyst* **140**, 1376–1390 (2015).
54. E. A. Mason, E. W. McDaniel, *Transport Properties of Ions in Gases* (Wiley, 1988).
55. V. Gabelica, *et al.*, Recommendations for reporting ion mobility Mass Spectrometry measurements. *Mass Spectrom. Rev.* **38**, 291–320 (2019).
56. Y. Liu, D. E. Clemmer, Characterizing Oligosaccharides Using Injected-Ion Mobility/Mass Spectrometry. *Anal. Chem.* **69**, 2504–2509 (1997).
57. B. H. Clowers, P. Dwivedi, W. E. Steiner, H. H. Hill, B. Bendiak, Separation of Sodiated Isobaric Disaccharides and Trisaccharides Using Electrospray Ionization-Atmospheric Pressure Ion Mobility-Time of Flight Mass Spectrometry. *J. Am. Soc. Mass Spectrom.* **16**, 660–669 (2005).
58. C. Uetrecht, R. J. Rose, E. van Duijn, K. Lorenzen, A. J. R. Heck, Ion mobility mass spectrometry of proteins and proteinassemblies. *Chem. Soc. Rev.* **39**, 1633–1655 (2010).
59. A. B. Kanu, P. Dwivedi, M. Tam, L. Matz, H. H. Hill, Ion mobility–mass spectrometry. *J. Mass Spectrom.* **43**, 1–22 (2008).
60. E. W. McDaniel, D. W. Martin, W. S. Barnes, Drift Tube-Mass Spectrometer for Studies of Low-Energy Ion-Molecule Reactions. *Rev. Sci. Instrum.* **33**, 2–7 (1962).
61. W. S. Barnes, D. W. Martin, E. W. McDaniel, Mass Spectrographic Identification of the Ion Observed in Hydrogen Mobility Experiments. *Phys. Rev. Lett.* **6**, 110–111 (1961).
62. G. M. Thomson, *et al.*, Mobility, diffusion, and clustering of K+ ions in gases. *J. Chem. Phys.* **58**, 2402–2411 (1973).

63. L. G. McKnight, K. B. McAfee, D. P. Sipler, Low-Field Drift Velocities and Reactions of Nitrogen Ions in Nitrogen. *Phys. Rev.* **164**, 62–70 (1967).
64. K. B. McAfee, D. Sipler, D. Edelson, Mobilities and Reactions of Ions in Argon. *Phys. Rev.* **160**, 130–135 (1967).
65. C. S. Hoaglund-Hyzer, D. E. Clemmer, Ion Trap/Ion Mobility/Quadrupole/Time-of-Flight Mass Spectrometry for Peptide Mixture Analysis. *Anal. Chem.* **73**, 177–184 (2001).
66. X. Tang, J. E. Bruce, H. H. Hill, Design and performance of an atmospheric pressure ion mobility Fourier transform ion cyclotron resonance mass spectrometer. *Rapid Commun. Mass Spectrom.* **21**, 1115–1122 (2007).
67. P. R. Kemper, M. T. Bowers, A hybrid double-focusing mass spectrometer—High-pressure drift reaction cell to study thermal energy reactions of mass-selected ions. *J. Am. Soc. Mass Spectrom.* **1**, 197–207 (1990).
68. Ph. Dugourd, R. R. Hudgins, D. E. Clemmer, M. F. Jarrold, High-resolution ion mobility measurements. *Rev. Sci. Instrum.* **68**, 1122–1129 (1997).
69. M. Guilhaus, D. Selby, V. Mlynski, Orthogonal acceleration time-of-flight mass spectrometry. *Mass Spectrom. Rev.* **19**, 65–107 (2000).
70. S. D. Pringle, *et al.*, An investigation of the mobility separation of some peptide and protein ions using a new hybrid quadrupole/travelling wave IMS/oa-ToF instrument. *Int. J. Mass Spectrom.* **261**, 1–12 (2007).
71. K. Giles, *et al.*, Applications of a travelling wave-based radio-frequency-only stacked ring ion guide. *Rapid Commun. Mass Spectrom.* **18**, 2401–2414 (2004).
72. K. Giles, J. P. Williams, I. Campuzano, Enhancements in travelling wave ion mobility resolution. *Rapid Commun. Mass Spectrom. RCM* **25**, 1559–1566 (2011).
73. Y. Zhong, S.-J. Hyung, B. T. Ruotolo, Characterizing the resolution and accuracy of a second-generation traveling-wave ion mobility separator for biomolecular ions. *Analyst* **136**, 3534–3541 (2011).
74. M. F. Bush, *et al.*, Collision cross sections of proteins and their complexes: a calibration framework and database for gas-phase structural biology. *Anal. Chem.* **82**, 9557–9565 (2010).
75. S. J. Allen, M. F. Bush, Radio-Frequency (rf) Confinement in Ion Mobility Spectrometry: Apparent Mobilities and Effective Temperatures. *J. Am. Soc. Mass Spectrom.* **27**, 2054–2063 (2016).
76. S. J. Allen, K. Giles, T. Gilbert, M. F. Bush, Ion mobility mass spectrometry of peptide, protein, and protein complex ions using a radio-frequency confining drift cell. *Analyst* **141**, 884–891 (2016).
77. B. T. Ruotolo, J. L. P. Benesch, A. M. Sandercock, S.-J. Hyung, C. V. Robinson, Ion mobility–mass spectrometry analysis of large protein complexes. *Nat. Protoc.* **3**, 1139–1152 (2008).
78. B. T. Ruotolo, *et al.*, Evidence for Macromolecular Protein Rings in the Absence of Bulk Water. *Science* **310**, 1658–1661 (2005).
79. N. A. Pierson, D. E. Clemmer, An IMS-IMS threshold method for semi-quantitative determination of activation barriers: Interconversion of proline cis↔trans forms in triply protonated bradykinin. *Int. J. Mass Spectrom.* **377**, 646–654 (2015).
80. K. B. Shelimov, M. F. Jarrold, Conformations, Unfolding, and Refolding of Apomyoglobin in Vacuum: An Activation Barrier for Gas-Phase Protein Folding. *J. Am. Chem. Soc.* **119**, 2987–2994 (1997).

81. P. M. Mayer, C. Poon, The mechanisms of collisional activation of ions in mass spectrometry. *Mass Spectrom. Rev.* **28**, 608–639 (2009).
82. J. L. P. Benesch, B. T. Ruotolo, D. A. Simmons, C. V. Robinson, Protein Complexes in the Gas Phase: Technology for Structural Genomics and Proteomics. *Chem. Rev.* **107**, 3544–3567 (2007).
83. S. A. McLuckey, D. E. Goeringer, SPECIAL FEATURE: TUTORIAL Slow Heating Methods in Tandem Mass Spectrometry. *J. Mass Spectrom.* **32**, 461–474 (1997).
84. K. J. Light-Wahl, B. L. Schwartz, R. D. Smith, Observation of the Noncovalent Quaternary Associations of Proteins by Electrospray Ionization Mass Spectrometry. *J. Am. Chem. Soc.* **116**, 5271–5278 (1994).
85. J. C. Jurchen, E. R. Williams, Origin of Asymmetric Charge Partitioning in the Dissociation of Gas-Phase Protein Homodimers. *J. Am. Chem. Soc.* **125**, 2817–2826 (2003).
86. L. Han, S.-J. Hyung, B. T. Ruotolo, Bound Cations Significantly Stabilize the Structure of Multiprotein Complexes in the Gas Phase. *Angew. Chem. Int. Ed.* **51**, 5692–5695 (2012).
87. N. Felitsyn, E. N. Kitova, J. S. Klassen, Thermal Decomposition of a Gaseous Multiprotein Complex Studied by Blackbody Infrared Radiative Dissociation. Investigating the Origin of the Asymmetric Dissociation Behavior. *Anal. Chem.* **73**, 4647–4661 (2001).
88. V. Popa, D. A. Trecroce, R. G. McAllister, L. Konermann, Collision-Induced Dissociation of Electrosprayed Protein Complexes: An All-Atom Molecular Dynamics Model with Mobile Protons. *J. Phys. Chem. B* **120**, 5114–5124 (2016).
89. S. K. Fegan, M. Thachuk, A Charge Moving Algorithm for Molecular Dynamics Simulations of Gas-Phase Proteins. *J. Chem. Theory Comput.* **9**, 2531–2539 (2013).
90. Y. Tian, L. Han, A. C. Buckner, B. T. Ruotolo, Collision Induced Unfolding of Intact Antibodies: Rapid Characterization of Disulfide Bonding Patterns, Glycosylation, and Structures. *Anal. Chem.* **87**, 11509–11515 (2015).
91. J. D. Eschweiler, R. M. Martini, B. T. Ruotolo, Chemical Probes and Engineered Constructs Reveal a Detailed Unfolding Mechanism for a Solvent-Free Multidomain Protein. *J. Am. Chem. Soc.* **139**, 534–540 (2017).
92. J. T. S. Hopper, N. J. Oldham, Collision Induced Unfolding of Protein Ions in the Gas Phase Studied by Ion Mobility-Mass Spectrometry: The Effect of Ligand Binding on Conformational Stability. *J. Am. Soc. Mass Spectrom.* **20**, 1851–1858 (2009).
93. S. Hong, M. F. Bush, Collision-Induced Unfolding Is Sensitive to the Polarity of Proteins and Protein Complexes. *J. Am. Soc. Mass Spectrom.* **30**, 2430–2437 (2019).
94. J. N. Rabuck, *et al.*, Activation State-Selective Kinase Inhibitor Assay Based on Ion Mobility-Mass Spectrometry. *Anal. Chem.* **85**, 6995–7002 (2013).
95. M. F. Mesleh, J. M. Hunter, A. A. Shvartsburg, G. C. Schatz, M. F. Jarrold, Structural Information from Ion Mobility Measurements: Effects of the Long-Range Potential. *J. Phys. Chem.* **100**, 16082–16086 (1996).
96. J. Freeke, M. F. Bush, C. V. Robinson, B. T. Ruotolo, Gas-phase protein assemblies: Unfolding landscapes and preserving native-like structures using noncovalent adducts. *Chem. Phys. Lett.* **524**, 1–9 (2012).
97. L. Han, S.-J. Hyung, J. J. S. Mayers, B. T. Ruotolo, Bound anions differentially stabilize multiprotein complexes in the absence of bulk solvent. *J. Am. Chem. Soc.* **133**, 11358–11367 (2011).

98. S. Mehmood, *et al.*, Mass spectrometry captures off-target drug binding and provides mechanistic insights into the human metalloprotease ZMPSTE24. *Nat. Chem.* **8**, 1152–1158 (2016).
99. D. P. Byrne, *et al.*, cAMP-dependent protein kinase (PKA) complexes probed by complementary differential scanning fluorimetry and ion mobility–mass spectrometry. *Biochem. J.* **473**, 3159–3175 (2016).
100. O. Hernandez-Alba, E. Wagner-Rousset, A. Beck, S. Cianférani, Native Mass Spectrometry, Ion Mobility, and Collision-Induced Unfolding for Conformational Characterization of IgG4 Monoclonal Antibodies. *Anal. Chem.* (2018) https:/doi.org/10.1021/acs.analchem.8b00912 (July 2, 2020).
101. T. M. Allison, *et al.*, Quantifying the stabilizing effects of protein–ligand interactions in the gas phase. *Nat. Commun.* **6**, 8551 (2015).
102. D. A. Polasky, S. M. Dixit, S. M. Fantin, B. T. Ruotolo, CIUSuite 2: Next-Generation Software for the Analysis of Gas-Phase Protein Unfolding Data. *Anal. Chem.* **91**, 3147–3155 (2019).
103. J. M. Reichert, C. J. Rosensweig, L. B. Faden, M. C. Dewitz, Monoclonal antibody successes in the clinic. *Nat. Biotechnol.* **23**, 1073–1078 (2005).
104. J. M. Reichert, Antibodies to watch in 2010. *mAbs* **2**, 84–100 (2010).
105. J. M. Reichert, Monoclonal antibodies as innovative therapeutics. *Curr. Pharm. Biotechnol.* (2008) https:/doi.org/10.2174/138920108786786358.
106. L. J. Harris, E. Skaletsky, A. McPherson, Crystallographic structure of an intact IgG1 monoclonal antibody. *J. Mol. Biol.* **275**, 861–872 (1998).
107. E. O. Saphire, *et al.*, Crystal Structure of a Neutralizing Human IgG Against HIV-1: A Template for Vaccine Design. *Science* **293**, 1155–1159 (2001).
108. L. J. Harris, S. B. Larson, K. W. Hasel, A. McPherson, Refined structure of an intact IgG2a monoclonal antibody. *Biochemistry* **36**, 1581–1597 (1997).
109. P. M. Ladwig, D. R. Barnidge, M. A. V. Willrich, Mass Spectrometry Approaches for Identification and Quantitation of Therapeutic Monoclonal Antibodies in the Clinical Laboratory. *Clin. Vaccine Immunol. CVI* **24** (2017).
110. X. Zhu, S. Huo, C. Xue, B. An, J. Qu, Current LC-MS-based strategies for characterization and quantification of antibody-drug conjugates. *J. Pharm. Anal.* **10**, 209–220 (2020).
111. S. Rosati, *et al.*, Exploring an Orbitrap Analyzer for the Characterization of Intact Antibodies by Native Mass Spectrometry. *Angew. Chem. Int. Ed.* **51**, 12992–12996 (2012).
112. R. J. Rose, *et al.*, Quantitative analysis of the interaction strength and dynamics of human IgG4 half molecules by native mass spectrometry. *Struct. Lond. Engl. 1993* **19**, 1274–1282 (2011).
113. M. A. Tito, *et al.*, Probing Molecular Interactions in Intact Antibody: Antigen Complexes, an Electrospray Time-of-Flight Mass Spectrometry Approach. *Biophys. J.* **81**, 3503–3509 (2001).
114. S. Rosati, Y. Yang, A. Barendregt, A. J. R. Heck, Detailed mass analysis of structural heterogeneity in monoclonal antibodies using native mass spectrometry. *Nat. Protoc.* **9**, 967–976 (2014).
115. D. Bagal, J. F. Valliere-Douglass, A. Balland, P. D. Schnier, Resolving Disulfide Structural Isoforms of IgG2 Monoclonal Antibodies by Ion Mobility Mass Spectrometry. *Anal. Chem.* **82**, 6751–6755 (2010).

116. K. J. Pacholarz, *et al.*, Dynamics of intact immunoglobulin G explored by drift-tube ion-mobility mass spectrometry and molecular modeling. *Angew. Chem. Int. Ed Engl.* **53**, 7765–7769 (2014).
117. K. Pisupati, *et al.*, A Multidimensional Analytical Comparison of Remicade and the Biosimilar Remsima. *Anal. Chem.* **89**, 4838–4846 (2017).
118. G. J. Van Berkel, F. Zhou, J. T. Aronson, Changes in bulk solution pH caused by the inherent controlled-current electrolytic process of an electrospray ion source. *Int. J. Mass Spectrom. Ion Process.* **162**, 55–67 (1997).
119. I. Liko, J. T. S. Hopper, T. M. Allison, J. L. P. Benesch, C. V. Robinson, Negative Ions Enhance Survival of Membrane Protein Complexes. *J. Am. Soc. Mass Spectrom.* **27**, 1099–1104 (2016).
120. K. J. Laszlo, M. F. Bush, Analysis of Native-Like Proteins and Protein Complexes Using Cation to Anion Proton Transfer Reactions (CAPTR). *J. Am. Soc. Mass Spectrom.* **26**, 2152–2161 (2015).

Chapter 2: [2Fe-2S] Cluster Binding to FBXL5

2.1 Abstract

F-box and leucine-rich protein 5 (FBXL5) is the substrate receptor subunit of Skp1-Cul1-Fbox (SCF) E3 ubiquitin ligase complexes. Cellular iron homeostasis is maintained by degradation of iron regulatory protein 2 (IRP2) mediated by FBXL5 (1, 2). Preliminary biochemical and biophysical analysis by Wang et al. (3) suggests that FBXL5 binds to Fe-S clusters of unknown Fe:S stoichiometry. Here, the stoichiometry of Fe:S is investigated using native MS and MS of the intact FBXL5-Skp1 under activating conditions. Native MS of FBXL5-Skp1 was interfered by nonspecifically-binding adducts under low desolvation energy. Instrumental activation in combination with thermal activation in solution prior to the ESI were effective in removing the nonspecifically-binding adducts. The [2Fe-2S] primarily binds to FBXL5-Skp1 under positive and negative ESI polarity indicating that the [2Fe-2S] binding to FBXL5-Skp1 is independent of the redox induced by ESI under conditions used in this study.

2.2 Introduction

Iron-sulfur clusters (Fe-S) are important cofactors for proteins in many cellular processes including photosynthesis (4), nitrogen fixation (5), redox reactions (6) and iron homeostasis (7). The oxidation state of Fe-S clusters (8) depends on the surrounding amino acid (*i.e.* the 3-

dimensional structure of the protein (9)) or the solvent environment (*i.e.* hydration (10)). Biologically relevant Fe-S clusters can exhibit varying Fe:S stoichiometry (11–13). [2Fe-2S] and [4Fe-4S] are the most common types of Fe-S clusters in biological systems (13).

Mass spectrometry (MS) of intact proteins has been used to identify the oxidation state (14) and the stoichiometry (14, 15) of Fe-S clusters. For instance, MS was used to investigate the changes to the stoichiometry of Fe:S in Fe-S clusters that interact with scaffold proteins in a time-dependent manner (15). The oxidation state of Fe-S clusters is determined using a MS-based approach that uses the accurate mass of the apo protein and the difference between the number of excess protons and the charge state of the holoproteins. Therefore, determining the oxidation state of the Fe-S cluster requires a high-resolution mass spectrometer (16–18) that isotopically resolves the mass of the apo and holoprotein with at least 1 Da accuracy. For example, the oxidation state of the [4Fe-4S] cluster that binds to the high-potential iron-sulfur protein from *Chromatium vinosum* was determined to be 3+ using ESI-FT-ICR in positive ion mode (14).

The iron responsive element (IRE) regulates the intracellular iron levels via interactions with iron responsive domain 1 and iron responsive domain 2 (IRP2) (7, 19, 20). F-box and leucine-rich protein 5 (FBXL5) is the substrate receptor subunit of Skp1-Cul1-Fbox (SCF) ubiquitin ligase complexes that aids in the degradation of IRP2 under the iron-enriched environment (1, 2). The biochemical basis for the interactions between FBXL5 and IRP2 has not been fully understood. The UV/vis absorption analysis by Wang et al. (3) confirms the presence of the endogenous Fe-S cluster binding to FBXL5. Initially, the cryo-EM structure by Wang et al. at resolution above 3 Å supports the rhombic shape of the Fe-S cluster binding to FBXL5 which is indicative of [2Fe-2S] stoichiometry (12). The objective of this study is to confirm the binding of

endogenous Fe-S clusters to FBXL5-Skp1 complex and to identify the stoichiometry of Fe:S. In order to identify the Fe-S cluster and improve the spectrum quality, various methods of activation including instrumental (*e.g.*, collisional and sampling cone voltage) and thermal activation are applied. Additionally, the stoichiometry of Fe-S cluster binding is assessed in both polarities that induces reduction and oxidation conditions for negative and positive ion mode respectively.

2.3 Experimental Methods

FBXL5-Skp1 was purified and expressed by Wang et al (3). The FBXL5-Skp1 (3) complex was buffer exchanged into aqueous 200 mM ammonium acetate at pH 7.0 using centrifugal concentrators (10 kDa MWCO, Spin-X UF, Corning, Inc.) and a centrifuge operated at 4 °C. The thermal activation includes heating the protein sample using a heating block at ~52 °C for one minute prior to the nESI. The protein samples were loaded into glass capillaries with inner diameters of 0.78 mm that were pulled to approximately 1 to 3 μm on one end using a micropipette puller (P-97, Sutter Instruments, Novato, CA) for nanoelectrospray ionization. 10 μM of sample was loaded into the glass capillary tip. Electrical contact with the solution was attained by inserting a platinum wire electrode into the wide end of the capillary (21). To minimize impurity carryover between experiments, the electrode was washed with aqueous 25% HCl (v:v) and rinsed with ultrapure (18.2 MΩ) water between samples. Data were acquired using a Waters Synapt G2 HDMS hybrid mass spectrometer (Waters Co., Wilmslow, UK) (22) in which the traveling-wave ion mobility cell was replaced with a radio-frequency (RF) confining drift cell (23) that contained approximately 1.7 Torr He. The following MS parameters were used for native MS in positive ion mode: capillary voltage, less than 1.0 kV; sampling cone, 20 V; extraction cone, 5 V; source temperature, ~ 30 ºC; trap collision energy, 4 V; trap gas flow, 3 – 8

ml/min. MS parameters that deviated from those listed above are noted in the figure captions. The following MS parameters were used for MS in negative ion mode: capillary voltage, less than 1.0 kV; sampling cone, 50 V; extraction cone, 2 V; source temperature, ~ 30 ºC; trap collision energy, 30 V; trap gas flow, 1 mL/min. MS parameters of the instrumental activation of FBXL5-Skp1 are noted in the corresponding figure captions. Mass spectra were analyzed using MassLynx v4.1 (Waters, Co., Milford, MA).

2.3 Results

2.3.1 MS Analysis of the Intact FBXL5-Skp1

Figure 2.1 shows the native MS of FBXL5-Skp1 in positive ion mode. The narrow range of charge states is consistent with general characteristics of native-like proteins. Figure 2.2 shows the enlarged native MS of 13+ FBXL5-Skp1 and displays apparent two peaks. However, the peaks are broad and show poor alignment with the theoretical mass of the apo FBXL5-Skp1. The width is most likely attributed to binding of nonspecific adducts. Alternatively, the possible binding of divalent metal ions (*e.g.*, Fe-S cluster binding) may exacerbate the broadening because the isotopic distributions of divalent metal ions differ from the amino acid.

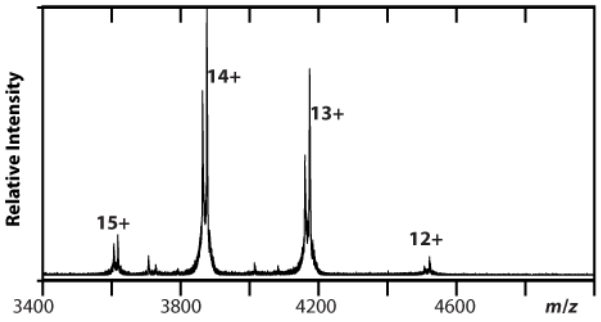

Figure 2.1. The native MS of FBXL5-Skp1in positive ion mode.

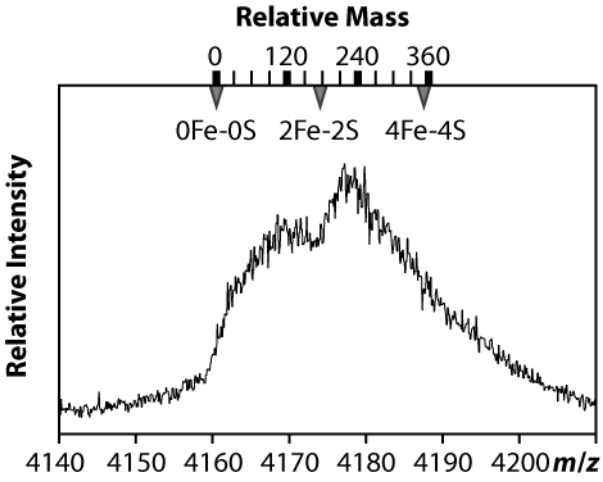

Figure 2.2. The native MS of FBXL5-Skp1in positive ion mode (no activation).

Figure 2.3a exhibits two primary peaks with reduced presence of adducts as a result of instrumental activation achieved by increasing collision and sampling cone voltage. The bimodal peak shape is a consistent feature observed with the native MS (Figure 2.1) indicating that the noncovalent interactions between FBXL5 and Skp1 and primary ligands are preserved. The two peaks (Figure 2.3a) are aligned with the apo and the binding of [2Fe-2S] (Figure 2.3a). The most intense signal corresponds to the binding of [2Fe-2S] suggesting that FBXL5-Skp1 primarily binds to [2Fe-2S] clusters. This conclusion is consistent with the rhombic shape of the bound Fe-S cluster observed by cryo-EM and stoichiometry of Fe:S later determined from electron paramagnetic resonance (3).

Some additional signal other than the apo and [2Fe-2S] bound peaks were present in the mass spectrum. This suggests that FBXL5-Skp1 binds to nonspecifically-binding adducts. In order to further investigate the origin of the minor signal, additional thermal activation is applied. A previous study reported that thermal activation of proteins in solution prior to ESI has been utilized to induce more subtle unfolding as compared to collision-induced activation (24). The extent of unfolding by thermal activation depends on the time scale, temperature range and the precursor ions (24, 25).

Figure 2.3b shows the MS of FBXL5-Skp1 under both thermal activation in solution prior to the ESI and instrumental activation. Figure 2.3b shows that the baseline of the minor signal decreased compared to Figure 2.3a, while FBXL5-Skp1 primarily binds to [2Fe-2S] cluster. This indicates that the thermal activation is useful to release nonspecifically-binding adducts without disrupting specific noncovalent interactions with Fe-S clusters and/or between FBXL5 and Skp1. On the contrary, increasing extent of activation solely by instrumental parameters (*i.e* greater extent of instrumental activation than shown in Figure 2.3a) did not

decrease the presence of adducts but appeared to release S (sulfur) from [2Fe-2S] clusters at significantly higher energy (data not shown). This may indicate that the thermal activation may induce subtle activation that removes adducts but preserves the characteristics of noncovalent interactions observed using native MS (Figure 2.2). Therefore, additional thermal activation may be a facile way to confer a relatively gentler activation to elucidate specific binding interactions in combination with instrumental activation.

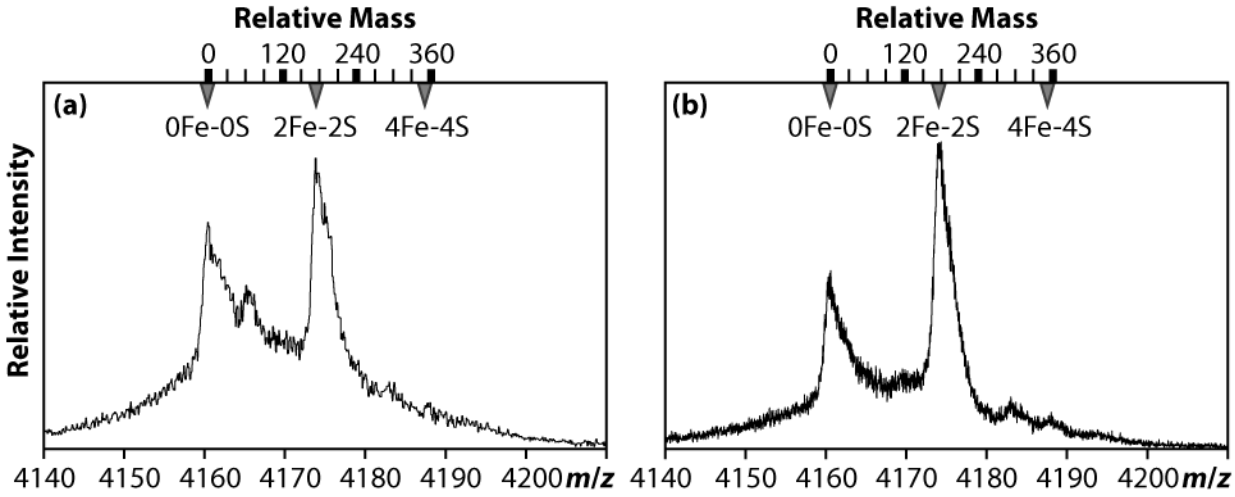

Figure 2.3. Results from native mass spectrometry of the 13+ FBXL5-Skp1 complex. The top axis shows the mass relative to the apo complex. The relative masses expected for the 2Fe-2S and 4Fe-4S containing complexes were calculated assuming Fe^{2+} and S^{2-}. (a) The FBXL5-Skp1 complex was not heated prior to the nESI but subjected to instrumental activation (sampling cone: 70 V and trap CE: 50 V). (b) The FBXL5-Skp1 complex was heated at 52 ºC prior to the nESI in addition to some instrumental activation (sampling cone: 70 V and trap CE: 50 V).

2.3.2 Fe-S Cluster Binding in Redox Conditions Induced by ESI

The redox state of the Fe-S cluster affects the interaction between FBXL5 and IRP2 (3). In addition, a previous study reported that metal binding stoichiometry depends on the polarity for some protein systems (26). In ESI, the positive and negative ion modes induce oxidizing and reducing conditions respectively (27). Figure 2.4 shows the full MS of FBXL5-Skp1 in negative ion mode. Compared to the positive MS (Figure 2.1), the average charge state is lower for anions than cations, which is consistent with native MS of most proteins (28, 29). Figure 2.5a and 2.5b show the enlarged MS of 13+ and 13− FBXL5-Skp1 respectively. The quality of the spectrum of the anions (Figure 2.5b) is poorer than cations because anions contain more adducts than the cations. The greater presence of adducts in anion spectra is commonly observed for other native-like proteins (28). Despite the difference in the quality of the MS, the MS of 13− FBXL5-Skp1 shows the most intense signal corresponding to protein binding to [2Fe-2S] clusters (Figure 2.5b). This suggests that the [2Fe-2S] binding to FBXL5-Skp1 is not affected by the polarity under conditions used in this study.

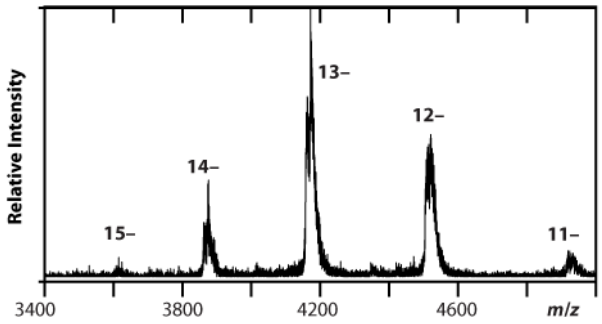

Figure 2.4. The native MS of FBXL5-Skp1 in negative ion mode.

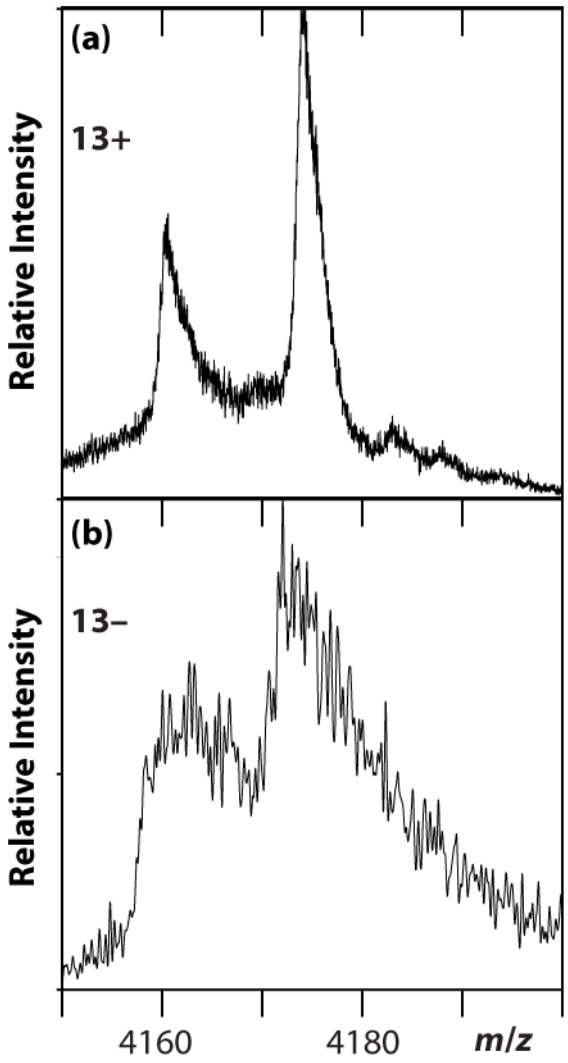

Figure 2.5. The enlarged MS of (a) 13+ and (b) 13− FBXL5-Skp1 in positive and negative ion mode respectively.

2.4 Conclusions

The native MS analysis demonstrates that FBXL5-Skp1 primarily binds to endogenous [2Fe-2S] clusters in positive and negative ion modes. The instrumental activation is useful to remove the nonspecifically-binding adducts and to elucidate the stoichiometry of Fe:S in the Fe-S cluster. The minor presence of nonspecifically-binding adducts can be further removed by additional thermal activation in solution prior to ESI while maintaining the primary noncovalent interactions of FBXL5-Skp1. This indicates that a brief thermal heating in solution prior to ESI may be a facile and robust way to release nonspecifically-binding adducts and to improve the spectrum quality.

2.5 Acknowledgements

This work was supported by funds from the National Science Foundation (CHE-1807382 to M.F.B.). M.F.B. and S.H. acknowledge support from the University of Washington. The authors thank Prof. Ning Zheng and Dr. Hui Wang for providing the FBXL5-Skp1 samples and critical insights.

2.6 References

1. A. A. Salahudeen, *et al.*, An E3 Ligase Possessing an Iron-Responsive Hemerythrin Domain Is a Regulator of Iron Homeostasis. *Science* **326**, 722–726 (2009).
2. A. A. Vashisht, *et al.*, Control of Iron Homeostasis by an Iron-Regulated Ubiquitin Ligase. *Science* **326**, 718–721 (2009).
3. H. Wang, *et al.*, FBXL5 Regulates IRP2 Stability in Iron Homeostasis via an Oxygen-Responsive [2Fe2S] Cluster. *Mol. Cell* **78**, 31-41.e5 (2020).
4. D. Kessler, J. Papenbrock, Iron–sulfur cluster biosynthesis in photosynthetic organisms. *Photosynth. Res.* **86**, 391–407 (2005).
5. D. C. Johnson, D. R. Dean, A. D. Smith, M. K. Johnson, Structure, function, and formation of biological iron-sulfur clusters. *Annu. Rev. Biochem.* **74**, 247–281 (2005).
6. T. A. Link, "The Structures of Rieske and Rieske-Type Proteins" in *Advances in Inorganic Chemistry*, A. G. Sykes, Ed. (Academic Press, 1999), pp. 83–157.
7. T. A. Rouault, The role of iron regulatory proteins in mammalian iron homeostasis and disease. *Nat. Chem. Biol.* **2**, 406–414 (2006).

8. F. W. Outten, E. C. Theil, Iron-Based Redox Switches in Biology. *Antioxid. Redox Signal.* **11**, 1029–1046 (2009).
9. R. P. Sheridan, L. C. Allen, C. W. Carter, Coupling between oxidation state and hydrogen bond conformation in high potential iron-sulfur protein. *J. Biol. Chem.* **256**, 5052–5057 (1981).
10. A. Dey, *et al.*, Solvent tuning of electrochemical potentials in the active sites of HiPIP versus ferredoxin. *Science* **318**, 1464–1468 (2007).
11. C. L. Drennan, J. W. Peters, Surprising cofactors in metalloenzymes. *Curr. Opin. Struct. Biol.* **13**, 220–226 (2003).
12. H. Beinert, Iron-sulfur proteins: ancient structures, still full of surprises. *J. Biol. Inorg. Chem. JBIC Publ. Soc. Biol. Inorg. Chem.* **5**, 2–15 (2000).
13. H. Beinert, R. H. Holm, E. Münck, Iron-sulfur clusters: nature's modular, multipurpose structures. *Science* **277**, 653–659 (1997).
14. K. A. Johnson, M. F. J. M. Verhagen, P. S. Brereton, M. W. W. Adams, I. J. Amster, Probing the Stoichiometry and Oxidation States of Metal Centers in Iron−Sulfur Proteins Using Electrospray FTICR Mass Spectrometry. *Anal. Chem.* **72**, 1410–1418 (2000).
15. C.-W. Lin, J. W. McCabe, D. H. Russell, D. P. Barondeau, Molecular Mechanism of ISC Iron–Sulfur Cluster Biogenesis Revealed by High-Resolution Native Mass Spectrometry. *J. Am. Chem. Soc.* **142**, 6018–6029 (2020).
16. V. Katta, B. T. Chait, Observation of the heme-globin complex in native myoglobin by electrospray-ionization mass spectrometry. *J. Am. Chem. Soc.* **113**, 8534–8535 (1991).
17. M. T. Hay, R. M. Milberg, Y. Lu, Preparation and Characterization of Mercury and Silver Derivatives of an Engineered Purple Copper Center in Azurin. *J. Am. Chem. Soc.* **118**, 11976–11977 (1996).
18. J. A. Loo, Studying noncovalent protein complexes by electrospray ionization mass spectrometry. *Mass Spectrom. Rev.* **16**, 1–23 (1997).
19. C. P. Anderson, M. Shen, R. S. Eisenstein, E. A. Leibold, Mammalian iron metabolism and its control by iron regulatory proteins. *Biochim. Biophys. Acta BBA - Mol. Cell Res.* **1823**, 1468–1483 (2012).
20. M. L. Wallander, E. A. Leibold, R. S. Eisenstein, Molecular control of vertebrate iron homeostasis by iron regulatory proteins. *Biochim. Biophys. Acta BBA - Mol. Cell Res.* **1763**, 668–689 (2006).
21. K. L. Davidson, D. R. Oberreit, C. J. Hogan, M. F. Bush, Nonspecific aggregation in native electrokinetic nanoelectrospray ionization. *Int. J. Mass Spectrom.* **420**, 35–42 (2017).
22. K. Giles, J. P. Williams, I. Campuzano, Enhancements in travelling wave ion mobility resolution. *Rapid Commun. Mass Spectrom.* **25**, 1559–1566 (2011).
23. S. J. Allen, K. Giles, T. Gilbert, M. F. Bush, Ion mobility mass spectrometry of peptide, protein, and protein complex ions using a radio-frequency confining drift cell. *The Analyst* **141**, 884–891 (2016).
24. G. Li, S. Zheng, Y. Chen, Z. Hou, G. Huang, Reliable Tracking In-Solution Protein Unfolding via Ultrafast Thermal Unfolding/Ion Mobility-Mass Spectrometry. *Anal. Chem.* **90**, 7997–8001 (2018).
25. T. J. El-Baba, *et al.*, Melting Proteins: Evidence for Multiple Stable Structures upon Thermal Denaturation of Native Ubiquitin from Ion Mobility Spectrometry-Mass Spectrometry Measurements. *J. Am. Chem. Soc.* **139**, 6306–6309 (2017).

26. Peifeng. Hu, Q.-Zhuang. Ye, J. A. Loo, Calcium Stoichiometry Determination for Calcium Binding Proteins by Electrospray Ionization Mass Spectrometry. *Anal. Chem.* **66**, 4190–4194 (1994).
27. G. J. Van Berkel, F. Zhou, J. T. Aronson, Changes in bulk solution pH caused by the inherent controlled-current electrolytic process of an electrospray ion source. *Int. J. Mass Spectrom. Ion Process.* **162**, 55–67 (1997).
28. S. Hong, M. F. Bush, Collision-Induced Unfolding Is Sensitive to the Polarity of Proteins and Protein Complexes. *J. Am. Soc. Mass Spectrom.* **30**, 2430–2437 (2019).
29. S. J. Allen, A. M. Schwartz, M. F. Bush, Effects of Polarity on the Structures and Charge States of Native-Like Proteins and Protein Complexes in the Gas Phase. *Anal. Chem.* **85**, 12055–12061 (2013).

Chapter 3: Collision-Induced Unfolding Is Sensitive to the Polarity of Proteins and Protein Complexes

This chapter is reproduced with permission from Hong, Seoyeon; Bush, Matthew F. “Collision-Induced Unfolding Is Sensitive to the Polarity of Proteins and Protein Complexes” *Journal of American Society of Mass Spectrometry* 2019. DOI: 10.1021/jasms.8b06263.

3.1 Abstract

Collision-induced unfolding (CIU) uses ion mobility to probe the structures of ions of proteins and noncovalent complexes as a function of the extent of gas-phase activation prior to analysis. CIU can be sensitive to domain structures, isoform identities, and binding partners, which makes it appealing for many applications. Almost all previous applications of CIU have probed cations. Here, we evaluate the application of CIU to anions and compare the results for anions with those for cations. Towards that end, we developed a “similarity score” that we used to quantify the differences between the results of different CIU experiments and evaluate the significance of those differences relative to the variance of the underlying measurements. Many of the differences between anions and cations that were identified can be attributed to the lower absolute charge states of anions. For example, the extents of the increase in collision cross section over the full range of energies depended strongly on absolute charge state. However, over intermediate energies there are significant difference between anions and cations with the same absolute charge state. Therefore, CIU is sensitive to the polarity of protein ions. Based on these results, we propose that the utility of CIU to differentiate similar proteins or noncovalent complexes may also depend on polarity. More generally, these results indicate the relationship

between the structures and dynamics of native-like cations and anions deserve further attention and that future studies may benefit from integrating results from ions of both polarities.

3.2 Introduction

In native mass spectrometry (MS), native-like ions are generated using electrospray ionization of proteins, nucleic acids, lipids, and/or other biological molecules in aqueous solutions. Native-like ions can retain noncovalent interactions that were present in solution and therefore native MS can probe the oligomeric state (1), topology (2), and stability (3) of biomolecular complexes in solution. This information can be particularly valuable when the biomolecular complex is too large or small, heterogeneous, or dynamic for other structural tools such as nuclear magnetic resonance, X-ray crystallography, and cryo electron microscopy. For example, native MS of hepatitis B virus capsid proteins provides evidence for complete capsids containing 180 and 240 subunits (4), consistent with high-resolution characterization, as well as the stoichiometry of antigen-binding domain binding (5) and mechanisms of the assembly process (6, 7), which would have been challenging to investigate using conventional techniques.

Most native MS experiments have probed native-like cations, although some properties of native-like anions have been investigated (8–11). Typically, native-like anions have lower absolute charge states than the corresponding cations generated from the same solutions (9, 10). This systematic difference has been attributed to different extents of charge-carrier emission during the final stages of desolvation (10), with lower emission energies and therefore greater numbers of competitive emission events (12) for anions. An atomic-level understanding of the structural differences between cations and anions remains elusive. One obvious difference is that native-like anions, $[M–nH^+]^{n–}$, are proton deficient, whereas native-like cations, $[M+nH^+]^{n+}$, are proton rich. Even though these difference will affect hydrogen bonding, salt bridges, and other

noncovalent interactions within the ion (13, 14), the collision cross section (Ω) values determined using ion mobility (IM) MS of native-like ions of medium- to large-mass proteins and protein complexes appear to depend weakly on charge state (10, 15) and polarity (10). This suggests that the structural differences between native-like anions and cations may be modest, highly localized, and/or beyond the resolution of current IM measurements.

Collisional activation of native-like ions can result in the loss of nonspecific adducts, changes in conformation, and eventually dissociation (16). Monitoring changes in conformation (collision-induced unfolding, CIU (17)) and extents of dissociation (collision-induced dissociation, CID) as a function of energy can provide information that is complementary to the associated IM and MS characterization of minimally activated ions. For example, CIU can be sensitive to charge state (18–20), domain structure (21), isoform identity (22), and ligand binding (23–26). Consequently, there is great interest in using CIU "fingerprints" to differentiate similar proteins (22, 24, 27, 28), particularly in cases where the associated native MS and native IM-MS data are not sensitive to those difference. For example, native-like cations of IgG subclasses with different disulfide bonding have similar Ω values, but exhibit unique CIU features upon the activation (22). Almost all applications of energy-dependent native MS have probed native-like cations. Based on the similarity of the results from CIU of 21+ and 21– ions of serum amyloid P (SAP) pentamers, Hall and coworkers reported that "the conformation and the gas-phase behavior during collisional activation are the same for SAP pentamer, regardless of whether it has an excess of positive or negative charges" (20). For complexes between cholera toxin B subunit homopentamers and five GM1 pentasaccharide ligands, CID of cations results predominantly in the loss of a protein subunit (without a ligand), whereas CID of anions results predominantly in the loss of a ligand (without a protein) (29). These differences suggest that the

CID products are a consequence of polarity-dependent structural changes that occur in the gas phase prior to dissociation (29).

It is challenging to assess the general utility of CIU to differentiate similar proteins or complexes because negative results, *i.e.*, cases where CIU is not sensitive to those differences, are usually not reported. Here, in order to broaden the potential utility of CIU, we demonstrate the application of CIU to anions and compare the results for anions with those for cations. Towards that end, we developed a "similarity score" that we use to quantify the differences between the results of different CIU experiments and evaluate the significance of those differences relative to the variance of the underlying measurements.

3.3 Experimental Methods

Sample Preparation

Avidin from egg white (A2667, Invitrogen, Carlsbad, CA) and β-lactoglobulin A from bovine milk (product number L7880, Sigma-Aldrich Co., St. Louis, MO) were each buffer exchanged into aqueous 200 mM ammonium acetate at pH 7.0 using centrifugal concentrators (10 kDa MWCO, Spin-X UF, Corning, Inc.) and a centrifuge operated at 4 ºC. For charge-reduction experiments, ions were generated from an aqueous solution containing 50 mM trimethylamine and 200 mM ammonium acetate.

Ion Mobility Mass Spectrometry and Collision-Induced Unfolding

Samples were each loaded into glass capillaries with inner diameters of 0.78 mm that were pulled to approximately 1 to 3 μm on one end using a micropipette puller (P-97, Sutter Instruments, Novato, CA). 10 μM protein sample was loaded onto the glass capillary. Electrical contact with the solution was achieved by inserting a platinum wire electrode into the wide end of the capillary (30). To minimize analyte carryover between samples, the electrode was washed

with aqueous 25% HCl (v:v) and rinsed with ultrapure (18.2 MΩ) water. Data were acquired using a Waters Synapt G2 HDMS hybrid mass spectrometer (Waters Co., Wilmslow, UK) (31) in which the traveling-wave IM cell was replaced with a radio-frequency (RF) confining drift cell (32) that contained 1.7 Torr He. To preserve the noncovalent interactions, the following instrument parameters were used: capillary voltage, ~ 1.0 kV; sampling cone, 20 V; extraction cone, 5 V; source temperature, ~ 30 ºC; and trap collision energy, 4 V. To determine the mobilities of minimally activated ions, those ions were introduced into the RF-confining drift cell that was operated using at least 9 drift voltages ranging from 104 to 354 V (32). Ω values of minimally activated ions and the mobility-independent transport times of ions (t_0) were determined from the slopes of plots of drift time versus reciprocal drift voltage as described previously (32). For CIU experiments, ions were accelerated prior to entering the trap cell using a range of trap injection voltages from 4 to 61 V with the RF confining drift cell operated at a drift voltage of 104 V.

Data Analysis

Mass spectra were analyzed using MassLynx v4.1 (Waters, Co., Milford, MA). Arrival-time distributions were extracted and analyzed using in-house software (33). The intensities of each arrival-time distribution were normalized so that their sum equals one. To aid in the comparison of IM data, arrival-time distributions were converted to apparent Ω distributions and then interpolated along a common Ω axis. The axes used for avidin and β-lactoglobulin contained 1000 and 500 points, respectively.

3.4 Results

3.4.1 Effects of Polarity on the Mass Spectra and Ion Mobility of Native-Like Ions

Figure 3.1a shows a representative native mass spectrum of avidin that was measured while operating the instrument in positive ion mode and exhibits peaks that are assigned to the 17+, 16+, 15+, and 14+ tetramers of avidin. This spectrum and these assignments are consistent with many examples in the literatures (10, 34). Figure 3.1b shows the analogous spectrum obtained in negative ion mode, which exhibits peaks that are assigned to the 14–, 13–, and 12– tetramers of avidin. The difference in the absolute charge states observed for the two polarities is similar to that reported previously (10). However, we are not aware of any other reports of native-like anions of avidin in the literature that could be used for comparison. The relative lack of analogous spectra of anions can partially be attributed to the propensity of corona discharge at the tip of electrospray emitters in negative ion mode (35). However, corona discharge was rare in the present experiments, which may be attributable to the low onset voltage for electrospray in this implementation (30).

The native-like cations and anions of avidin were also analyzed using IM-MS, which revealed that the median Ω ($\widetilde{\Omega}$) values of these ions are all similar to each other (Table S1, determined from cumulative distribution function of each apparent Ω distribution as shown in Figure S3.1). These results corroborate previous results suggesting that gas-phase structure can depend weakly on charge and polarity under native-like conditions (10, 20). However, similar Ω values for native-like cations and anions does not preclude possible differences of anions and cations that are not resolved in these IM measurements. To investigate the potential differences between the cations and anions, we subjected avidin ions to CIU.

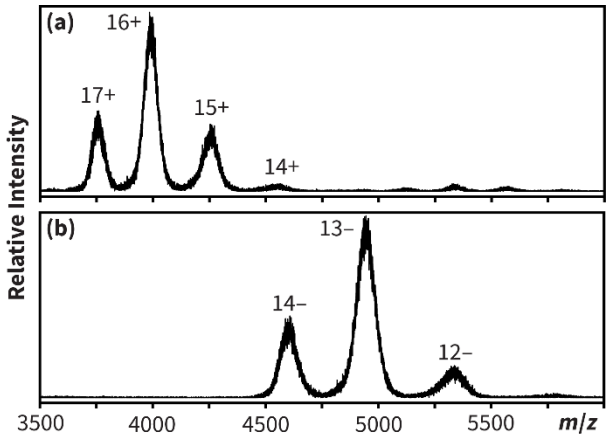

Figure 3.1. Native mass spectra of avidin in positive (a) and negative (b) polarity obtained from an aqueous solution of 200 mM ammonium acetate at pH 7.0. The predominant peaks are assigned to tetramers, with charge states as labeled. The weak signals at higher *m*/*z* are assigned to dimers of the avidin tetramer, which is attributed to nonspecific aggregation during electrospray ionization [30].

3.4.2 Effects of Polarity on the Collision-Induced Unfolding of Native-Like Ions

Selected charge states of native-like cations and anions of avidin were subjected to CIU by varying their laboratory-frame kinetic energy as they enter the trap cell that is positioned immediately prior to the IM cell. Laboratory-frame energy is the product of the voltage used to inject ions in the trap cell and the absolute value of charge state of the ion (36). The resulting products were then separated by IM and the resulting apparent Ω distributions are shown in Figure 3.2. The initial distributions are similar for all charge states, consistent with the $\widetilde{\Omega}$ values discussed above. With increasing energy, features appear that are attributed to partially unfolded and mostly unfolded structures, consistent with a previous study of native-like cations of avidin (34). Although features for folded, partially unfolded, and mostly unfolded avidin ions are observed in all cases, the appearance energy and Ω of these features appear to depend on charge state and polarity to varying extents. Differences are most apparent for the partially unfolded ions. Aspects of these differences will be quantified and discussed in more detail below.

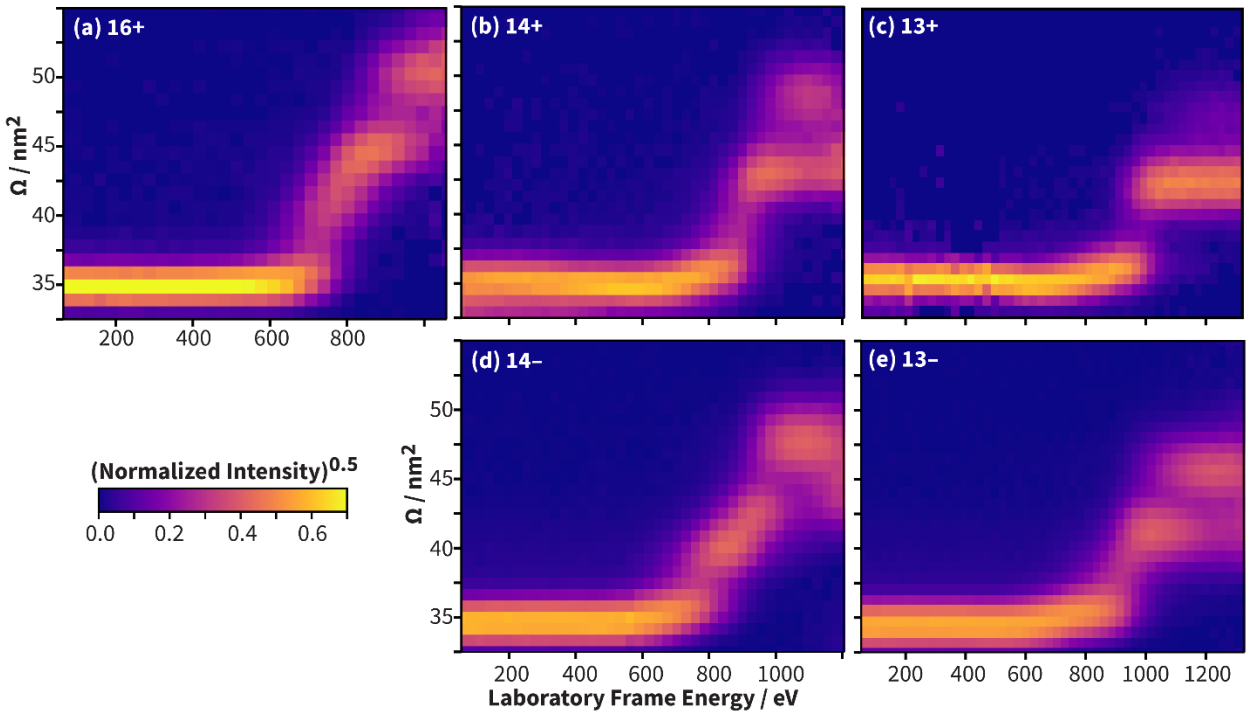

Figure 3.2. Results from collision-induced unfolding (CIU) of selected charge states of the avidin tetramer. Ions were generated from an aqueous solution containing 200 mM ammonium acetate, except the 13+ ions were generated from a solution that also contained 50 mM trimethylamine. The heat maps display the Ω distributions as a function of laboratory frame energy, based on data acquired using 2 V increments of the trap injection voltage. Laboratory frame energy was increased until the precursor was depleted due to dissociation.

Even though the Ω distributions at low energies are similar for charge states characterized in both polarities, the distributions formed at the highest energies appears to exhibit decreasing magnitudes with decreasing absolute charge state (Figure 3.2). Figure 3.3 shows the $\widetilde{\Omega}$ values at the highest (Figure S3.2) and lowest (Figure S3.1) energies for each species. The $\widetilde{\Omega}$ values at high energy increase with absolute charge states, which is consistent with visual inspection of the CIU data (Figure 3.2). The $\widetilde{\Omega}$ value at high energy for the 14– ions is slightly greater than that for the 14+ ions. Because these are the only ions with the same absolute charge state that are observed in both polarities, it is challenging to draw more general conclusions about the effects of polarity on the maximum expansion of protein ions by CIU. In order to further investigate the effects of polarity separately from charge state, trimethylamine was added to an avidin sample, which was then analyzed in positive ion mode. In these experiments, trimethylamine acts as a charge-reducing agent (37) and enables the formation of 13+ avidin ions. Interestingly, $\widetilde{\Omega}$ value at high energy for the 13– ions is less than that for the 13+ ions. However, the binding of trimethylamine is evidenced by the mass spectra shown in Figure S3.3; the centroids of the peaks in the originating from the sample with trimethylamine correspond to masses that are ~556 Da heavier (equivalent to nearly 10 molecules of trimethylamine) than those originating from the sample without trimethylamine. Based on these results alone, we are unable to conclude whether the differences are a consequence of polarity or the presence of trimethylamine in the sample used to generate the cations. Therefore, this topic will require further investigation in the future.

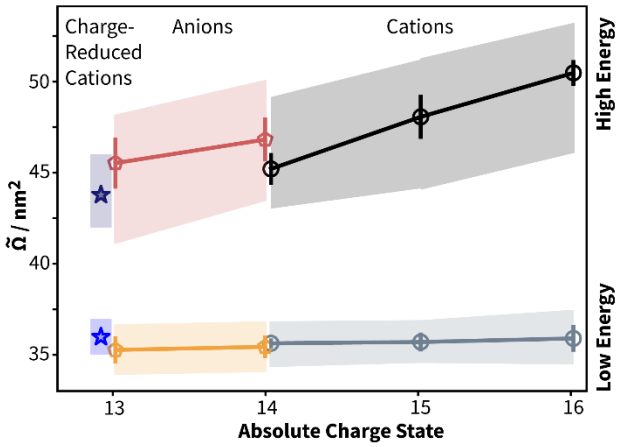

Figure 3.3. The median **Ω** ($\widetilde{\Omega}$) value at low (20 V) and high (16+: 64 V, 15+: 68 V, 14+: 86 V, 13+: 118 V, 14-:86 V, 13-:100 V) trap injection voltage. Each marker represents the average of the $\widetilde{\Omega}$ values determined for three intendent technical replicates. The vertical bars span the 95% confidence interval of the replicates. The upper and low bound of the shaded region represent the **Ω** values at 90% and 10% of the cumulative distribution function respectively, as shown in Figures S3.1 and S3.2.

Although the differences between the $\widetilde{\Omega}$ values at high energies 14+ and 14– are subtle, the CIU results for these ions appear to exhibit more significant differences over intermediate energies (Figures 3.2b and 3.2d). For comparison, the apparent **Ω** distributions for these ions at selected energies are shown in Figure S3.4. To highlight the differences between the CIU results for these ions of opposing polarity, the difference between those results is plotted in Figure 3.4a. For comparison, Figures 3.4b and 3.4c shows the difference between the **Ω** distribution of two independent replicates of 14+ and 14– ions, respectively. Although the magnitudes of the differences between replicate analyses of ions of the same polarity (Figures 3.4b and 3.4c) are less than the differences between analyses of ions of different polarity (Figure 3.4a), it was challenging to interpret these differences using these plots alone. For example, the differences at low energies appear as red and blue streaks, but it appears that those differences are the consequence of very slight differences in underlying distributions (*e.g.*, Figure S3.4a) and that the distributions may have been undersampled in the original experiments. However, both the difference plot (Figure 3.4a) and the individual **Ω** distributions (Figure S3.4) indicate that the greatest differences occur over intermediate energies, in the region associated with partially unfolded structures.

In order to quantitatively compare the apparent **Ω** distributions underlying these CIU results, we developed a similarity score that depends on the dot products of the pair of distributions and the dot products of duplicate distributions. The similarity score of the distributions for ions α and β is defined as:

$$Similarity\ Score = \frac{1}{2}\left(\frac{I_\alpha \cdot I_\beta}{I_\alpha \cdot I_\alpha} + \frac{I_\alpha \cdot I_\beta}{I_\beta \cdot I_\beta}\right) \qquad \text{(Equation 3.1)}$$

where I_α and I_β are the intensities of the distribution for α and β, respectively. Possible scores range between zero and one. A similarity score of one indicates that the two distributions are

identical. Conversely, differences in the two distributions will result in similarity scores that are less than one. Figure 3.4d shows the similarity scores as a function of laboratory frame energy determined from CIU analysis of 14+ and 14− avidin ions, *i.e.*, where α and β have different polarities. This trace is near one for energies <600 eV and near 950 eV, but decreases to significantly lower values near 840 and 1050 eV. Figures S3.4a to S3.4e show representative apparent Ω distributions of 14+ and 14− avidin ions at 56, 840, 924, 1036, and 1288 eV. Visual inspection of the distributions at each energy provides context for interpreting the scores determined using Equation 3.1 and corroborates the preceding evaluation of similarity/difference based only on similarity scores. The results demonstrate the utility of this score for quantifying the similarity between two distributions and identifying the laboratory frame energies that yield the greatest differences for samples from different classes.

Figures 3.4e and 3.4f plot the similarity score traces determined for the same data used for the analysis in Figures 3.4b and 3.4c, respectively. These traces illustrate typical similarity scores for comparisons between members of the same class. Relative to the traces determined when α and β have the opposite polarity, these traces are largely independent of energy. To provide context for this data and illustrate sources of variance, Figures S3.5 and S3.6 show apparent Ω distributions and similarity scores at selected energies for two pairs of technical replicates. Figure S3.5 shows that the results for a pair of technical replicates selected for the anions have similarity scores that range from 0.97 to 0.99. At intermediate energies, it appears that a slightly greater fraction of the ions in one replicate have unfolded than in the other, but the differences between the two replicates are very subtle. Figure S3.6 shows that the results for a pair of technical replicates selected for the cations have similarity scores that range from 0.96 to 0.99. Those slightly lower values appear to be a consequence of a systematic ~1 nm^2 difference

in Ω between the two replicates, which were acquired four months apart. Systematic differences could be reduced by acquiring data for different samples on the same day or by standardizing the mobility data (33).

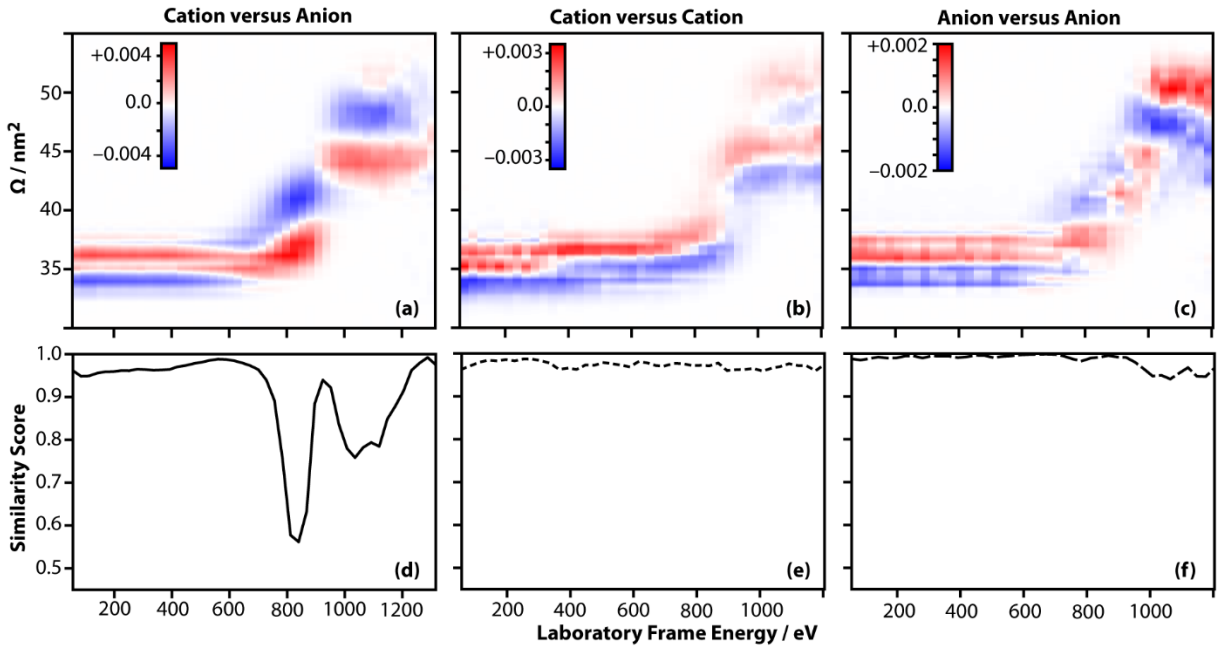

Figure 3.4. (a) The differences between the CIU intensities for 14+ and 14– avidin from native-like conditions. Reds indicate greater relative intensities for the cations (positive values), whereas blues indicate greater relative intensities for the anions (negative values). The differences between the CIU intensities based on two independent technical replicates of 14+ and 14– avidin are shown in (b) and (c), respectively. (d) The similarity scores (Equation 1) for the apparent Ω distributions of 14+ and 14– avidin used for (a). The similarity scores for the apparent Ω distributions used for (b) and (c) are plotted in (e) and (f), respectively.

Figure 3.5 show similarity score traces that were determined for many independent CIU analyses of 14+ and 14− ions. These results clearly show that the differences between the CIU results for ions of different polarities are significantly greater than the differences between technical replicates for ions of the same polarity. That is, even though the $\widetilde{\Omega}$ values at the lowest and the highest energies depend subtly on polarity, the Ω values of the ions generated at intermediate energies depend strongly on polarity. An alternative method for analyzing these results is CIU Suite 2 (38). For example, Figure S3.7 shows the comparison plot and RMSD values generated using that method, default settings, and the same experimental data used for Figure 3.4. The RMSD value for ions of different polarity (25%, Figure S3.7A) is larger than those for ions of the same polarity (10%, Figures S3.7B and S3.7C). By comparison, the similarity scores in Figure 3.5 (1) exhibit far larger differences between ions of different polarity and ions of the same polarity and (2) directly indicate the energies that are most useful for differentiating between species of interest.

In order to evaluate whether other proteins also exhibit polarity-dependent differences, CIU was used to characterize monomers of β-lactoglobulin, which has a mass of 18.4 kDa. Figure S3.8 shows the native mass spectra of the 7+ and 7− ions, and that features for unadducted protein ions (*i.e.*, no nonspecific adducts) are resolved in both polarities. Unadducted forms of these ions were each quadrupole selected (Figure S3.8) and subjected to CIU. Unadducted ions are preferred for these experiments because previous studies have shown that that ions subjected to CIU can be stabilized through interactions with nonspecific adducts (34, 39, 40); unfortunately this was not possible in the preceding example due to presence of multiple glycoforms of avidin (41) and other challenges associated with native MS of higher mass proteins, including decreased apparent resolving power associated with broader isotope

distributions (42), increased binding of nonspecific adducts (43), and increased scattering with background gas during time-of-flight mass analysis. Figure S3.9a shows the apparent Ω distributions of 7+ and 7− ions as a function of laboratory frame energy, which reveals very different CIU fingerprints. For example, at 518 eV the 7− anions exhibit a bimodal Ω distribution that is significantly broader than that for the 7+ cations (Figure S3.4f). The similarity scores are plotted in Figure S3.9b and indicate that the differences between the results for the anions and cations increase with increasing laboratory frame energy. These results for β-lactoglobulin complement those for avidin and provide further support that the CIU of native-like ions can depend on polarity.

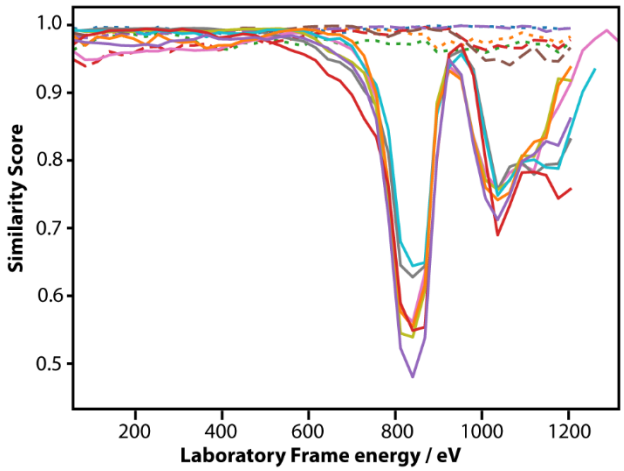

Figure 3.5. Similarity scores of results for 14+ and 14– avidin ions (solid lines) determined from unique pairs of three replicate CIU analyses of 14+ and 14– avidin. Similarity scores for unique pairs of replicate CIU analyses of 14+ (dotted lines) and 14– (dashed lines) avidin.

3.4.3 Effects of Polarity on CID Efficiency

The highest energies used for CIU of the avidin tetramer also resulted in CID, yielding monomers and trimers of avidin (Figure S3.10). The Figure 3.6a shows the survival yield of quadrupole-selected tetramers ions:

$$Survival\ Yield = \frac{\sum I(tetramers)}{\sum I(monomers)+\sum I(trimers)+\sum I(tetramers)} \qquad \text{(Equation 3.2)}$$

The survival yield of the tetramer decreases with increasing laboratory frame energy as a consequence of the formation of monomers and trimers (Figure S3.10). Activation of the precursor ions also results in the appearance of charge-reduced and higher-charge ions (Figure S3.11 and S3.12); such charge-transfer products have been reported previously (44). In general, anions exhibit greater propensity for charge stripping than the corresponding cations (Figure S3.13). Note that survival yields were calculated using all ions observed for each oligomeric state, including any charge-transfer products.

To help compare the stability of each precursor during CID, we determined "LFE_{50}" values, which are defined as the laboratory frame energy that results in a survival yield of 50%. These values for all charge states and both polarities are plotted in Figure 6b. Note that in some cases charge-stripped tetramers may have the same *m*/*z* as some trimers. The likelihood of this occurring is greatest for the anions, which exhibit the greatest extent of charge stripping. In order to estimate the possible contributions from such interferences, we calculated LFE_{50} values for the 13– and 14– ions assuming that the ambiguous ions are entirely trimers (the lower limit) or charge-stripped tetramers (the upper limit). The lower and upper limits of the LFE_{50} for 14– avidin are 1077 and 1089 eV, respectively. Those limits for 13– avidin are 1141 and 1191 eV, respectively. Since these ranges are small, we did not evaluate this possibility further and use the upper limits in the following discussion.

Overall, the CID efficiency for the native-like anions is less than that of the native-like cations, which to some extent is a consequence of the lower absolute charge states for the former. Figure 3.6b shows that the LFE_{50} of 14– avidin is higher than that of the 14+ avidin by 43 eV. 14+ and 14– avidin possess the same charge state but may differ in the presence of mobile protons or charge carriers. For context, numerous studies have concluded that CID of multiprotein complexes involves charge migration to one of the protein subunits, which leads to unfolding and the subsequent ejection of that subunit (20, 45–49). Therefore, it is possible that less efficient charge migration in anions, which are proton deficient, may also contribute to their lower CID efficiency. There may be additional consequences of the number of protons in these ions and the concomitant differences in the number of hydrogen bonds and salt bridges (13) present in their structures.

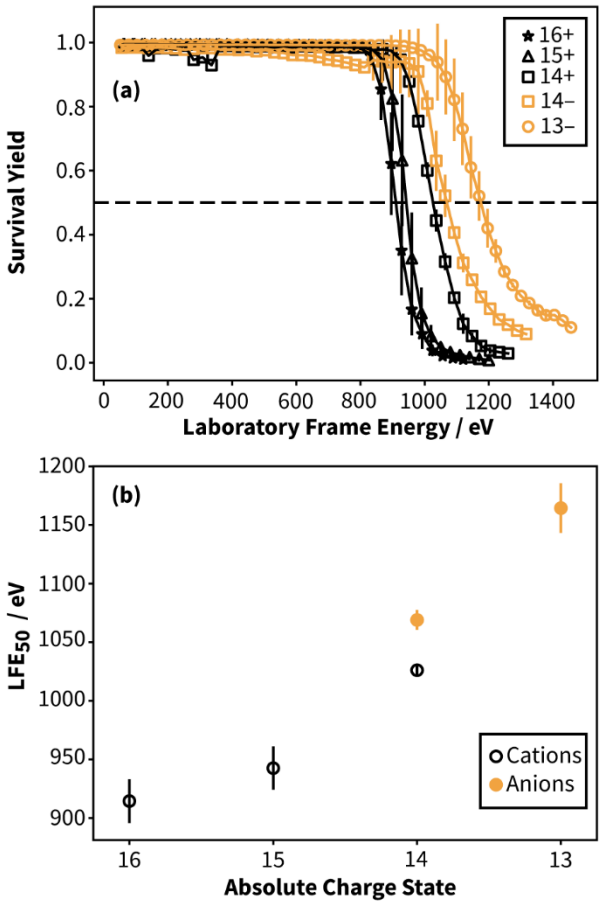

Figure 3.6. Results from collision-induced dissociation (CID) of avidin ions from native-like conditions. Representative mass spectra are shown in Figure S3.10. (a) Survival yield of the precursor ions as function of laboratory frame energy. The bars span the 95% confidence interval of three independent technical replicates. Note that replicates were not collected for laboratory frame energies that are far greater or lower than the LFE_{50}. (b) LFE_{50} for each charge state is shown in both polarities. The bars span the 95% confidence interval based on three independent technical replicates.

3.5 Conclusions

Native-like anions and cations of the avidin tetramer were probed using IM-MS, CIU, and CID. Visual inspection of the CIU data for avidin (Figure 3.2) indicate that there are differences between the results for anions and cations. To analyze the significance of those differences, we developed a "similarity score" (Equation 3.1) that we used to quantify the differences between results for ions of difference polarities relative to the differences between results for technical replicates of the same polarity (Figure 3.5). Many of the differences between anions and cations that were identified can be attributed to the lower absolute charge states of anions (Figure 3.1). For example, the extents of increase in $\widetilde{\Omega}$ values over the full range of energies depended strongly on absolute charge state (Figure 3.3). However, over intermediate energies there are significant difference between anions and cations with the same absolute charge state (Figures 3.4, 3.5, and S3.4). Differences between the CIU of anions and cations of β-lactoglobulin were also observed and characterized (Figure S3.9). These results all indicate that CIU is sensitive to the polarity of protein ions. The CID efficiency of avidin ions also appears to depend on polarity (Figure 3.6). Characterizing the differences between these properties for additional multiprotein complexes may enable more general insights into the role of charge mobility on dissociation of multiprotein complexes.

Very few native IM-MS experiments have probed anions. Based on results for a selected set of proteins and protein complexes, we reported previously that native-like cations and anions (with minimal activation) can have very similar $\boldsymbol{\Omega}$ values and suggested that there was "no inherent benefit to selecting a specific polarity for capturing a more native-like structure" (10). Because the present results indicate that the CIU of equally charged ions is sensitive to polarity, we propose that the utility of CIU to differentiate similar proteins or noncovalent complexes may

depend on polarity. Therefore, we recommend that analyte polarity should be considered during the development of native IM-MS methods for specific applications. More generally, these results indicate the relationship between the structures and dynamics of native-like cations and anions deserve further attention and that future studies may benefit from integrating results from ions of both polarities.

3.6 Acknowledgements.

This material is based upon work supported by the National Science Foundation under CHE-1807382 (M. F. B.).

3.7 Supporting Information.

Tables S3.1, Figures S3.1 to S3.13.

3.8 References

1. F. Stengel, *et al.*, Dissecting Heterogeneous Molecular Chaperone Complexes Using a Mass Spectrum Deconvolution Approach. *Chem. Biol.* **19**, 599–607 (2012).
2. A. J. R. Heck, Native mass spectrometry: a bridge between interactomics and structural biology. *Nat. Methods* **5**, 927–933 (2008).
3. A. El-Hawiet, *et al.*, Quantifying Ligand Binding to Large Protein Complexes Using Electrospray Ionization Mass Spectrometry. *Anal. Chem.* **84**, 3867–3870 (2012).
4. C. Uetrecht, *et al.*, High-resolution mass spectrometry of viral assemblies: Molecular composition and stability of dimorphic hepatitis B virus capsids. *Proc. Natl. Acad. Sci.* **105**, 9216–9220 (2008).
5. J. Z. Bereszczak, *et al.*, Sizing up large protein complexes by electrospray ionisation-based electrophoretic mobility and native mass spectrometry: morphology selective binding of Fabs to hepatitis B virus capsids. *Anal. Bioanal. Chem.* **406**, 1437–1446 (2014).
6. C. Uetrecht, I. M. Barbu, G. K. Shoemaker, E. van Duijn, A. J. R. Heck, Interrogating viral capsid assembly with ion mobility–mass spectrometry. *Nat. Chem.* **3**, 126 (2010).
7. C. A. Lutomski, *et al.*, Hepatitis B Virus Capsid Completion Occurs through Error Correction. *J. Am. Chem. Soc.* **139**, 16932–16938 (2017).
8. L. Konermann, D. J. Douglas, Unfolding of proteins monitored by electrospray ionization mass spectrometry: a comparison of positive and negative ion modes. *J. Am. Soc. Mass Spectrom.* **9**, 1248–1254 (1998).
9. A. J. R. Heck, R. H. H. van den Heuvel, Investigation of intact protein complexes by mass spectrometry. *Mass Spectrom. Rev.* **23**, 368–389 (2004).

10. S. J. Allen, A. M. Schwartz, M. F. Bush, Effects of Polarity on the Structures and Charge States of Native-Like Proteins and Protein Complexes in the Gas Phase. *Anal. Chem.* **85**, 12055–12061 (2013).
11. I. Liko, J. T. S. Hopper, T. M. Allison, J. L. P. Benesch, C. V. Robinson, Negative Ions Enhance Survival of Membrane Protein Complexes. *J. Am. Soc. Mass Spectrom.* **27**, 1099–1104 (2016).
12. C. J. Hogan, J. A. Carroll, H. W. Rohrs, P. Biswas, M. L. Gross, Combined Charged Residue-Field Emission Model of Macromolecular Electrospray Ionization. *Anal. Chem.* **81**, 369–377 (2009).
13. R. R. O. Loo, J. A. Loo, Salt Bridge Rearrangement (SaBRe) Explains the Dissociation Behavior of Noncovalent Complexes. *J. Am. Soc. Mass Spectrom.* **27**, 975–990 (2016).
14. L. Konermann, Molecular Dynamics Simulations on Gas-Phase Proteins with Mobile Protons: Inclusion of All-Atom Charge Solvation. *J. Phys. Chem. B* **121**, 8102–8112 (2017).
15. K. J. Laszlo, M. F. Bush, Interpreting the Collision Cross Sections of Native-like Protein Ions: Insights from Cation-to-Anion Proton-Transfer Reactions. *Anal. Chem.* **89**, 7607–7614 (2017).
16. J. L. P. Benesch, Collisional activation of protein complexes: Picking up the pieces. *J. Am. Soc. Mass Spectrom.* **20**, 341–348 (2009).
17. S. M. Dixit, D. A. Polasky, B. T. Ruotolo, Collision induced unfolding of isolated proteins in the gas phase: past, present, and future. *Curr. Opin. Chem. Biol.* **42**, 93–100 (2018).
18. K. B. Shelimov, M. F. Jarrold, Conformations, Unfolding, and Refolding of Apomyoglobin in Vacuum: An Activation Barrier for Gas-Phase Protein Folding. *J. Am. Chem. Soc.* **119**, 2987–2994 (1997).
19. K. Pagel, S.-J. Hyung, B. T. Ruotolo, C. V. Robinson, Alternate Dissociation Pathways Identified in Charge-Reduced Protein Complex Ions. *Anal. Chem.* **82**, 5363–5372 (2010).
20. Z. Hall, A. Politis, M. F. Bush, L. J. Smith, C. V. Robinson, Charge-State Dependent Compaction and Dissociation of Protein Complexes: Insights from Ion Mobility and Molecular Dynamics. *J. Am. Chem. Soc.* **134**, 3429–3438 (2012).
21. Y. Zhong, L. Han, B. T. Ruotolo, Collisional and Coulombic Unfolding of Gas-Phase Proteins: High Correlation to Their Domain Structures in Solution. *Angew. Chem. Int. Ed.* **53**, 9209–9212 (2014).
22. Y. Tian, L. Han, A. C. Buckner, B. T. Ruotolo, Collision Induced Unfolding of Intact Antibodies: Rapid Characterization of Disulfide Bonding Patterns, Glycosylation, and Structures. *Anal. Chem.* **87**, 11509–11515 (2015).
23. J. T. S. Hopper, N. J. Oldham, Collision induced unfolding of protein ions in the gas phase studied by ion mobility-mass spectrometry: The effect of ligand binding on conformational stability. *J. Am. Soc. Mass Spectrom.* **20**, 1851–1858 (2009).
24. S.-J. Hyung, C. V. Robinson, B. T. Ruotolo, Gas-phase unfolding and disassembly reveals stability differences in ligand-bound multiprotein complexes. *Chem. Biol.* **16**, 382–390 (2009).
25. J. N. Rabuck, *et al.*, Activation state-selective kinase inhibitor assay based on ion mobility-mass spectrometry. *Anal. Chem.* **85**, 6995–7002 (2013).
26. Y. Zhao, *et al.*, A Traveling Wave Ion Mobility Spectrometry (TWIMS) Study of the Robo1-Heparan Sulfate Interaction. *J. Am. Soc. Mass Spectrom.* **29**, 1153–1165 (2018).
27. J. N. Rabuck-Gibbons, J. M. Lodge, A. K. Mapp, B. T. Ruotolo, Collision-Induced Unfolding Reveals Unique Fingerprints for Remote Protein Interaction Sites in the KIX

Regulation Domain. *J. Am. Soc. Mass Spectrom.* (2018) https:/doi.org/10.1007/s13361-018-2043-6 (September 10, 2018).
28. N. D. Wagner, D. E. Clemmer, D. H. Russell, ESI-IM-MS and Collision-Induced Unfolding That Provide Insight into the Linkage-Dependent Interfacial Interactions of Covalently Linked Diubiquitin. *Anal. Chem.* **89**, 10094–10103 (2017).
29. Y. Zhang, L. Deng, E. N. Kitova, J. S. Klassen, Dissociation of Multisubunit Protein–Ligand Complexes in the Gas Phase. Evidence for Ligand Migration. *J. Am. Soc. Mass Spectrom.* **24**, 1573–1583 (2013).
30. K. L. Davidson, D. R. Oberreit, C. J. Hogan, M. F. Bush, Nonspecific aggregation in native electrokinetic nanoelectrospray ionization. *Int. J. Mass Spectrom.* **420**, 34–42 (2016).
31. K. Giles, J. P. Williams, I. Campuzano, Enhancements in travelling wave ion mobility resolution. *Rapid Commun. Mass Spectrom.* **25**, 1559–1566 (2011).
32. S. J. Allen, K. Giles, T. Gilbert, M. F. Bush, Ion mobility mass spectrometry of peptide, protein, and protein complex ions using a radio-frequency confining drift cell. *The Analyst* **141**, 884–891 (2016).
33. M. F. Bush, I. D. G. Campuzano, C. V. Robinson, Ion mobility mass spectrometry of peptide ions: effects of drift gas and calibration strategies. *Anal. Chem.* **84**, 7124–7130 (2012).
34. J. Freeke, M. F. Bush, C. V. Robinson, B. T. Ruotolo, Gas-phase protein assemblies: Unfolding landscapes and preserving native-like structures using noncovalent adducts. *Chem. Phys. Lett.* **524**, 1–9 (2012).
35. P. J. McClory, K. Håkansson, Corona Discharge Suppression in Negative Ion Mode Nanoelectrospray Ionization via Trifluoroethanol Addition. *Anal. Chem.* **89**, 10188–10193 (2017).
36. J. Laskin, J. H. Futrell, Activation of large ions in FT-ICR mass spectrometry. *Mass Spectrom. Rev.* **24**, 135–167 (2005).
37. X. Zhuang, A. F. M. Gavriilidou, R. Zenobi, Influence of Alkylammonium Acetate Buffers on Protein–Ligand Noncovalent Interactions Using Native Mass Spectrometry. *J. Am. Soc. Mass Spectrom.* **28**, 341–346 (2017).
38. D. A. Polasky, S. M. Dixit, S. M. Fantin, B. T. Ruotolo, CIUSuite 2: Next-Generation Software for the Analysis of Gas-Phase Protein Unfolding Data. *Anal. Chem.* **91**, 3147–3155 (2019).
39. L. Han, S.-J. Hyung, J. J. S. Mayers, B. T. Ruotolo, Bound anions differentially stabilize multiprotein complexes in the absence of bulk solvent. *J. Am. Chem. Soc.* **133**, 11358–11367 (2011).
40. L. Han, S.-J. Hyung, B. T. Ruotolo, Bound Cations Significantly Stabilize the Structure of Multiprotein Complexes in the Gas-phase. *Angew. Chem. Int. Ed Engl.* **51**, 5692–5695 (2012).
41. R. J. DeLange, T. S. Huang, Egg white avidin. 3. Sequence of the 78-residue middle cyanogen bromide peptide. Complete amino acid sequence of the protein subunit. *J. Biol. Chem.* **246**, 698–709 (1971).
42. P. Lössl, J. Snijder, A. J. R. Heck, Boundaries of mass resolution in native mass spectrometry. *J. Am. Soc. Mass Spectrom.* **25**, 906–917 (2014).
43. J. L. P. Benesch, B. T. Ruotolo, D. A. Simmons, C. V. Robinson, Protein Complexes in the Gas Phase: Technology for Structural Genomics and Proteomics. *Chem. Rev.* **107**, 3544–3567 (2007).
44. F. Sobott, M. G. McCammon, C. V. Robinson, Gas-phase dissociation pathways of a tetrameric protein complex. *Int. J. Mass Spectrom.* **230**, 193–200 (2003).

45. N. Felitsyn, E. N. Kitova, J. S. Klassen, Thermal Decomposition of a Gaseous Multiprotein Complex Studied by Blackbody Infrared Radiative Dissociation. Investigating the Origin of the Asymmetric Dissociation Behavior. *Anal. Chem.* **73**, 4647–4661 (2001).
46. J. C. Jurchen, E. R. Williams, Origin of Asymmetric Charge Partitioning in the Dissociation of Gas-Phase Protein Homodimers. *J. Am. Chem. Soc.* **125**, 2817–2826 (2003).
47. J. C. Jurchen, D. E. Garcia, E. R. Williams, Further studies on the origins of asymmetric charge partitioning in protein homodimers. *J. Am. Soc. Mass Spectrom.* **15**, 1408–1415 (2004).
48. S. K. Fegan, M. Thachuk, A Charge Moving Algorithm for Molecular Dynamics Simulations of Gas-Phase Proteins. *J. Chem. Theory Comput.* **9**, 2531–2539 (2013).
49. V. Popa, D. A. Trecroce, R. G. McAllister, L. Konermann, Collision-Induced Dissociation of Electrosprayed Protein Complexes: An All-Atom Molecular Dynamics Model with Mobile Protons. *J. Phys. Chem. B* **120**, 5114–5124 (2016).

Chapter 4: Effects of Charge State and Polarity on Native-like Intact Antibody

4.1 Abstract

Analytical tools for characterizing the antibodies (Abs) are in high demand with increasing number of innovator antibody therapeutics and their biosimilars. The effects of charge state and polarity are evaluated for the native mass spectrometry (MS) and ion mobility (IM) – MS analysis of Abs using two samples of IgG2. These two samples are from the same subclass (IgG2), have the κ light chain, were each purified from human myeloma plasma, but were from different manufacturing origins. Native MS analysis of the two samples was used to determine the apparent mass and relative mass heterogeneity. Despite the similarities of the two samples, the native mass spectra were vastly different. Native IM-MS results demonstrate that the median Ω values ($\widetilde{\Omega}$) of native-like cations increased with increased by up to 9% with increasing, whereas the anions increase by up to 12% with increasing charge. The strong dependence of $\widetilde{\Omega}$ on charge may be due to large differences in structural populations; unimodal and bimodal Ω distributions were observed for different species. Interestingly, collision-induced unfolding (CIU) revealed that the greatest differences between the two samples were present at the lowest energies, with greater differences for anions than for cations. More generally, these results demonstrate the benefits of using cation and anions when developing native IM-MS and CIU methods for differentiating similar proteins.

4.2 Introduction

In native mass spectrometry (MS), native-like ions are formed from electrospray ionization. The native-like ions preserve noncovalent interactions present in the solution phase

and provide insights into topology (1), stoichiometry (2) and ligand binding (3) of biomolecular complexes. The information from native MS is insightful particularly for biomolecules that are too small, large, heterogeneous, dynamic for conventional structural techniques, such as standard nuclear magnetic resonance, x-ray crystallography, and cryo-electron microscopy. For instance, the composition of heterocomplex of the full-length small heat shock proteins, *Ps*HSP18.1 from pea and *Ta*HSP16.9 from wheat shows the molar ratio ranging from 1:6 and 6:1 respectively (4). Furthermore, the kinetic analysis using time dependent MS supports that the heterocomplexes exchanges primarily dimeric species consistent with the results from high-resolution structural technique (4).

In native MS, protein cations usually contain excess protons $[M+nH]^{n+}$ and protein anions are usually proton deficient $[M-nH]^{n-}$. Although proteins in solution may be positively or negatively changed, most native MS studies probe protein cations. The magnitude of charge states depends on polarity; the average charge state of the protein anions is lower than those for the corresponding cations formed from the same solution conditions (5, 6). The lower average charge state of anions has been attributed to different extents of charge-carrier emission (7). In native ion mobility (IM) analysis, native-like conformations are preserved by minimizing solution denaturation (8, 9) and instrumental activation of the ions. The collision cross section (Ω) of many "medium-to-large" size protein ions are independent of the charge state and polarity (5, 10) under native conditions. This suggests that the structural differences between native-like cations and anions are highly localized and/or beyond the resolution of the current IM resolution.

Collision-induced unfolding (CIU) of proteins induces the unfolding of protein complexes by increasing their internal energy. CIU probes the Ω distributions as a function of energy. Previous studies demonstrated that CIU is sensitive to polarity (11), charge state (11, 12),

PTMs (13, 14), ligand binding (15, 16), domain structure (17), subclasses (18) and mutation (19). For example, our previous study demonstrated that the Ω of native-like 14+ and 14− AVD appear very similar at low energy. However, the structural differences between the cations and anions are elicited upon CIU (11).

Monoclonal antibodies (mAb) are glycoproteins that belongs to immunoglobulin (Ig) family. Therapeutic mAbs are widely used to treat cancer (20), autoimmune disease (21), neural (22) and infectious diseases (23) in humans. The mAb product is consisting of heterogeneous population due to PTMs such as glycosylation (24, 25), pyroglutamate formation (26), and deamidation (27), and charge on the surface (28). These sources of heterogeneity can significantly affect the function (29, 30) and structure (31) of mAbs. The full-length mAb is too dynamic for structural analysis and only a few complete structures of full-length mAbs have been solved using X-ray crystallography (32–34). Consequently, most studies investigate fragments of mAb such as the antigen-binding fragment of the mAb complexed with its binding partner (35–37).

IM-MS may be a useful tool to investigate the structural analysis of mAb. Previous study reported that the gas-phase structure of native mAb (IgG1κ) cations shows more compact conformations by Ω than the theoretical Ω values using the crystal structure (38, 39). This has been attributed to contraction near the hinge region (39), whereas the antigen binding domain, most secondary structure and tertiary folding are maintained. The Ω of native-like IgG1κ displays nearly 3% difference in Ω over the range of five sequential charge states (38). In this study, we investigate the effects of charge and polarity on the structures of antibodies (Abs) using two samples of IgG2. Additionally, we evaluate the utility of CIU on differentiating the two samples.

4.3 Experimental Methods

Sample preparation for native and deglycosyalted IgG

For native MS experiments, IgG2κ from human myeloma plasma was acquired from Sigma Aldrich (I5404, abbreviated as ^{S}IgG2κ) and Athens Research and Technology (16-16-090707-2M, abbreviated as ^{A}IgG2κ) and buffer exchanged into 200 mM ammonium acetate at pH 7.0 using Micro Bio-Spin™ P-6 Gel Columns (Bio-Rad) at 4 ºC. ADH (Sigma Aldrich, A7011) is buffer exchanged into 200 mM ammonium acetate at pH 7.0. PNGase F (New England Biolabs, P0705S) was used for N-linked deglycosylation of ^{S}IgG2κ and ^{A}IgG2κ. The nondenaturing protocol suggested by the manufacturer was followed. The samples containing the enzyme were incubated at 44 ºC overnight. The control samples included all the elements for the deglycosylation reaction except the enzyme. The deglycosylated and control samples were buffer exchanged using centrifugal concentrators (10 kDa MWCO, Spin-X UF, Corning, Inc.)

MS and Ion mobility Experiments

10 μM of protein samples were loaded into glass capillaries with inner diameters of 0.78 mm that were pulled approximately 1 to 3 μm on one end using a micropipette puller (P-97, Sutter Instruments, Novato, CA). Electrical contact was attained by inserting a Pt wire into the wide end of the capillary. In order to minimize potential sources of adducts and carryover between experiments, the Pt wire was washed with 25% HCl (v/v) and rinsed with ultrapure (18.2 MΩ) water. All the experiments were conducted on a Waters Synapt G2 HDMS hybrid mass spectrometer (Waters Co., Wilmslow, UK) (40) in which the traveling wave IM cell has been replaced with an rf-confining drift cell (41), which contained ~ 1.7 torr He for all mobility experiments. The experimental parameters for native MS experiments are the followings: capillary voltage, ~ 1.0 kV; sampling cone, 20 V; extraction cone, 5 V; source temperature, ~

30 °C; and trap collision energy, 4 V. To determine the mobilities of minimally activated ions, those ions were introduced into the RF-confining drift cell that was operated using drift voltages ranging from 104 to 354 V (41). For CIU experiments, mobility results are acquired for a range of trap injection voltage in 4 V increments ranging from 4 to 200 V and 10 to 198 V, for Abs and ADH, respectively.

CAPTR experiments with RF-confining drift cell

Cation-to-anion proton-transfer-reactions (CAPTR) were performed on the same instrument, which has a glow-discharge ionization source (42) containing perfluoro-1,3-dimethylcyclohexane (PDCH, Sigma Aldrich)(43). The source block at the interface between the ambient pressure and vacuum regions of the instrument was heated to 120 ºC, which prevents the buildup of reagent in the source but also has been shown to transfer some heat to the sample (44). The $[\mathrm{PDCH} - \mathrm{F}]^-$ anions were generated using glow-discharge ionization. The anion was selected at *m*/*z* 381 using quadrupole and was accumulated in the trap cell for 100 ms followed by the polarity switch to positive ion mode. For the following 1 s, positively charged protein ions were transmitted into the trap cell and reacted with $[\mathrm{PDCH} - \mathrm{F}]^-$ to induce CAPTR.

Data Analysis

Mass spectra was extracted using MassLynx v4.1 (Waters, Co., Milford, MA). Arrival-time distributions were extracted using in-house software(45). The Ω and mobility-independent transport time (t_0) of distributions that appeared unimodal were determined from the slope of drift time versus reciprocal drift voltage as described previously (41). The drift time used to calculate the Ω and t_0 of distributions that did not appear unimodal were analyzed by using the median Ω values ($\widetilde{\Omega}$), which were determined from 50% of the cumulative distribution function

of the arrival-time distribution (44). The intensity of Ω distributions are normalized so that the sum of the intensity equals one. The similarity score for CIU experiments was analyzed as previously described (11). In order to compared CIU results using similarity score, drift time were converted to apparent Ω axis and then interpolated along a common 1000-point Ω axis.

4.4 Results

4.4.1 Native MS of IgG2

Figures 4.1a and 4.1b show the native mass spectra of ^{S}IgG2 in positive and negative ion mode, respectively. The average charge states of ^{S}IgG2 in positive and negative ion mode are 24 and 21, respectively. The peak width of ^{S}IgG2 is greater for anions than cations. This indicates that anions contain greater presence of adducts than the cations, which has been observed previously for other native-like protein anions (11). The native cations and anions both display peaks that appear unimodal. The apparent mass corresponds to approximately 154 kDa in both polarities. Though the apparent mass is approximate, it is distinct from that determined for IgGs of other subclasses (Figure S4.1). The resolution of the peaks may be limited by relatively broad isotopic distributions of mAb, presence of non-specifically bound adducts, less efficient desolvation (46) due to the large size, decreased TOF resolving power (47) and increased TOF scattering with the background gas during the TOF analysis. Together with the broad peak width and heterogeneity of mAb reported by others (28, 29), the presence of multiple species with similar masses cannot be precluded. The heterogeneity of ^{S}IgG2 is further investigated in *Deglycosylation of IgG2 Abs* (*vide infra*).

Figures 4.1c and 4.1d show the native spectra of ^{A}IgG2 in positive and negative ion modes. The ^{A}IgG2 and ^{S}IgG2 display similar properties such as same subclass (IgG2) from human myeloma plasma and κ light chain, but produced from different manufacturing origins.

The average charge states of ^{A}IgG2 in positive and negative ion mode are 26 and 22, respectively. The native MS shows apparent bimodal peaks that correspond to approximately 157 and 159 kDa in both polarities. This indicates that the apparent mass of ^{A}IgG2 is greater than ^{S}IgG2 by approximately 3 to 5 kDa. In addition, the bimodal peak shape of ^{A}IgG2 in native MS demonstrates that the heterogeneity of ^{A}IgG2 may be greater than ^{S}IgG2.

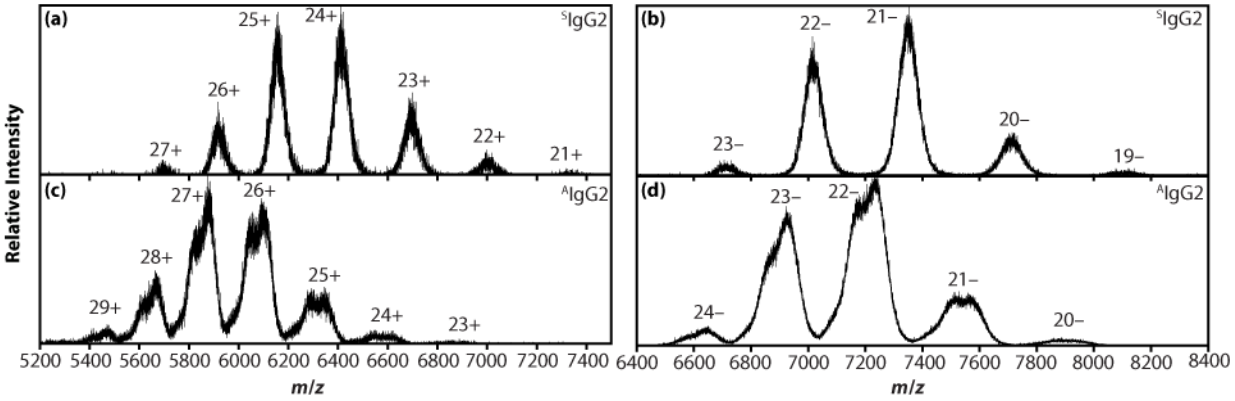

Figure 4.1. Native mass spectra of ^{S}IgG2 (a) and ^{A}IgG2 (b) acquired in positive ion mode. The corresponding spectra acquired in negative ion mode are shown in (b) and (c), respectively. The apparent mass of ^{S}IgG2 is 154 kDa in both polarities. The apparent mass of ^{A}IgG2 is 157 and 159 kDa in both polarities. All ions were formed from aqueous 200 mM ammonium acetate at pH 7.0.

4.4.2 Deglycosylation of IgG2 Abs

The N-linked glycosylation is one of the most-commonly observed PTMs in Abs. Therefore, the effects of deglycosylation provides insights into the heterogeneity by glycosylation. Figure 4.2a shows the mass spectrum of deglycosylated ^{S}IgG2. Figure S2 shows the control MS of ^{S}IgG2 that underwent the same conditions as for deglycosylation reaction, except lacking the presence of the enzyme. The control MS (Figure S4.2a) contrasts with Figure 4.2a and ensures that the features observed in Figure 4.2a are solely deglycosylated species of ^{S}IgG2. In addition, the signal for the deglycosylated (Figure 4.2a) appear at similar *m*/*z* as the intact ^{S}IgG2 (Figure 4.1a) so that the features by deglycosylation are not induced by incubation conditions used for the deglycosylation reactions. The deglycosylated species of ^{S}IgG2 are noted as ^{S}α, ^{S}β and ^{S}γ (Figure 4.2a). The apparent mass of ^{S}α, ^{S}β and ^{S}γ is determined from CAPTR (cation-to-anion-proton-transfer-reaction) (48) (Figure S4.3). Figure S4.3a shows that the selected 26+ ^{S}γ generate charge-reduced species (CAPTR product ions) via CAPTR. The apparent mass of ^{S}γ (~151 kDa) is determined using the CAPTR product ions. Figure S4.3b shows that the precursor ions for ^{S}α and ^{S}β appeared unimodal, but CAPTR of the precursor effectively differentiated ^{S}α and ^{S}β where the charge reduction increases *m*/*z* spacing between the two species. The apparent mass of ^{S}α and ^{S}β are ~148 and 149 kDa respectively. The percent composition of the deglycosylate species (^{S}α, ^{S}β and ^{S}γ) are calculated to evaluate the effects of glycosylation on the mass heterogeneity of the intact ^{S}IgG2. The percent composition of ^{S}γ relative to ^{S}α, ^{S}β and ^{S}γ is ~95% indicating that deglycosylation of ^{S}IgG2 primarily results in one species.

Figure 4.2b shows the spectrum of deglycosylated ^{A}IgG2. CAPTR of deglycosylated ^{A}IgG2 (Figure S4.4) identified three species, which are noted as ^{A}δ, ^{A}ε and ^{A}ζ in Figure 4.2b. The

control MS (Figure S4.2b) shows that the emergence of $^{A}\delta$, $^{A}\varepsilon$ and $^{A}\zeta$ (Figure 4.2b) are solely attributed to deglycosylation. Since the $^{A}\varepsilon$ and $^{A}\zeta$ exhibit a mass difference of 0.9 kDa and are partially resolved, the percent composition of $^{A}\varepsilon$ and $^{A}\zeta$ relative to the sum of $^{A}\delta$, $^{A}\varepsilon$ and $^{A}\zeta$ is calculated and corresponds to 46.9% for the 25+ charge state. This indicates that ^{A}IgG2 is consisting of three species distinguished by glycosylation with a relatively more even abundance and therefore, the apparent heterogeneity by glycosylation for ^{A}IgG2 may be larger than ^{S}IgG2.

The extent of glycosylation is compared between ^{S}IgG2 and ^{A}IgG2. The extent of glycosylation is the mass difference between mass of deglycosylated species and the respective intact IgG2. The extent of glycosylation of ^{A}IgG2 may range from 4 to 8.5 kDa, which is 2.5 – 5.7% of the intact ^{A}IgG2. The glycosylation by $^{S}\gamma$ (the primary deglycosylated ^{S}IgG2) accounts for 1.9% of the intact mass. This shows that the intact ^{A}IgG2 is relatively more glycosylated compared to ^{S}IgG2. However, the mass of the deglycosylated ^{A}IgG2 (149 – 152 kDa) and ^{S}IgG2 (148 - 151 kDa) are identical (Figure 4.2). This indicates that the two samples may also vary by other kinds of PTMs (24–27) and/or composition of primary amino acid.

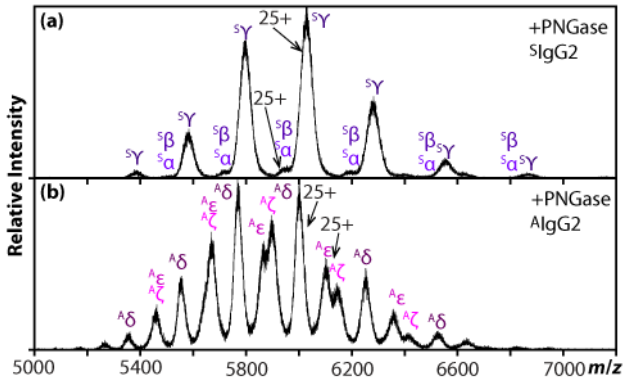

Figure 4.2. Spectra of the deglycosylated (a) ^{S}IgG2 and (b) ^{A}IgG2. (a) ^{S}α, ^{S}β, and ^{S}γ indicate three deglycosylated species of ^{S}IgG2. Based on results from CAPTR (Figure S4.3), the masses of ^{S}α, ^{S}β, and ^{S}γ are 148, 149, and 151 kDa, respectively. (b) ^{A}δ, ^{A}ε and ^{A}ζ indicate three deglycosylated species of ^{A}IgG2. Based on results from CAPTR (Figure S4.4), the masses of ^{A}δ, ^{A}ε and ^{A}ζ are 150, 153, and 153 kDa, respectively.

4.4.3 Native IM-MS of IgG2

Figure 4.3a shows the Ω distributions of native-like ^{S}IgG2 in both polarities. The Ω distributions display apparent unimodal distributions. The Ω values increase with increasing charge state indicating that the structures of native-like ^{S}IgG2 adopt more larger conformations. Additionally, the peak width of Ω distributions increases with increasing *z*. This suggests that the structural heterogeneity of native-like ^{S}IgG2 increases with increasing *z*. The $\widetilde{\Omega}$ of native-like ^{S}IgG2 is determined as described in *Data Analysis* and plotted in Figure 4.3c. The $\widetilde{\Omega}$ increases up to 11% from the 20− to the 27+ charge states. To better understand the effects of polarity and *z*, the linear regression was used to correlate the $\widetilde{\Omega}$ values and the |*z*| (Figure 4.3c). The slope indicates the rate of the $\widetilde{\Omega}$ change by charge state. The slopes are 0.8 and 1.2 nm^2 for cations and anions respectively. This suggests that the structures of the ^{S}IgG2 anions increase $\widetilde{\Omega}$ by charge state than the cations by a factor of 1.5. As result, the $\widetilde{\Omega}$ increases up to 4% (from 23+ to 27+), while the anions increase up to 6% (from 20− to 23−). Since the anions display relatively more compact conformations than the cations *i.e* increasing the nocovalent interactions within the Abs, increasing *z* may more significantly disrupts the noncovalent interactions and induces a greater expansion of the structures. To the best of our knowledge, the dependence of Ω of native-like Abs on the charge states for the anions has not been reported previously. The demonstrates that the consideration of charge state and polarity may be useful for native IM-MS analysis of native-like Abs.

For context, the strong relationship between charge state and Ω observed for ^{S}IgG2 is not observed for most globular native-like protein ions (5, 10). For example, alcohol dehydrogenase (ADH) has a mass (~150 kDa) and exhibits similar charge state as most Abs. However, the $\widetilde{\Omega}$ of native-like ADH (Figure 4.3c) does not depend on charge state. The changes of structures of

native-like ^{S}IgG2 by charge state may be attributed to the flexible regions of Abs that enable to adopt a wide range of conformations. However, non-globular shape of the proteins does not guarantee the Ω dependence on *z* at low energy. For example, the pentameric serum amyloid P (SAP) contains a large central cavity and the Ω depends on *z* at low energy (49). Therefore, the Ω dependence on *z* of native-like ^{S}IgG2 may be facilitated by the flexible hinge region that enables a wide range of conformations with varying charge states.

Figure 4.3b shows that the Ω distributions of ^{A}IgG2. The Ω distributions of the anions display bimodal distributions, indicating the presence of at least two structures. However, these bimodal features disappear with increasing $|z|$ and increasingly displays unimodal distributions. This suggests that increasing $|z|$ enables the more compact conformations in the bimodal distributions to rapidly isomerize into larger structures. The $\widetilde{\Omega}$ of ^{A}IgG2 is shown in Figure 4.3c. The linear regression is fitted to the $\widetilde{\Omega}$ to understand the effects of *z* for each polarity (Figure 4.3c). The slope of the cations corresponds to 1.2 nm^2 , resulting in the increase of $\widetilde{\Omega}$ by 9% (from 23+ to 28+). The slope of the anions is 1.7 nm^2 and is correlated to the $\widetilde{\Omega}$ increase to 12% (from 19− to 24−). This indicates that the $\widetilde{\Omega}$ increase by *z* is greater for the anions than the cations by a factor of ~1.4. The greater increase of $\widetilde{\Omega}$ for the anions by *z* is associated with the rapid isomerization to larger structures with increasing *z* partly indicated by disappearance of bimodal distributions.

The $\widetilde{\Omega}$ of ^{A}IgG2 and ^{S}IgG2 are different for ions of the same charge states indicating that the structures of native-like ^{A}IgG2 and ^{S}IgG2 are distinct from each other. For example, the comparison of $\widetilde{\Omega}$ of 23+ ^{A}IgG2 than ^{S}IgG2 exhibits only up to 0.71% difference and may undermine the difference between ^{A}IgG2 than ^{S}IgG2 elicited using 22− charge state that shows

about 7.3% difference (Figure 4.3c). The difference in the apparent mass, mass heterogeneity and the extent of glycosylation (*vide supra*) may be attributed to induce distinct conformations of Abs under native conditions. The slopes of the linear regression are greater for ^{A}IgG2 than ^{S}IgG2 for the anions and cations respectively by a factor of 1.6 and 1.4. This indicates that the structures of ^{A}IgG2 enlarges due to increasing *z* to a greater extent than ^{S}IgG2. Since the structures of the Abs varies by polarity and *z*, consideration of the *z* and polarity may enhance the **Ω** comparison of native-like ^{A}IgG2 and ^{S}IgG2 or other native-like Abs with the similar properties.

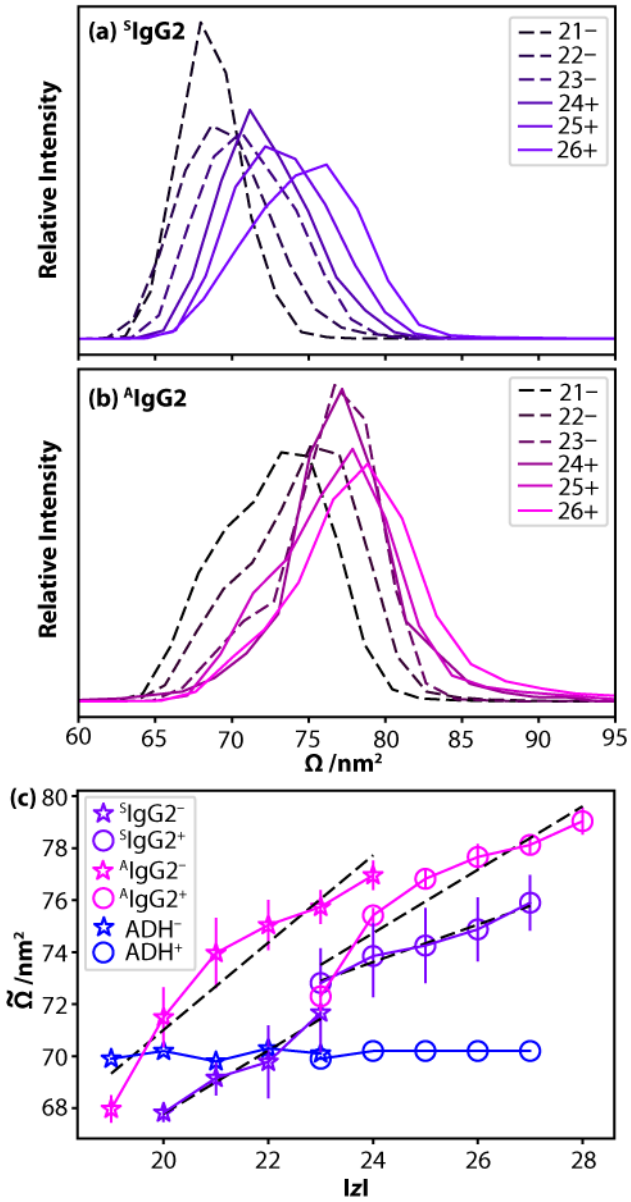

	SIgG2	AIgG2
Anions	$\tilde{\Omega}$=1.2|z| + 43 R^2=0.96	$\tilde{\Omega}$=1.7|z| + 37 R^2=0.91
Cations	$\tilde{\Omega}$=0.8|z| + 56 R^2=0.98	$\tilde{\Omega}$=1.2|z| + 45 R^2=0.89

Figure 4.3. Native-like **Ω** of ^{S}IgG2 and ^{A}IgG2. The **Ω** distributions of (a) ^{S}IgG2 and (b) ^{A}IgG2 at trap injection voltage of 4 V. The anions and cations are plotted in dotted (---) and solid (−) lines respectively. (c) The $\tilde{\Omega}$ of anions (☆) and cations (○) of ^{S}IgG2, ^{A}IgG2 and ADH(5) are plotted.

Each marker represents the average of the $\widetilde{\Omega}$ of three independent technical replicates. Linear regression of the results for the anions and cations is indicated by dotted black lines. The equations for the fitted linear regression and the R^2 values are shown below. The error bars indicate the standard deviation of the $\widetilde{\Omega}$ of three independent technical replicates.

4.4.4 CIU of IgG2

Selected charge states of ^{S}IgG2 ions were injected into the trap cell with a wide range of laboratory frame energy. Laboratory frame energy is the product of the trap injection voltage and the charge state. CIU analysis of ^{S}IgG2 ions monitors the conformational changes observe by **Ω** as a function of laboratory frame energy (Figure 4.4). The **Ω** of the most compact conformation is observed at low energy. The **Ω** of the most compact conformation increases with increasing charge state consistent with results discussed in *Native IM-MS of IgG*. Interestingly, the anions of ^{S}IgG2 exhibit further compaction with increasing energy. This suggests that the ions of lower charge states may adopt more compact conformations upon activation less inhibited by coulombic unfolding compared to ions of higher charge states. Alternatively, a previous report suggests that activation of the pentameric serum amyloid P (SAP) of low charge states induces compaction due to collapse of the ring-like topology (49). Therefore, it may be possible that the ^{S}IgG2 anions may contain cavity-like region that collapses upon the activation.

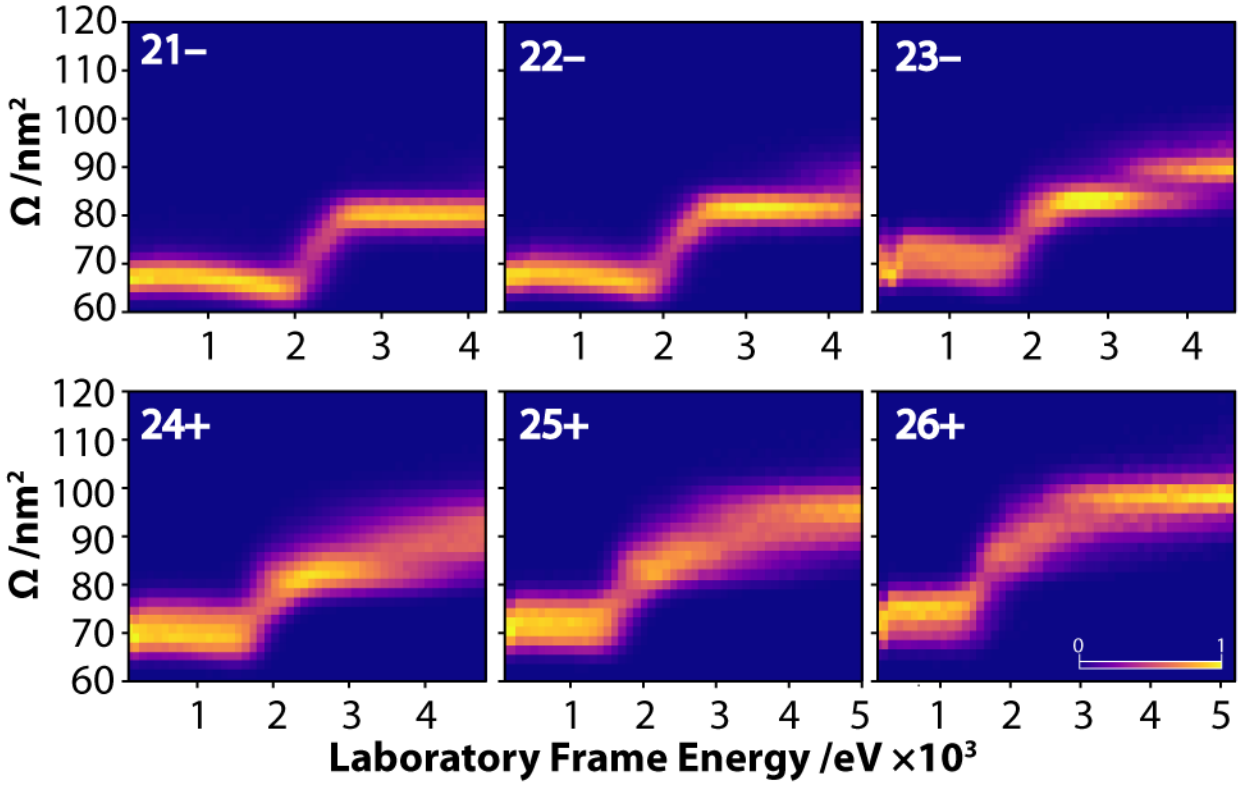

Figure 4.4. Results of CIU of selected charge states of native ^{S}IgG2 precursor ions. The heatmap exhibits apparent Ω distributions as a function of laboratory frame energy in 4 V increment from 4 – 200 V.

The CIU of ^{S}IgG2 is further characterized by comparing to the CIU of ADH (Figure S4.5). The CIU fingerprints of ^{S}IgG2 (Figure 4.4) and ADH (Figure S4.5) show that the unfolding stability of ^{S}IgG2 is greater than ADH, which display continuous increase in Ω with increasing energy. The extent of unfolding stability is quantified by $\frac{\widetilde{\Omega}_{max}}{\widetilde{\Omega}_{\min}}$, where $\widetilde{\Omega}_{max}$ and $\widetilde{\Omega}_{min}$ correspond to the $\widetilde{\Omega}$ at the highest and lowest laboratory-frame energy, respectively (Figure 4.5). The $\frac{\widetilde{\Omega}_{max}}{\widetilde{\Omega}_{\min}}$ of ^{S}IgG2 and ADH increase with increasing *z* (Figure 4.5). The $\frac{\widetilde{\Omega}_{max}}{\widetilde{\Omega}_{\min}}$ of ADH is greater than ^{S}IgG2 for the ions of the same charge states. For instance, $\frac{\widetilde{\Omega}_{max}}{\widetilde{\Omega}_{\min}}$ of ADH is 1.41 and 1.58 for 21- and 25+ charge states respectively, while the overall extent of unfolding for ^{S}IgG2 is 1.19 and 1.33 for 21- and 25+ charge states respectively. The higher $\frac{\widetilde{\Omega}_{max}}{\widetilde{\Omega}_{\min}}$ of ADH is attributed to continuous unfolding in the intermediate energy (Figure S4.5). The difference in the unfolding stability of ^{S}IgG2 may be attributed to the flexible region of ^{S}IgG2 that enable the ^{S}IgG2 to adopt a wide range of conformations of the similar **Ω**. Alternatively, the quaternary structure of ADH (consisting of homotetramers via noncovalent interactions) may be inefficient in stabilizing the ions the subunits compared to the ^{S}IgG2, a monomeric protein.

The CIU results of ^{A}IgG2 (Figure S4.6) is used to obtain $\frac{\widetilde{\Omega}_{max}}{\widetilde{\Omega}_{\min}}$ (Figure 4.5). The $\frac{\widetilde{\Omega}_{max}}{\widetilde{\Omega}_{\min}}$ of ^{A}IgG2 increases with increasing *z* (Figure 4.5). The $\frac{\widetilde{\Omega}_{max}}{\widetilde{\Omega}_{\min}}$ of ^{S}IgG2 and ^{A}IgG2 are relatively similar to each other compared to ADH. For example, the difference of $\frac{\widetilde{\Omega}_{max}}{\widetilde{\Omega}_{\min}}$ of ^{S}IgG2 and ^{A}IgG are 0.07 and 0.05 for 21− and 25+ charge states respectively. On the contrary, the difference of $\frac{\widetilde{\Omega}_{max}}{\widetilde{\Omega}_{\min}}$ of ADH and ^{S}IgG2 are 0.2 and 0.3 for 21− and 25+ charge states respectively. The visual inspection of the ^{S}IgG2 and ^{A}IgG CIU fingerprints confirms that the CIU of the samplesare

similar to each other than ADH. This indicates that the greater CIU stability than ADH is consistently observed for both samples.

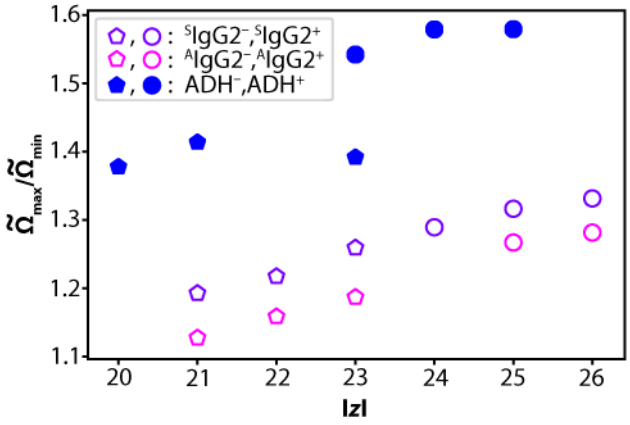

Figure 4.5. The $\frac{\widetilde{\Omega}_{max}}{\widetilde{\Omega}_{min}}$ of CIU of ^{S}IgG2 and ^{A}IgG2. The $\widetilde{\Omega}_{max}$ and $\widetilde{\Omega}_{min}$ represent the average of the $\widetilde{\Omega}$ values of three independent technical replicates at 200 and 4 V for ^{S}IgG2 and ^{A}IgG2. The $\frac{\widetilde{\Omega}_{max}}{\widetilde{\Omega}_{min}}$ of the cations (○) and anions (⬠) of ^{S}IgG2 and ^{A}IgG2 are plotted. The $\widetilde{\Omega}_{max}$ and $\widetilde{\Omega}_{min}$ of ADH cations (●) and anions (⬟) are the $\widetilde{\Omega}$ values at 198 and 10 V respectively. The standard deviation of $\widetilde{\Omega}_{max}$ and $\widetilde{\Omega}_{min}$ of ^{S}IgG2 and ^{A}IgG2 is within 3% of the respective $\widetilde{\Omega}$ values.

Since the $\frac{\tilde{\Omega}_{max}}{\tilde{\Omega}_{\min}}$ compares the **Ω** at the lowest and highest energy, the CIU results for ^{S}IgG2 and ^{A}IgG2 are quantitatively compared for the entire energy range (Figure 4.6 and Figure S4.7) using a "similarity score", which has been previously described in detail (11). Identical **Ω** distributions result in similarity score of exactly 1. However, dissimilarity between the **Ω** distributions decreases the similarity score from 1. Figure 4.6a shows the similarity score analysis comparing 22− ^{S}IgG2 and ^{A}IgG2 comparison. The similarity score in the low energy range (88 – 1500 eV) shows the greatest dissimilarity indicated by the lowest score (~0.6). The **Ω** distributions of 22− ^{S}IgG2 and ^{A}IgG2 (Figure S4.9) only partially overlap at the low energy. Additionally, the similarity score comparing the technical replicates (Figure 4.6a and Figure S4.8a) do not interfere the comparison between the samples in the low energy range (88 – 1500 eV). Therefore, the low energy range may be utilized to compare the structures of 22− ^{S}IgG2 and ^{A}IgG2 *i.e* the native IM-MS analysis is sufficient to effectively differentiate the two samples.

The similarity score increases with increasing energy indicating that the structures of 22− ^{S}IgG2 and ^{A}IgG2 isomerize into the similar structures. For example, Figure 4.6a shows that the similarity score reaches approximately one at ~2000 eV confirmed by very similar **Ω** distributions of the two samples (Figure S4.8b and Figure S4.9b). The similarity score at the highest energy range (~2000 – 4400 eV), but interfered by decreased reproducibility (Figure S4.8c). The decreased reproducibility at high energy may be attributed to varying stability of the samples amongst technical replicates or binding of nonspecific adducts (50) that is beyond the resolution of the TOF. Therefore, the comparison of 22− ^{S}IgG2 and ^{A}IgG2 is not further pursued. The largest difference in the low energy is observed for anions of other charge states (Figure S4.7) without the interference by reproducibility.

Figure 4.6b shows the similarity score analysis of 25+ ^{S}IgG2 and ^{A}IgG2. Figure 4.6b shows that the similarity score comparing the 25+ ^{S}IgG2 and ^{A}IgG2 exhibits the lowest score (~0.6 to 0.85) at the low energy range (100 – 1800 eV). Figure S4.9d confirms that the Ω distributions of 25+ ^{S}IgG2 and ^{A}IgG2 indeed show distinct difference. However, the comparison in this energy range is also interfered by decreased reproducibility (Figure 4.6b and Figure S4.7). The decreased reproducibility is continuously observed at the intermediate energy (2000 – 3500 eV) (Figure 4.6b, Figure S4.8e and Figure S4.9e) until the 25+ ^{S}IgG2 and ^{A}IgG2 isomerize into similar structures at the highest energy range (3500 – 5000 eV) (Figure 4.6b and Figure S4.9f). Generally, the extent of difference in the low energy range is more modest for cations than any of the anions (Figure S4.7). Additionally, the CIU results of the cations are disadvantaged from decreased reproducibility.

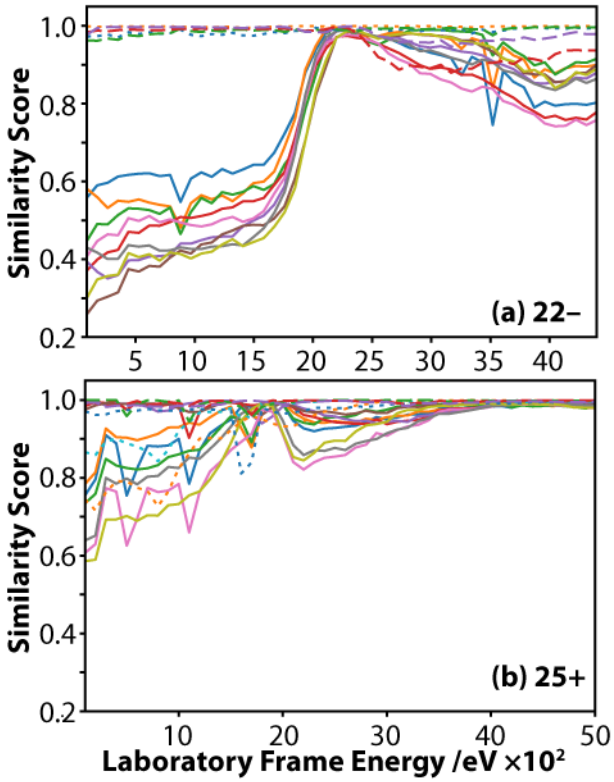

Figure 6. Similarity score (11) comparing unique pairs of triplicate CIU results of (a) 22− and (b) 25+ ^{S}IgG2 and ^{A}IgG2. The solid lines indicate the comparison between ^{S}IgG2 and ^{A}IgG2. The dashed (---) and dotted (···) indicate the similarity score comparing the technical replicates of ^{S}IgG2 and ^{A}IgG2, respectively.

4.5 Conclusions

Native-like ^{S}IgG2 and ^{A}IgG2 are probed using native MS, native IM-MS and CIU. ^{S}IgG2 and ^{A}IgG2 are Abs that have the that have κ light chain and are both extracted from human myeloma plasma but have different manufacturing origins. The native IM-MS analysis shows that *z* and polarity affect the **Ω** of the samples. This result is very different than that obtained for other native-like protein ions using similar experimental methods (41), including ADH (Figure 4.3). The strong relationship between **Ω** and *z* and polarity may be attributed to the presence of flexible hinge region that enable Abs to adopt a wide range of conformations. The rate of **Ω** increase with *z* is greater for the anions than the cations for both samples. These results show that the consideration of *z* and polarity may enhance the utility of native IM-MS analysis of mAbs with similar properties or biosimilar mAbs. These structural differences of native-like Abs observed may be attributed to the difference in the apparent mass, relative mass heterogeneity (Figure 4.1) and glycosylation (Figure 4.2) observed using native MS.

The CIU analysis is useful to distinguish these two samples from eachother (Figure 4.4 and S4.6), as well as from proteins with different properties such as ADH (Figure S4.5) (Figure 4.5). The similarity score comparing CIU results of ^{S}IgG2 and ^{A}IgG2 demonstrates that the mAbs are most effectively differentiated at low energy range using anions (Figure 4.6). These results indicate that comparison between the mAbs with similar properties are sensitive to energy *z*, and polarity. The CIU fingerprints of the Abs and ADH are vastly different from each other across the entire energy range for several ions except 20– ^{A}IgG2 and most anions of ^{S}IgG2 at the low energy range. The comparison of the CIU results of the Abs and ADH demonstrates that the

Abs are more stable than ADH, possibly due to the presence of the flexible hinge region in the Abs.

The present study explores the effects of *z*, polarity and energy on native-like Abs using IM-MS analysis. Unlike most proteins that have been analyzed using IM-MS (41), the structures of native-like mAbs depend on *z* and polarity. The native IM-MS analysis of these samples suggests that consideration of *z* and polarity may enhance native IM-MS analysis of Abs, and more specifically, analysis of Abs with similar properties or biosimilar mAbs. In addition to *z* and polarity, these CIU results indicate that the comparison between structures of Abs is sensitive to energy, *z* and polarity. More generally, these results indicate that the consideration of *z*, polarity and energy may be important to understand the structures and dynamics of native-like Abs. Furthermore, the broader considerations of *z*, polarity and energy may enable improve native IM-MS methods controlling the quality of and differentiating similar mAbs.

4.6 Acknowledgements

This material is based upon work supported by the National Science Foundation under CHE-1807382 (M. F. B.).

4.7 Supporting Information

Figures S4.1 to S4.9.

4.8 References

1. A. Sahasrabuddhe, *et al.*, Confirmation of intersubunit connectivity and topology of designed protein complexes by native MS. *Proc. Natl. Acad. Sci.* **115**, 1268–1273 (2018).
2. M. G. McCammon, H. Hernández, F. Sobott, C. V. Robinson, Tandem Mass Spectrometry Defines the Stoichiometry and Quaternary Structural Arrangement of Tryptophan Molecules in the Multiprotein Complex TRAP. *J. Am. Chem. Soc.* **126**, 5950–5951 (2004).
3. A. El-Hawiet, *et al.*, Quantifying Ligand Binding to Large Protein Complexes Using Electrospray Ionization Mass Spectrometry. *Anal. Chem.* **84**, 3867–3870 (2012).

4. F. Sobott, J. L. P. Benesch, E. Vierling, C. V. Robinson, Subunit Exchange of Multimeric Protein Complexes REAL-TIME MONITORING OF SUBUNIT EXCHANGE BETWEEN SMALL HEAT SHOCK PROTEINS BY USING ELECTROSPRAY MASS SPECTROMETRY. *J. Biol. Chem.* **277**, 38921–38929 (2002).
5. S. J. Allen, A. M. Schwartz, M. F. Bush, Effects of Polarity on the Structures and Charge States of Native-Like Proteins and Protein Complexes in the Gas Phase. *Anal. Chem.* **85**, 12055–12061 (2013).
6. A. J. R. Heck, R. H. H. van den Heuvel, Investigation of intact protein complexes by mass spectrometry. *Mass Spectrom. Rev.* **23**, 368–389 (2004).
7. C. J. Hogan, J. A. Carroll, H. W. Rohrs, P. Biswas, M. L. Gross, Combined Charged Residue-Field Emission Model of Macromolecular Electrospray Ionization. *Anal. Chem.* **81**, 369–377 (2009).
8. H. J. Sterling, *et al.*, Effects of Supercharging Reagents on Noncovalent Complex Structure in Electrospray Ionization from Aqueous Solutions. *J. Am. Soc. Mass Spectrom.* **21**, 1762–1774 (2010).
9. J. C. May, *et al.*, Conformational Landscapes of Ubiquitin, Cytochrome c, and Myoglobin: Uniform Field Ion Mobility Measurements in Helium and Nitrogen Drift Gas. *Int. J. Mass Spectrom.* **427**, 79–90 (2018).
10. A. Q. Stiving, B. J. Jones, J. Ujma, K. Giles, V. H. Wysocki, Collision Cross Sections of Charge-Reduced Proteins and Protein Complexes: A Database for Collision Cross Section Calibration. *Anal. Chem.* **92**, 4475–4483 (2020).
11. S. Hong, M. F. Bush, Collision-Induced Unfolding Is Sensitive to the Polarity of Proteins and Protein Complexes. *J. Am. Soc. Mass Spectrom.* **30**, 2430–2437 (2019).
12. K. Pagel, S.-J. Hyung, B. T. Ruotolo, C. V. Robinson, Alternate Dissociation Pathways Identified in Charge-Reduced Protein Complex Ions. *Anal. Chem.* **82**, 5363–5372 (2010).
13. Y. Tian, B. T. Ruotolo, Collision induced unfolding detects subtle differences in intact antibody glycoforms and associated fragments. *Int. J. Mass Spectrom.* **425**, 1–9 (2018).
14. T. Botzanowski, *et al.*, Insights from native mass spectrometry approaches for top- and middle- level characterization of site-specific antibody-drug conjugates. *mAbs* **9**, 801–811 (2017).
15. S. M. Fantin, *et al.*, Collision Induced Unfolding Classifies Ligands Bound to the Integral Membrane Translocator Protein. *Anal. Chem.* **91**, 15469–15476 (2019).
16. J. T. S. Hopper, N. J. Oldham, Collision induced unfolding of protein ions in the gas phase studied by ion mobility-mass spectrometry: The effect of ligand binding on conformational stability. *J. Am. Soc. Mass Spectrom.* **20**, 1851–1858 (2009).
17. Y. Zhong, L. Han, B. T. Ruotolo, Collisional and Coulombic unfolding of gas-phase proteins: high correlation to their domain structures in solution. *Angew. Chem. Int. Ed Engl.* **53**, 9209–9212 (2014).
18. Y. Tian, L. Han, A. C. Buckner, B. T. Ruotolo, Collision Induced Unfolding of Intact Antibodies: Rapid Characterization of Disulfide Bonding Patterns, Glycosylation, and Structures. *Anal. Chem.* **87**, 11509–11515 (2015).
19. O. Hernandez-Alba, E. Wagner-Rousset, A. Beck, S. Cianférani, Native Mass Spectrometry, Ion Mobility, and Collision-Induced Unfolding for Conformational Characterization of IgG4 Monoclonal Antibodies. *Anal. Chem.* **90**, 8865–8872 (2018).
20. A. M. Scott, J. D. Wolchok, L. J. Old, Antibody therapy of cancer. *Nat. Rev. Cancer* **12**, 278–287 (2012).

21. T. Dörner, A. Radbruch, G. R. Burmester, B-cell-directed therapies for autoimmune disease. *Nat. Rev. Rheumatol.* **5**, 433–441 (2009).
22. I. Melnikova, Therapies for Alzheimer's disease. *Nat. Rev. Drug Discov.* **6**, 341–342 (2007).
23. C. Saylor, E. Dadachova, A. Casadevall, Monoclonal antibody-based therapies for microbial diseases. *Vaccine* **27**, G38–G46 (2009).
24. T. Mizuochi, T. Taniguchi, A. Shimizu, A. Kobata, Structural and numerical variations of the carbohydrate moiety of immunoglobulin G. *J. Immunol. Baltim. Md 1950* **129**, 2016–2020 (1982).
25. H. Leibiger, D. Wüstner, R. D. Stigler, U. Marx, Variable domain-linked oligosaccharides of a human monoclonal IgG: structure and influence on antigen binding. *Biochem. J.* **338**, 529–538 (1999).
26. L. W. Dick, C. Kim, D. Qiu, K.-C. Cheng, Determination of the origin of the N-terminal pyro-glutamate variation in monoclonal antibodies using model peptides. *Biotechnol. Bioeng.* **97**, 544–553 (2007).
27. M. Perkins, R. Theiler, S. Lunte, M. Jeschke, Determination of the origin of charge heterogeneity in a murine monoclonal antibody. *Pharm. Res.* **17**, 1110–1117 (2000).
28. B. Hintersteiner, *et al.*, Microheterogeneity of therapeutic monoclonal antibodies is governed by changes in the surface charge of the protein. *Biotechnol. J.* **11**, 1617–1627 (2016).
29. R. J. Harris, Heterogeneity of recombinant antibodies: linking structure to function. *Dev. Biol.* **122**, 117–127 (2005).
30. Y. Mimura, *et al.*, The influence of glycosylation on the thermal stability and effector function expression of human IgG1-Fc: properties of a series of truncated glycoforms. *Mol. Immunol.* **37**, 697–706 (2000).
31. K. Zheng, C. Bantog, R. Bayer, The impact of glycosylation on monoclonal antibody conformation and stability. *mAbs* **3**, 568–576 (2011).
32. L. J. Harris, E. Skaletsky, A. McPherson, Crystallographic structure of an intact IgG1 monoclonal antibody11Edited by I. A. Wilson. *J. Mol. Biol.* **275**, 861–872 (1998).
33. E. O. Saphire, *et al.*, Crystal Structure of a Neutralizing Human IgG Against HIV-1: A Template for Vaccine Design. *Science* **293**, 1155–1159 (2001).
34. L. J. Harris, S. B. Larson, K. W. Hasel, A. McPherson, Refined structure of an intact IgG2a monoclonal antibody. *Biochemistry* **36**, 1581–1597 (1997).
35. S. Horita, *et al.*, High-resolution crystal structure of the therapeutic antibody pembrolizumab bound to the human PD-1. *Sci. Rep.* **6**, 1–8 (2016).
36. F. Long, *et al.*, Structural basis of a potent human monoclonal antibody against Zika virus targeting a quaternary epitope. *Proc. Natl. Acad. Sci.* **116**, 1591–1596 (2019).
37. F. Long, *et al.*, Cryo-EM structures elucidate neutralizing mechanisms of anti-chikungunya human monoclonal antibodies with therapeutic activity. *Proc. Natl. Acad. Sci.* **112**, 13898–13903 (2015).
38. I. D. G. Campuzano, C. Larriba, D. Bagal, P. D. Schnier, "Ion Mobility and Mass Spectrometry Measurements of the Humanized IgGk NIST Monoclonal Antibody" in *State-of-the-Art and Emerging Technologies for Therapeutic Monoclonal Antibody Characterization Volume 3. Defining the Next Generation of Analytical and Biophysical Techniques*, ACS Symposium Series., (American Chemical Society, 2015), pp. 75–112.

39. K. J. Pacholarz, *et al.*, Dynamics of Intact Immunoglobulin G Explored by Drift-Tube Ion-Mobility Mass Spectrometry and Molecular Modeling. *Angew. Chem. Int. Ed.* **53**, 7765–7769 (2014).
40. K. Giles, J. P. Williams, I. Campuzano, Enhancements in travelling wave ion mobility resolution. *Rapid Commun. Mass Spectrom. RCM* **25**, 1559–1566 (2011).
41. S. J. Allen, K. Giles, T. Gilbert, M. F. Bush, Ion mobility mass spectrometry of peptide, protein, and protein complex ions using a radio-frequency confining drift cell. *Analyst* **141**, 884–891 (2016).
42. J. P. Williams, J. M. Brown, I. Campuzano, P. J. Sadler, Identifying drug metallation sites on peptides using electron transfer dissociation (ETD), collision induced dissociation (CID) and ion mobility-mass spectrometry (IM-MS). *Chem. Commun. Camb. Engl.* **46**, 5458–5460 (2010).
43. S. A. McLuckey, J. L. Stephenson, Ion/ion chemistry of high-mass multiply charged ions. *Mass Spectrom. Rev.* **17**, 369–407 (1998).
44. K. J. Laszlo, J. H. Buckner, E. B. Munger, M. F. Bush, Native-like and Denatured Cytochrome c Ions Yield Cation-to-Anion Proton-Transfer Reaction Products with Similar Collision Cross Sections. *J. Am. Soc. Mass Spectrom.* **28**, 1382–1391 (2017).
45. M. F. Bush, I. D. G. Campuzano, C. V. Robinson, Ion mobility mass spectrometry of peptide ions: effects of drift gas and calibration strategies. *Anal. Chem.* **84**, 7124–7130 (2012).
46. A. R. McKay, B. T. Ruotolo, L. L. Ilag, C. V. Robinson, Mass Measurements of Increased Accuracy Resolve Heterogeneous Populations of Intact Ribosomes. *J. Am. Chem. Soc.* **128**, 11433–11442 (2006).
47. P. Lössl, J. Snijder, A. J. R. Heck, Boundaries of Mass Resolution in Native Mass Spectrometry. *J. Am. Soc. Mass Spectrom.* **25**, 906–917 (2014).
48. K. J. Laszlo, M. F. Bush, Analysis of Native-Like Proteins and Protein Complexes Using Cation to Anion Proton Transfer Reactions (CAPTR). *J. Am. Soc. Mass Spectrom.* **26**, 2152–2161 (2015).
49. Z. Hall, A. Politis, M. F. Bush, L. J. Smith, C. V. Robinson, Charge-State Dependent Compaction and Dissociation of Protein Complexes: Insights from Ion Mobility and Molecular Dynamics. *J. Am. Chem. Soc.* **134**, 3429–3438 (2012).
50. J. Freeke, M. F. Bush, C. V. Robinson, B. T. Ruotolo, Gas-phase protein assemblies: Unfolding landscapes and preserving native-like structures using noncovalent adducts. *Chem. Phys. Lett.* **524**, 1–9 (2012).

Chapter 5: CIU Analysis of Protein-Ligand Complexes of Interest in the Presence of Nonspecifically Binding Interference

5.1 Abstract

Collision-induced unfolding (CIU) is increasingly used to study the effects of ligand binding to proteins and protein complexes. During CIU, precursor ions with a wide window of *m*/*z* are usually isolated; the width of this window is associated with the broad features often observed in native MS and in order to maximize sensitivity. Here, the mass spectra with increasing collision-energy show that the quadrupole selected precursor ions are interfered by nonspecifically binding adducts (NSA). Therefore, $S_{relative}$ is developed to evaluate the abundance of the interferants in the *m*/*z* windows of the precursor ions as a function of energy. The $S_{relative}$ method is used to determine the minimum collision-energy threshold at which all of the apparent NSA are removed. This energy threshold is used to unambiguously interpret the effects of ligand binding of interest on the CIU and CID stability. More generally, the $S_{relative}$ method may be used for quality control of CIU analysis.

5.2 Introduction

Ions in native MS are formed from ESI (electrospray ionization) (1, 2). Native MS experiments are operated under nondenaturing conditions including low temperature, low pressure, and minimal potential difference in the instrument. The ions of native MS display characteristics that are correlated to noncovalent interactions in the aqueous solution such as stoichiometry (3, 4), heterogeneity (3, 4), dynamics (3) and ligand binding (5) of proteins and protein complexes. Native MS analysis is increasingly used to study protein-ligand interactions (6–9) and provides insights into direct binding information (6, 8, 10). For example, native MS

results of the biotin retention protein A (BirA) from *Staphylococcus aureus* shows that the dimeric protein makes a complex with an oligonucleotide that has the a biotin transporter (BioY) recognition sequence under high biotin conditions (11).

Ion mobility (IM) separates ions based on their mobility and provides information about the size and shape of the analyte in terms of collision cross section (Ω). IM-MS results correlate the mobility of the ions with the respective results from MS. Energy-dependent IM-MS techniques such as collision-induced unfolding (CIU) (12–15) or collision induced dissociation (CID) (13, 14) provide further insights into the stability of protein complexes. Collisional activation of protein complexes unfolds the proteins by increasing the internal energy prior to IM-MS analysis. The CIU of protein complexes is mediated by migration of mobile protons (16, 17) to one of the subunits, which causes the Coulombic unfolding and the subsequent ejection of the subunit at sufficiently high energy.

Previously, several studies have established that CIU is sensitive to ligand binding (18–20). The application of CIU of the native precursor is often performed without narrow isolation of the ion of interest (*i.e.*, CIU of the whole spectrum) (21). Therefore, the effects of ligand binding of interest may be convoluted by the interference of nonspecific adducts (NSA). For instance, the binding of NSA including nonvolatile buffer ions (22) and alkali or alkali earth metal ions (15, 23) can increase the CIU stability of proteins in the gas-phase. The presence of NSA detected by MS are attributed to sample preparation (*e.g.*, incomplete buffer exchange), ionization conditions (*e.g.*, droplet size (24) formed from ESI, heating) and/or inevitable exposure to surface.

HSPB5 alpha crystallin domain (ACD) is the core domain of the full-length HSPB5, a mammalian small heat shock protein. HSPB5 ACD exists in equilibrium between monomers and

dimers in solution (25). A previous work suggests that the function of the full-length HSPB5 may be modulated by the dimer and monomer equilibrium of the ACD. Various metal ion binding to the full-length HSPB5 may increase or decrease the chaperone activity of the full-length HSPB5 (26). Here, we aim to study the effects of Ni(II) binding to the HSPB5 ACD dimer on the CIU and CID stability. The initial precursor for CIU analysis is interfered by NSA, precluding direct assessment of the effects of ligand binding. Increasing energy releases NSA from the quadrupole selected peak and gives rise to additional signals of the ACD dimer at lower *m*/*z* than the initially quadrupole selected peak. By probing the intensity in the initially quadrupole selected m/z relative to all observed dimer signals as a function of energy, we determine the minimum energy where the apparent NSA are fully released from the quadrupole selected peak. This energy threshold is used to unambiguously investigate the effects of ligand binding of interest on the CIU stability.

5.3 Experimental Methods

Sample Preparation

A TEV cleavable N-terminally His-tagged ACD of HSBP5 (residues 64–152 of the full-length HSPB5, UNIPROT: P02511) was expressed (27) and purified (28) as reported previously. The ACD was buffer exchanged into 200 mM ammonium acetate at pH 8.5 using centrifugal concentrators (5 kDa MWCO, Spin-X UF, Corning, Inc.). The final solution containing 10 μM ACD of HSBP5 titrated with 30 μM $NiCl_2 \cdot 6H2O$ (Sigma Aldrich) solutions were incubated for 20 to 24 hours at room temperature.

Native MS and IM-MS

Ions were generated using nESI as described previously (29). Mass spectrometry data were acquired using a Waters Synapt G2 HDMS instrument in which the traveling-wave ion mobility cell was replaced with a radio-frequency (rf) confining drift cell (30). The following MS parameters were used: capillary voltage, equal or less than 1.0 kV; sampling cone, 20 V; extraction cone, 5 V; source temperature, ~ 30 ºC; trap collision energy, 4 for the native MS. Mass spectra were analyzed using MassLynx (v4.1, Waters Co.). To determine the mobilities of minimally activated protein ions, ions were introduced into the rf confining drift cell that was operated using drift voltages ranging from 104 to 354 V (30). Ω values of protein ions and the mobility-independent transport times of ions (t0) were determined from the slopes of plots of drift time versus reciprocal drift voltage as described previously (30). For CIU experiments, ions were accelerated prior to entering the trap cell using trap injection voltages ranging from 4 to 61 V with 1 V increments using the rf confining drift cell operated at a drift voltage of 104 V. For all IM experiments, rf confining drift cell contained ~1.7 torr He. The arrival time distributions were extracted and analyzed using in-house software (31).

5.4 Results

5.4.1 Precursor Ions

Figure 5.1a shows the native spectrum of the 9+ dimer of HSPB5 ($[2ACD+2Ni+5H]^{9+}$). The signals at higher *m*/z than the quadrupole selected Ω precursor indicates the presence of NSA. The mass difference in the resolved peaks indicates that Na (23.0 Da) may nonspecifically bind to the ACD dimer. However, the unresolved baseline indicates that additional types of NSA are present. The presence of NSA may be attributed to the insufficient removal of buffer that the protein was prepared prior to buffer exchange into ammonium acetate. Additionally, the presence of NSA may be attributed to the inevitable exposure to surfaces (*e.g.*, glass capillary). Since the

apo ACD displays the presence of NSA (Figure 5.1a), it is likely that the NSA are present in Figure 5.1b, which shows HSPB5 with Ni(II) titration.

Figure 5.1a and 5.1b show the quadrupole selection of precursor ions for CIU based on *m*/*z*. Figure 5.1a shows that the quadrupole selection of the precursor of apo 9+ dimer HSPB5 does not likely have any contributions from NSA. However, quadrupole selection of the $[2ACD+2Ni+5H]^{9+}$ based on *m*/*z* is likely interfered by NSA. For example, the quadrupole selected peak may include $[2ACD+NSA]^{9+}$and/or $[2ACD+1Ni+NSA]^{9+}$ in addition to $[2ACD+2Ni+5H]^{9+}$. The three species may be more resolved with instruments with higher mass resolving power.

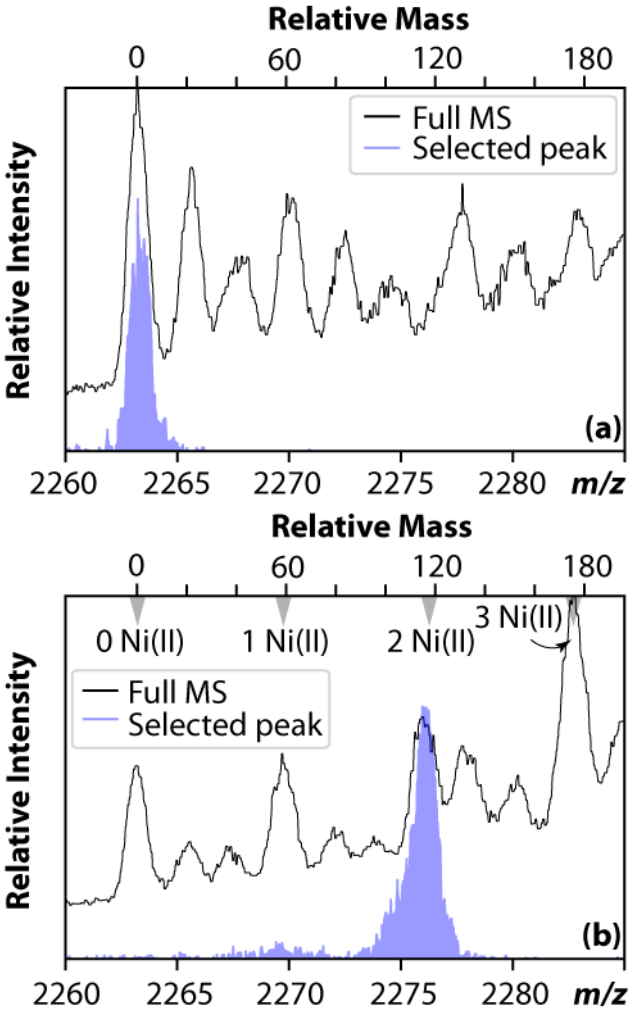

Figure 5.1. The enlarged native mass spectrum of 9+ HSPB5 dimer (a) without the addition of Ni(II) and (b) with the addition of Ni (II) (noted with black solid trace). The shaded region indicate the quadrupole selected (a) apo and (b) 2 Ni(II) bound 9+ HSPB5 dimer based on *m*/*z*. Relative mass axis indicates zero relative to the non-adducted 9+ HSPB5 dimer. (b) The arrows indicate the relative mass of 0 to 3 Ni(II) ions bound HSPB5 ACD.

5.4.2 Determination of $S_{relative}$

Figure 5.2a shows the effects of collisional activation on the apparent $[2ACD+2Ni+5H]^{9+}$ ions; the corresponding mass spectra with and without quadrupole selection are shown in Figure 5.1b. Interestingly, the activation of those ions gives rise to two additional peaks that align with $[2ACD+Ni+7H]^{9+}$ and $[2ACD+9H]^{9+}$. On the contrary, activation of the quadrupole selected ions shown in Figure 5.1a did not give rise to additional peaks at lower *m*/*z* corresponding to other types of ACD dimer (data not shown). This indicates that the emergence of additional peaks in Figure 5.1b can be attributed to the loss of noncovalent interactions but not covalent bond breaking.

The mass difference between the initial peak ($[2ACD+2Ni+5H]^{9+}$) and the additional peaks ($[2ACD+Ni+7H]^{9+}$ and $[2ACD+9H]^{9+}$) are approximately multiples of 58.69 Da. Additionally, the release of adducts does not alter the charge state, inferring that the adducts are lost as neutral molecules. One of the candidates that satisfy these two conditions is acetic acid (60.05 Da). Acetic acid may be formed from a proton from the proteins and acetate from ammonium acetate.

Figure 5.2b shows the survival of the precursor ions as a function of laboratory frame energy. Laboratory frame energy is the product of the charge state and trap injection voltage. The survival yield will be quantified by *S*, where *S* is defined using Equation 1:

$$S = \frac{\sum_{m/z=2275}^{m/z=2278} Intensity(m/z)}{\sum_{m/z=2260}^{m/z=2278} Intensity(m/z)} \qquad \text{Equation (1)}$$

S is used to determine the energy threshold that the signal from *m*/*z* 2275 to 2278 unambiguously probes HSPB5 bound by two Ni(II). *S* value decreases as the laboratory frame energy increases. The decrease of *S* indicates that signal from NSA decreases from the *m*/*z* of the initially quadrupole selected peak. The extent of decrease of *S* varies by the replicate. This indicates that

each replicate contains varying amount of NSA. Therefore, the normalized *S* ($S_{relative}$) is required to determine the energy threshold (*vide infra*). The increase of *S* at high energy occurs as the dimeric HSPB5 dissociates to monomers in the order of the $[2ACD+9H]^{9+}$, $[2ACD+1Ni+7H]^{9+}$ and $[2ACD+2Ni+5H]^{9+}$.

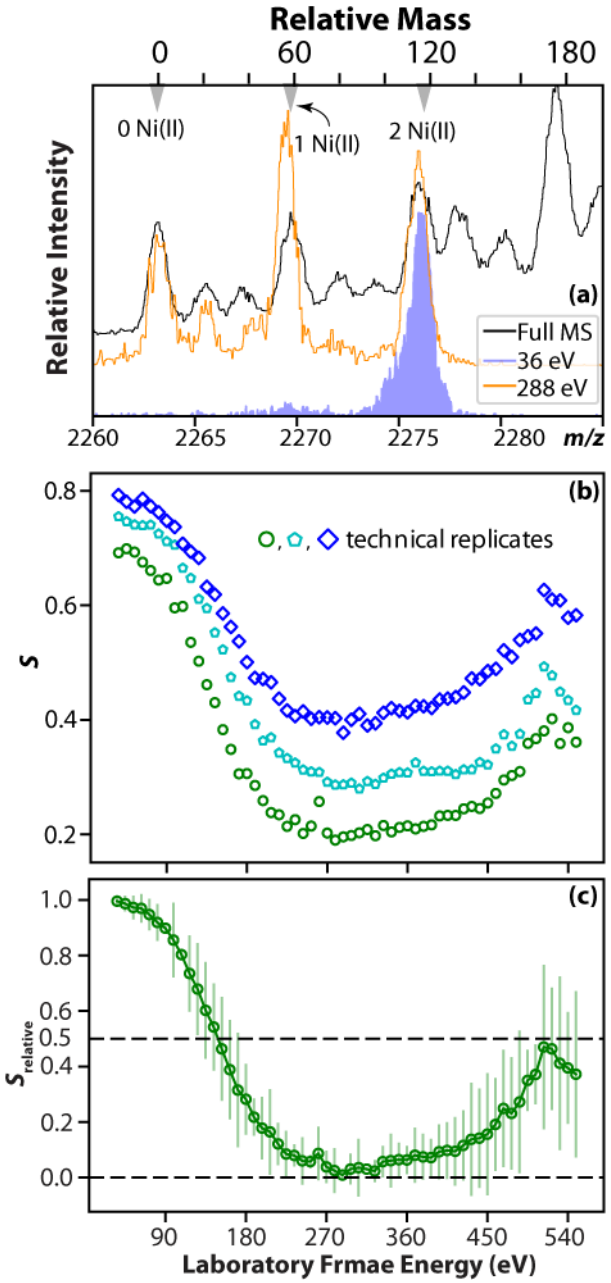

Figure 5.2. The enlarged mass spectrum of 9+ HSPB5 dimer (a) with the addition of Ni(II) (black solid trace). The quadrupole selected (a) 2 Ni(II) bound 9+ HSPB5 dimer based on *m*/*z* at 36 (shaded) and 288 eV (orange trace). (b) *S* as a function of laboratory frame energy. (c) The average of the $S_{relative}$ of the three independent replicates is plotted as a function of laboratory

frame energy. The error bar indicates the 95% confidence interval of the three independent technical replicates.

The $S_{relative}$ is defined as the following (Equation 2):

$$S_{relative} = \frac{S - S_{\min}}{S_{\max} - S_{\min}} \quad \text{Equation (2)}$$

where S_{min} the minimum value of S and S_{max} the maximum value of S. The $S_{relative}$ of each replicate reaches zero (S_{min}) at 288 eV for all replicates. This indicates that NSA are fully released at 288 eV for all technical replicates despite the varying amounts of adducts.

Figure 5.3a and 5.3b show the CIU heat maps of $[2ACD+2Ni+5H]^{9+}$and $[2ACD+9H]^{9+}$ respectively. The CIU of the most compact conformations (198 eV) is destabilized by two Ni(II) binding compared to the apo. On the contrary, the CIU of the intermediate conformations (333 eV) is stabilized by two Ni(II) relative to the apo. Since the apparent adduct interference is no longer present at energy higher than 288 eV, the increased CIU stability of the intermediate conformations is unambiguously attributed to two Ni(II) binding to HSPB5.

5.4.3 CIU and CID Analysis: Effects of Ni(II) Binding to the ACD Dimer

Figure 5.3a and 5.3b show the CIU heat maps of $[2ACD+2Ni+5H]^{9+}$and $[2ACD+9H]^{9+}$ respectively. Three major CIU species are observed for both $[2ACD+2Ni+5H]^{9+}$and $[2ACD+9H]^{9+}$ based on the **Ω** distribution: compact (I), partially unfolded (II) and mostly unfolded (III) species. The **Ω** distributions of conformer II show bimodal and unimodal distributions for $[2ACD+2Ni+5H]^{9+}$ and $[2ACD+9H]^{9+}$ respectively. The median **Ω** values of $[2ACD+2Ni+5H]^{9+}$ and $[2ACD+9H]^{9+}$ at 270 eV are determined from 50% of the cumulative distribution function of the **Ω** distribution (32). The median **Ω** values show 2% difference. Therefore, both **Ω** distributions are classified as conformer II for further analysis. The relative abundance of CIU conformers are plotted in Figure 5.3c and 5.3d as a function of energy. The

transition midpoint energy (TME) indicates the energy for the appearance and disappearance of CIU conformers by 50% and is used to evaluate the CIU unfolding stability of an ion.

The transition from conformer I to conformer II occurs at a lower energy than the threshold energy (288 eV) identified in the preceding section. On the contrary, the transition from conformer II to conformer III occurs above the threshold. Therefore, the unfolding from conformer II to conformer III is used to compare the CIU stability of $[2ACD+2Ni+5H]^{9+}$ and the apo counterpart. The TME for the transition from conformer II to conformer III of the $[2ACD+9H]^{9+}$ and $[2ACD+2Ni+5H]^{9+}$ are 297 – 306 and 333 eV respectively. This suggests that two Ni(II) binding stabilizes the unfolding from conformer II to conformer III by 27 – 36 eV. One explanation for the observed increase in unfolding stability involves the type of charge carrier of the apo and Ni(II) bound protein. The CIU of $[2ACD+9H]^{9+}$ is mediated by migration of mobile protons. In comparison, the charge carrier of $[2ACD+2Ni+5H]^{9+}$ may be a combination of protons and Ni(II) that the complex may display less efficient CIU due to less mobility of Ni(II) via multidentate interactions compared to protons.

Increasing energy eventually leads to CID of the apo and Ni(II) bound precursor dimers mostly via asymmetric charge partitioning generating 6+ and 3+ monomers (Figure S5.1a). However, some symmetric dissociation is evidenced by 5+ and 4+ monomers (Figure S5.1a). The CID of precursors containing Ni(II) generates product ions that retain Ni(II) even after the dissociations of the dimers, suggesting the high stability of Ni(II) binding interactions with the ACD dimer. To understand the effects of Ni(II) binding on the CID stability, the CID survival yield of precursor dimers relative to the dimers and dissociated monomers is probed as a function of the energy (Figure 5.3c and 5.3d) using the relative intensity in the mass spectra. Note that the precursor dimers in Figure 5.3d include all the dimers generated from the initially quadrupole

selected peak ($[2ACD+2Ni+5H]^{9+}$, $[2ACD+1Ni+7H]^{9+}$ and $[2ACD+9H]^{9+}$). Therefore, the difference between the CID stability in Figure 5.3c and 5.3d is attributed to one Ni(II) and/or two Ni(II) binding relative to the apo. The CID survival yield of the apo precursor dimer shows that the survival yield drastically decreases with the appearance of conformer III, indicating that the unfolding from conformer II to III significantly contributes to the dissociation. The TME of the apo and Ni(II) containing precursors are 432 – 441 and ~ 459 eV respectively, suggesting that Ni(II) binding increases the CID stability by 18 – 27 eV. Since the unfolding from conformer II to conformer III is above the 288 eV threshold, it may be possible that the increased stability of CID may be attributed to the increased CIU stability of $[2ACD+2Ni+5H]^{9+}$ compared to the apo.

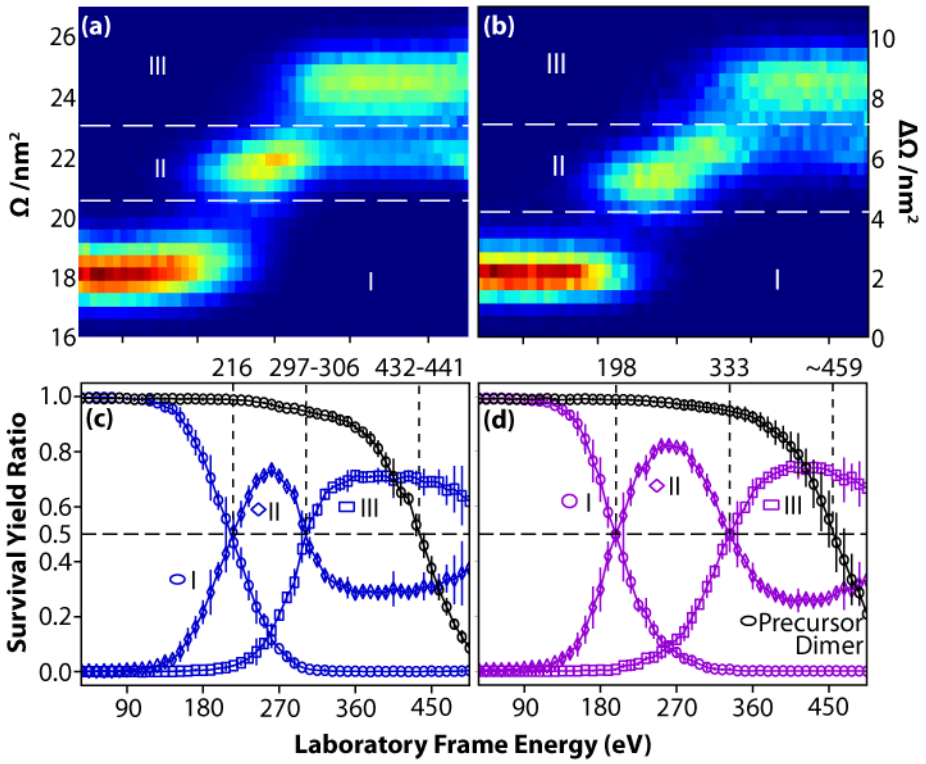

Figure 5.3. the CIU results of (a) the unadducted (Figure 5.1a) and (b) the quadrupole selected peak (Figure 5.1b). The trap injection voltage ranges from 4 – 61 V by 1 V increment. The survival yield plot of the CIU conformers of the precursors in (c) Figure 5.1a and (d) Figure 5.1b are probed as a function of energy. The CID survival yield of the precursor dimers relative to dissociated monomers (black trace) is plotted as a function of energy for the initial precursor dimers shown in (c) Figure 5.1a and (d) Figure 5.1b.

5.5 Conclusion

The objective of this research was to study Ni(II) binding to the 9+ HSPB5 ACD dimer using CIU and CID. Despite extensive buffer exchange, it was challenging to generate native MS spectra without the presence of NSA (Figure 5.1). As a result, the quadrupole selected precursor ions for CIU analysis of protein-ligand are interfered by NSA. In order to circumvent the adduct interference, $S_{relative}$ is used to determine the minimum collision-energy threshold at which all of the adduct ions are released (Figure 5.2). Using the threshold, we unambiguously determined the effects of two Ni(II) binding on the CIU stability of HSPB5 ACD dimers in comparison to the apo dimer. Ni(II) binding increases the stability of CIU from conformer II to III, which consequently increases the CID stability of the dimer (Figure 5.3). The $S_{relative}$ method is useful to understand the effects of ligand binding on the CIU and CID stability of protein-ligand complexes. Furthermore, The $S_{relative}$ method may be used for a general quality control for CIU analysis of protein ions that may be interfered by nonspecifically binding adducts.

5.6 Acknowledgement

This work is supported by the National Eye Institute under 2R01EY017370-09 (M. F. B.). M.F.B. and SH. acknowledge support from the University of Washington. The authors thank Prof. Rachel Klevit for providing the HSPB5 ACD samples and critical insights.

5.7 Supporting Information

Figures S5.1.

5.8 References

1. J. B. Fenn, M. Mann, C. K. Meng, S. F. Wong, C. M. Whitehouse, Electrospray ionization for mass spectrometry of large biomolecules. *Science* **246**, 64–71 (1989).
2. M. Wilm, M. Mann, Analytical properties of the nanoelectrospray ion source. *Anal. Chem.* **68**, 1–8 (1996).

3. I. Ebong, *et al.*, Heterogeneity and dynamics in the assembly of the Heat Shock Protein 90 chaperone complexes. *PNAS* **108**, 17939–17944 (2011).
4. J. Z. Bereszczak, *et al.*, Structure, stability and dynamics of norovirus P domain derived protein complexes studied by native mass spectrometry. *Journal of Structural Biology* **177**, 273–282 (2012).
5. R. J. Rose, *et al.*, Quantitative analysis of the interaction strength and dynamics of human IgG4 half molecules by native mass spectrometry. *Structure* **19**, 1274–1282 (2011).
6. A. El-Hawiet, *et al.*, Quantifying Ligand Binding to Large Protein Complexes Using Electrospray Ionization Mass Spectrometry. *Anal. Chem.* **84**, 3867–3870 (2012).
7. M. A. Freitas, C. L. Hendrickson, A. G. Marshall, A. A. Rostom, C. V. Robinson, Competitive binding to the oligopeptide binding protein, OppA: in-trap cleanup in an fourier transform ion cyclotron resonance mass spectrometer. *Journal of the American Society for Mass Spectrometry* **11**, 1023–1026 (2000).
8. A. El-Hawiet, E. N. Kitova, J. S. Klassen, Quantifying Protein Interactions with Isomeric Carbohydrate Ligands Using a Catch and Release Electrospray Ionization-Mass Spectrometry Assay. *Anal. Chem.* **85**, 7637–7644 (2013).
9. H.-Y. Yen, *et al.*, Ligand binding to a G protein–coupled receptor captured in a mass spectrometer. *Science Advances* **3**, e1701016 (2017).
10. P. I. Kitov, *et al.*, A quantitative, high-throughput method identifies protein–glycan interactions via mass spectrometry. *Communications Biology* **2**, 1–7 (2019).
11. J. Satiaputra, *et al.*, Native mass spectrometry identifies an alternative DNA-binding pathway for BirA from Staphylococcus aureus. *Scientific Reports* **9**, 2767 (2019).
12. J. L. P. Benesch, B. T. Ruotolo, D. A. Simmons, C. V. Robinson, Protein Complexes in the Gas Phase: Technology for Structural Genomics and Proteomics. *Chem. Rev.* **107**, 3544–3567 (2007).
13. K. J. Light-Wahl, B. L. Schwartz, R. D. Smith, Observation of the Noncovalent Quaternary Associations of Proteins by Electrospray Ionization Mass Spectrometry. *J. Am. Chem. Soc.* **116**, 5271–5278 (1994).
14. J. C. Jurchen, E. R. Williams, Origin of Asymmetric Charge Partitioning in the Dissociation of Gas-Phase Protein Homodimers. *J. Am. Chem. Soc.* **125**, 2817–2826 (2003).
15. L. Han, S.-J. Hyung, B. T. Ruotolo, Bound Cations Significantly Stabilize the Structure of Multiprotein Complexes in the Gas Phase. *Angewandte Chemie International Edition* **51**, 5692–5695 (2012).
16. V. Popa, D. A. Trecroce, R. G. McAllister, L. Konermann, Collision-Induced Dissociation of Electrosprayed Protein Complexes: An All-Atom Molecular Dynamics Model with Mobile Protons. *J. Phys. Chem. B* **120**, 5114–5124 (2016).
17. S. K. Fegan, M. Thachuk, A Charge Moving Algorithm for Molecular Dynamics Simulations of Gas-Phase Proteins. *J. Chem. Theory Comput.* **9**, 2531–2539 (2013).
18. J. T. S. Hopper, N. J. Oldham, Collision induced unfolding of protein ions in the gas phase studied by ion mobility-mass spectrometry: the effect of ligand binding on conformational stability. *J. Am. Soc. Mass Spectrom.* **20**, 1851–1858 (2009).
19. Y. Huang, N. D. Salinas, E. Chen, N. H. Tolia, M. L. Gross, Native Mass Spectrometry, Ion mobility, and Collision-Induced Unfolding Categorize Malaria Antigen/Antibody Binding. *J. Am. Soc. Mass Spectrom.* **28**, 2515–2518 (2017).
20. M. Landreh, *et al.*, Integrating mass spectrometry with MD simulations reveals the role of lipids in Na + /H + antiporters. *Nature Communications* **8**, 13993 (2017).

21. D. D. Vallejo, *et al.*, A Modified Drift Tube Ion Mobility-Mass Spectrometer for Charge-Multiplexed Collision-Induced Unfolding. *Anal. Chem.* **91**, 8137–8146 (2019).
22. J. Freeke, M. F. Bush, C. V. Robinson, B. T. Ruotolo, Gas-phase protein assemblies: Unfolding landscapes and preserving native-like structures using noncovalent adducts. *Chemical Physics Letters* **524**, 1–9 (2012).
23. L. Han, S.-J. Hyung, J. J. S. Mayers, B. T. Ruotolo, Bound Anions Differentially Stabilize Multiprotein Complexes in the Absence of Bulk Solvent. *J. Am. Chem. Soc.* **133**, 11358–11367 (2011).
24. K. L. Davidson, D. R. Oberreit, C. J. Hogan, M. F. Bush, Nonspecific aggregation in native electrokinetic nanoelectrospray ionization. *International Journal of Mass Spectrometry* **420**, 35–42 (2017).
25. P. Rajagopal, *et al.*, A conserved histidine modulates HSPB5 structure to trigger chaperone activity in response to stress-related acidosis. *eLife* **4**, e07304 (2015).
26. A. Biswas, K. P. Das, Zn2+ Enhances the Molecular Chaperone Function and Stability of α-Crystallin. *Biochemistry* **47**, 804–816 (2008).
27. S. P. Delbecq, S. Jehle, R. Klevit, Binding determinants of the small heat shock protein, αB-crystallin: recognition of the "IxI" motif. *EMBO J.* **31**, 4587–4594 (2012).
28. S. Jehle, *et al.*, αB-Crystallin: A Hybrid Solid-Solution State NMR Investigation Reveals Structural Aspects of the Heterogeneous Oligomer. *J Mol Biol* **385**, 1481–1497 (2009).
29. S. Hong, M. F. Bush, Collision-Induced Unfolding Is Sensitive to the Polarity of Proteins and Protein Complexes. *Journal of The American Society for Mass Spectrometry* (2019) https:/doi.org/10.1021/jasms.8b06263 (June 12, 2020).
30. S. J. Allen, K. Giles, T. Gilbert, M. F. Bush, Ion mobility mass spectrometry of peptide, protein, and protein complex ions using a radio-frequency confining drift cell. *Analyst* **141**, 884–891 (2016).
31. M. F. Bush, I. D. G. Campuzano, C. V. Robinson, Ion mobility mass spectrometry of peptide ions: effects of drift gas and calibration strategies. *Anal. Chem.* **84**, 7124–7130 (2012).
32. K. J. Laszlo, J. H. Buckner, E. B. Munger, M. F. Bush, Native-Like and Denatured Cytochrome c Ions Yield Cation-to-Anion Proton Transfer Reaction Products with Similar Collision Cross-Sections. *J. Am. Soc. Mass Spectrom.* **28**, 1382–1391 (2017).

Appendix A

Supplemental Information for Chapter 3

Table S1. Median Ω Values.

		Cations	Anions
Protein Name	**|z|**	**Ω / nm²**	**Ω / nm²**
Avidin	13	-	35.3
	14	35.2	35.3
	15	35.6	-
	16	35.9	-
β-lactoglobulin (*monomer*)	6	-	16.1
	7	16.7	16.4
	8	17.2	-
	9	18.0	-

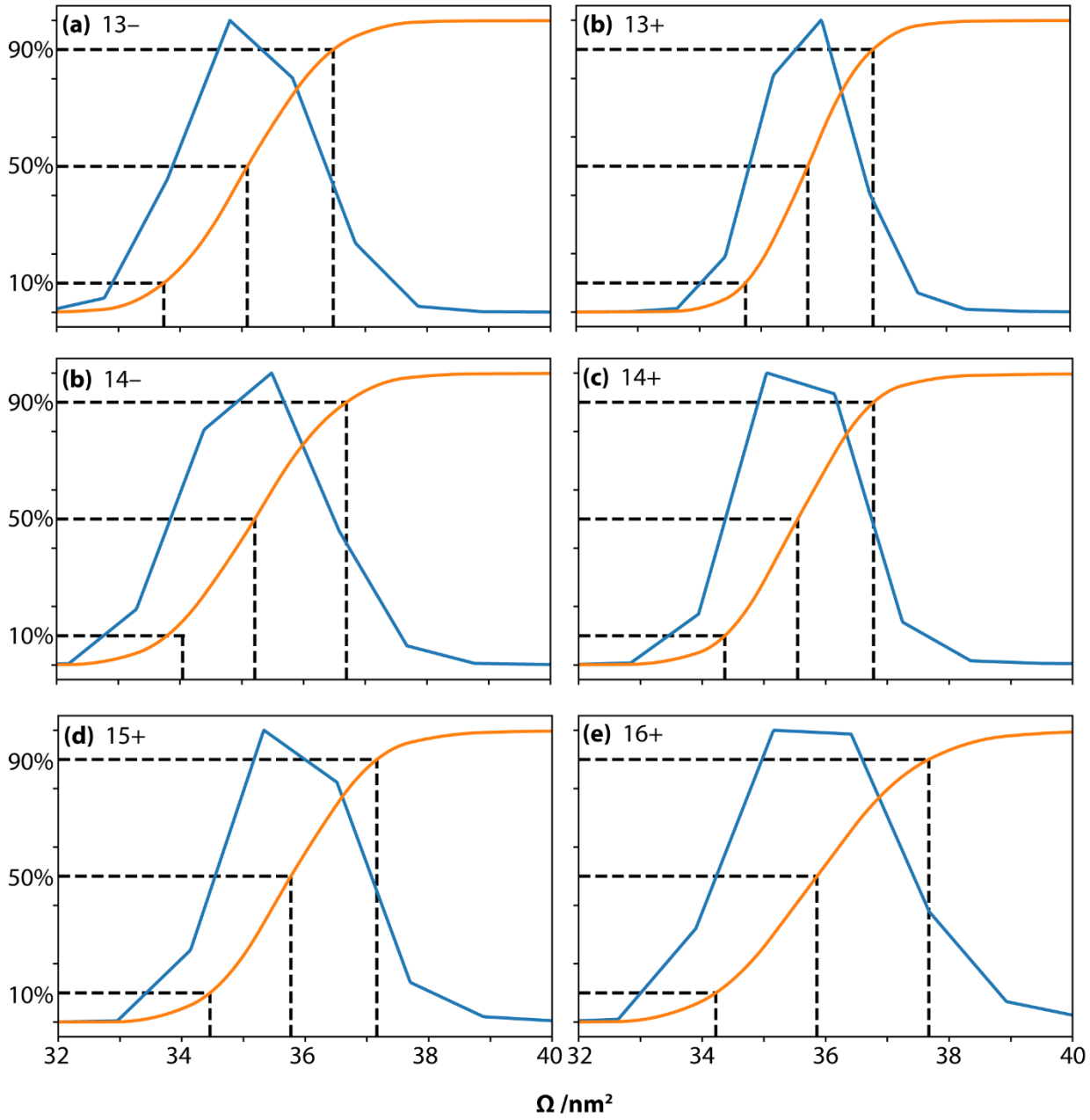

Figure S3.1. Apparent Ω distributions of avidin ions at low energy (*blue traces*) overlaid with the corresponding cumulative distribution functions (*orange traces*).

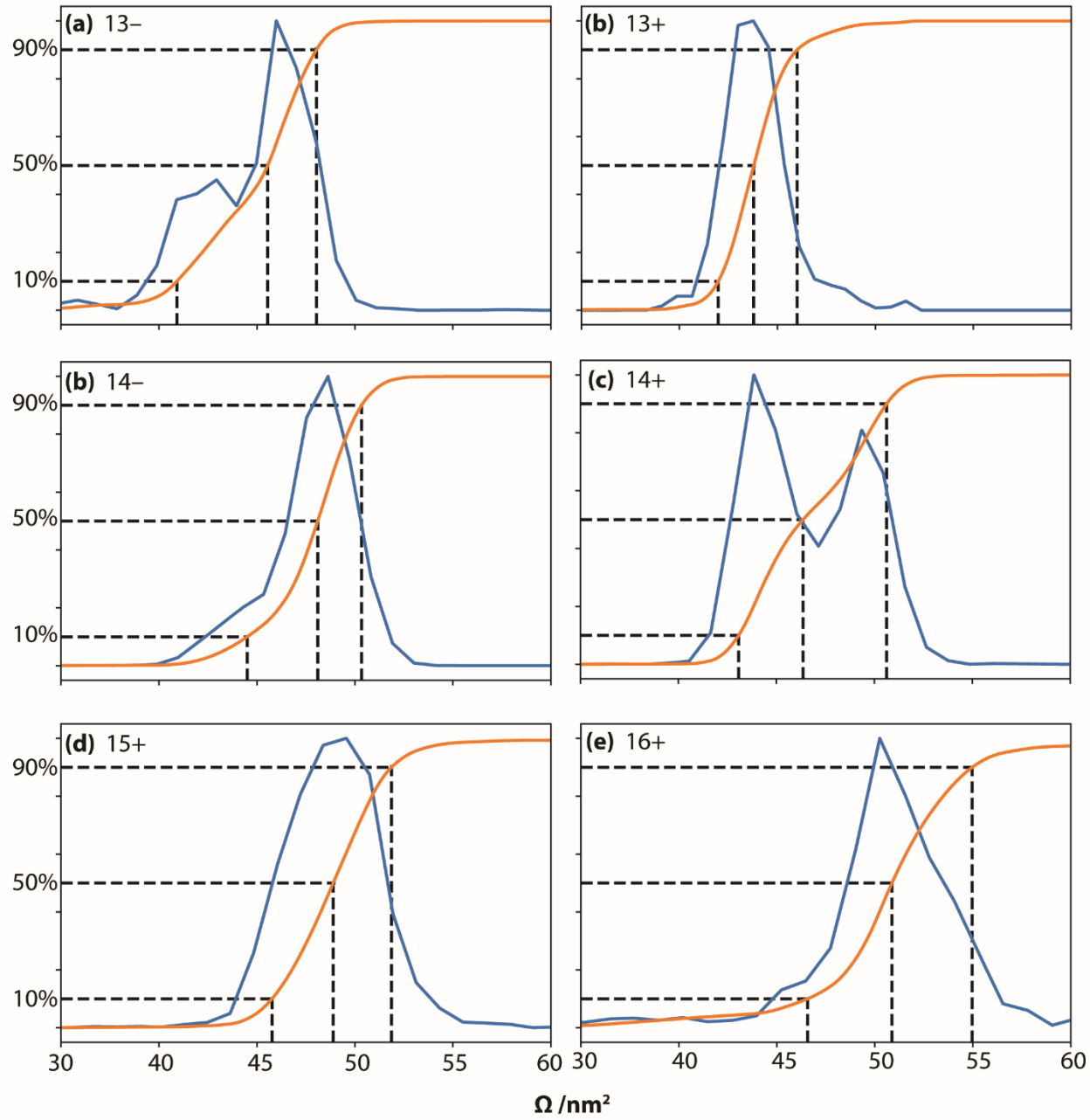

Figure S3.2. Apparent Ω distributions of avidin ions at high energy (*blue traces*) overlaid with the corresponding cumulative distribution functions (*orange traces*).

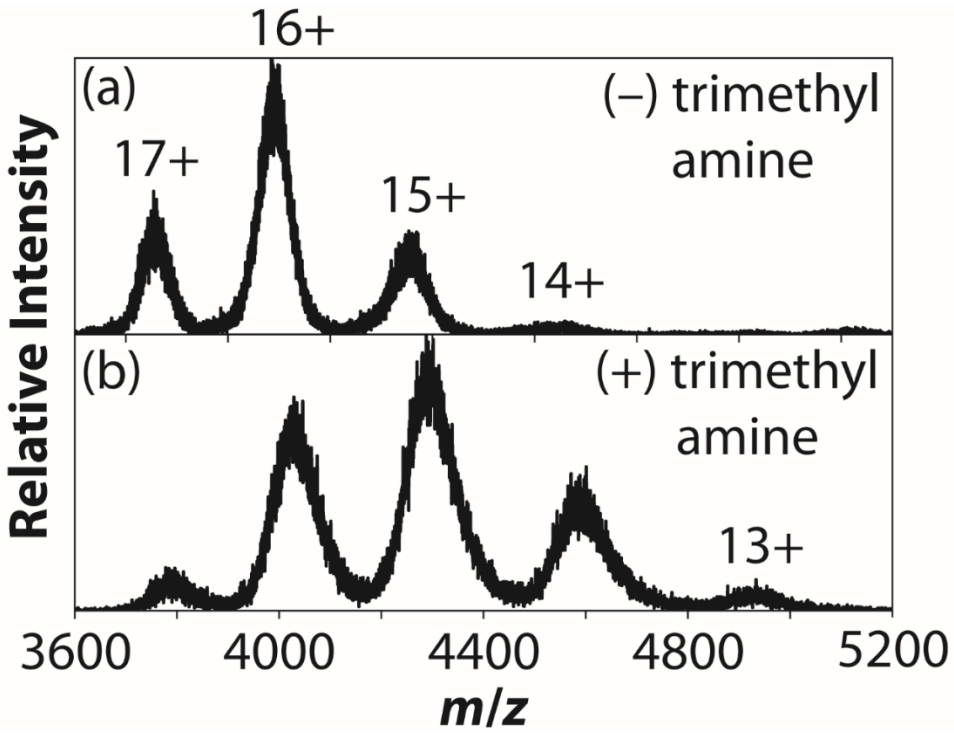

Figure S3.3. Mass spectra of avidin in positive ion mode obtained from solutions containing (a) 200 mM ammonium acetate at pH 7.0 and (b) 50 mM trimethylamine and 200 mM ammonium acetate.

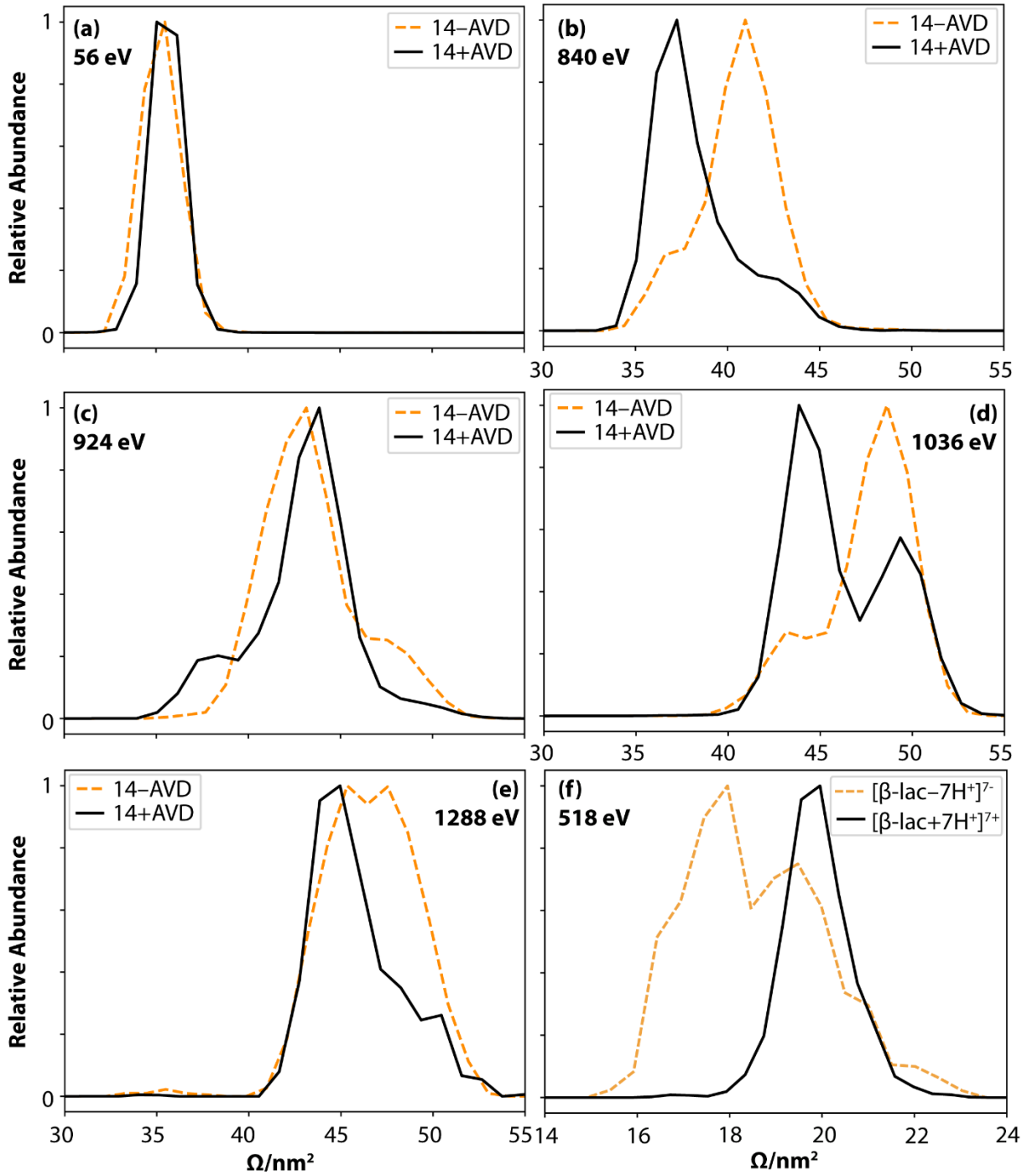

Figure S3.4. (a-e) Apparent Ω distributions of 14+ and 14– avidin at selected laboratory-frame energies. (f) Ω distributions of 7+ and 7– β-lactoglobulin monomer at a laboratory-frame energy of 518 eV.

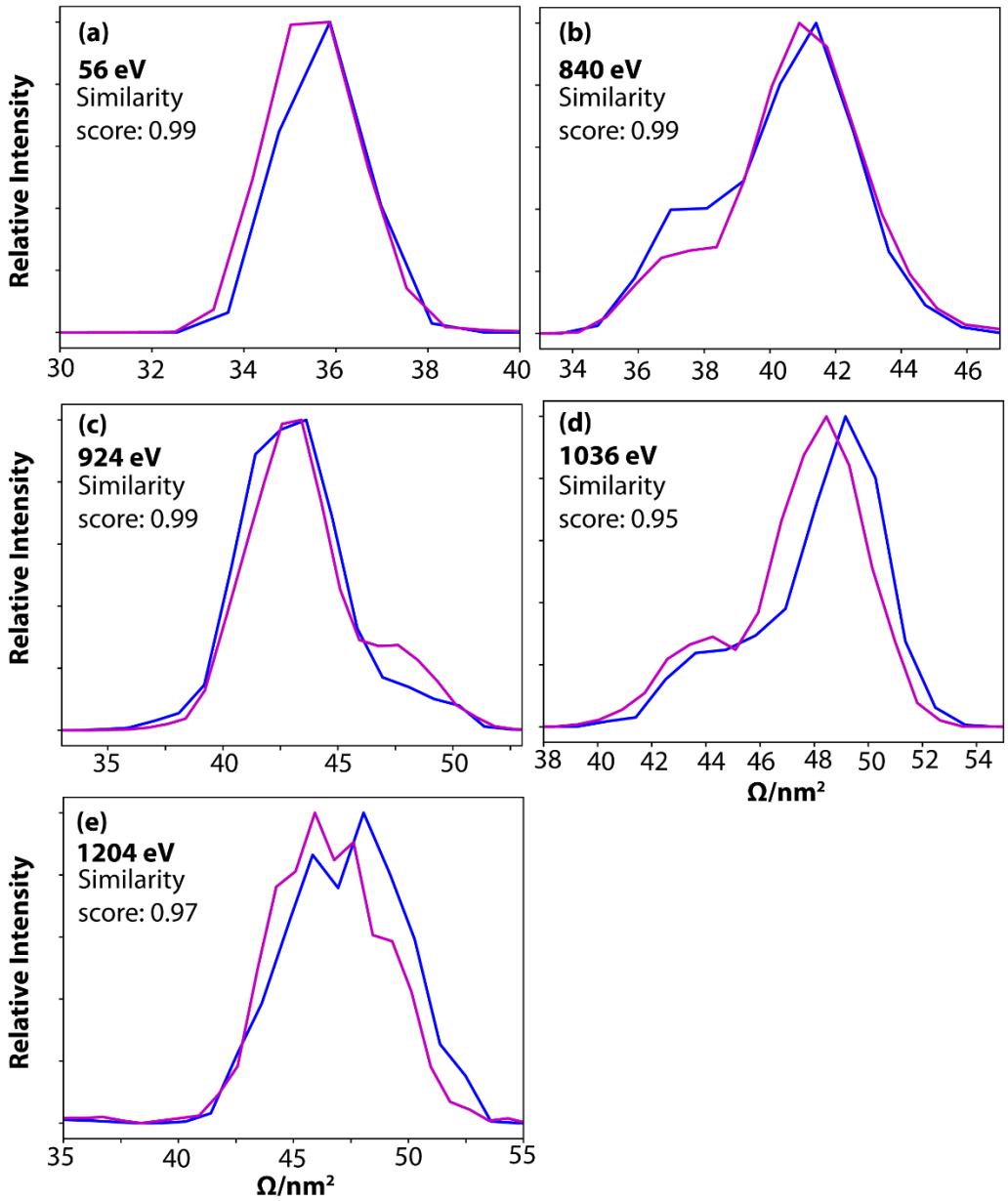

Figure S3.5. Apparent Ω distributions of 14− avidin at selected laboratory-frame energies. The *blue* and *purple* traces correspond to two technical replicates acquired on separate days.

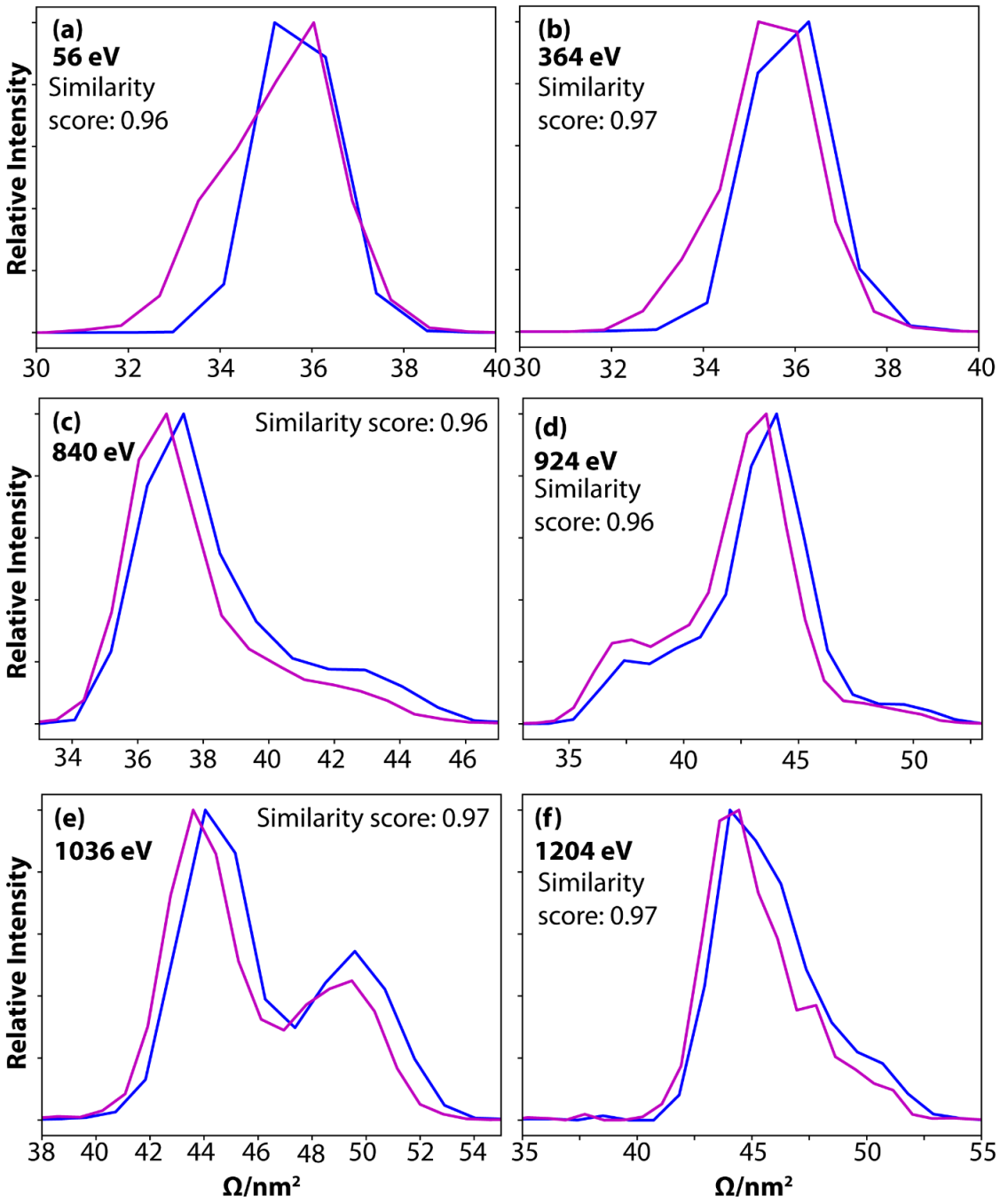

Figure S3.6. Apparent Ω distributions of 14+ avidin at selected laboratory-frame energies. The *blue* and *purple* traces correspond to two technical replicates acquired on separate days.

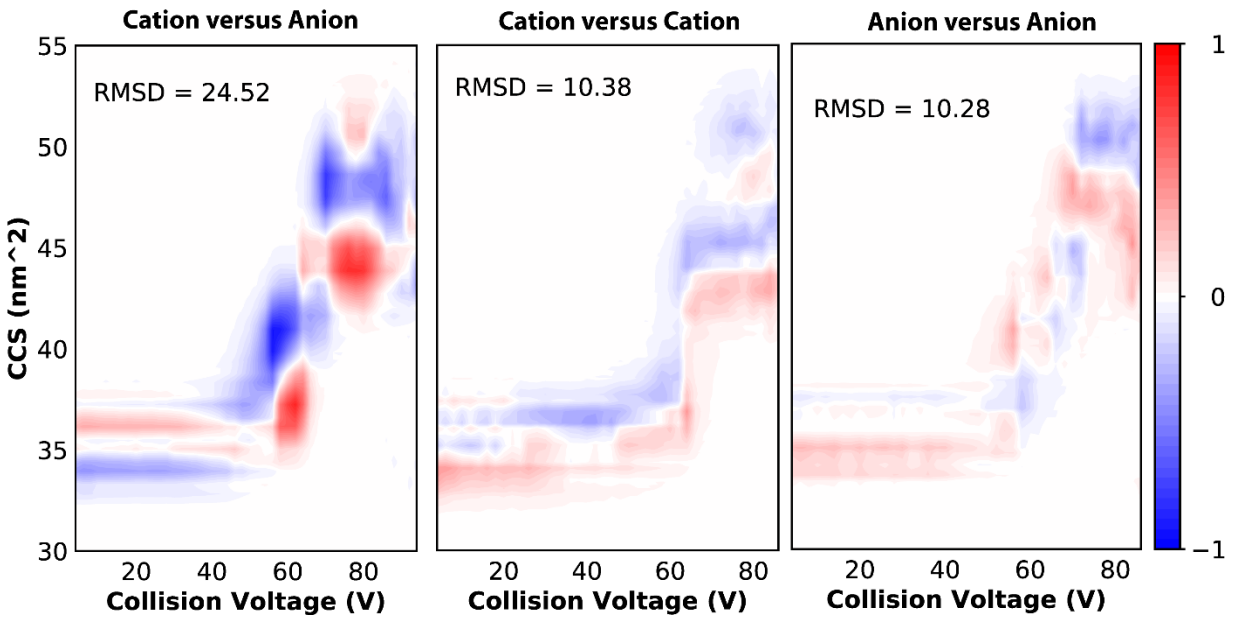

Figure S3.7. Comparison plots generated using CIU Suite 2 [38]. The plots were generated using the same experimental data as Figure 3.4. The default (no additional) smoothing was applied. The input files are normalized by CIU Suite 2 and is indicated by the color scale of +1 or −1.

38. Polasky, D.A., Dixit, S.M., Fantin, S.M., Ruotolo, B.T.: CIUSuite 2: Next-Generation Software for the Analysis of Gas-Phase Protein Unfolding Data. Anal. Chem. 91, 3147–3155 (2019). doi:10.1021/acs.analchem.8b05762

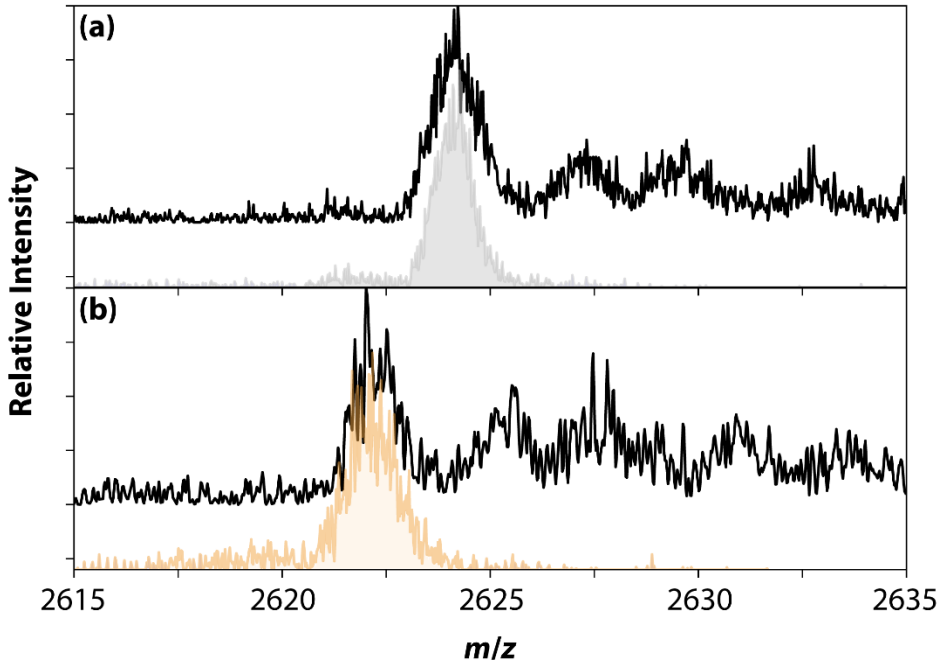

Figure S3.8. Native mass spectra (—) of β-lactoglobulin in positive (a) and negative (b) polarity. The unadducted 7+ (—, shaded) and 7– (—, shaded) β-lactoglobulin monomer at 28 eV were quadrupole selected and overlaid with the original mass spectra. Note that these spectra were not smoothed and are representative of those used for CIU analysis.

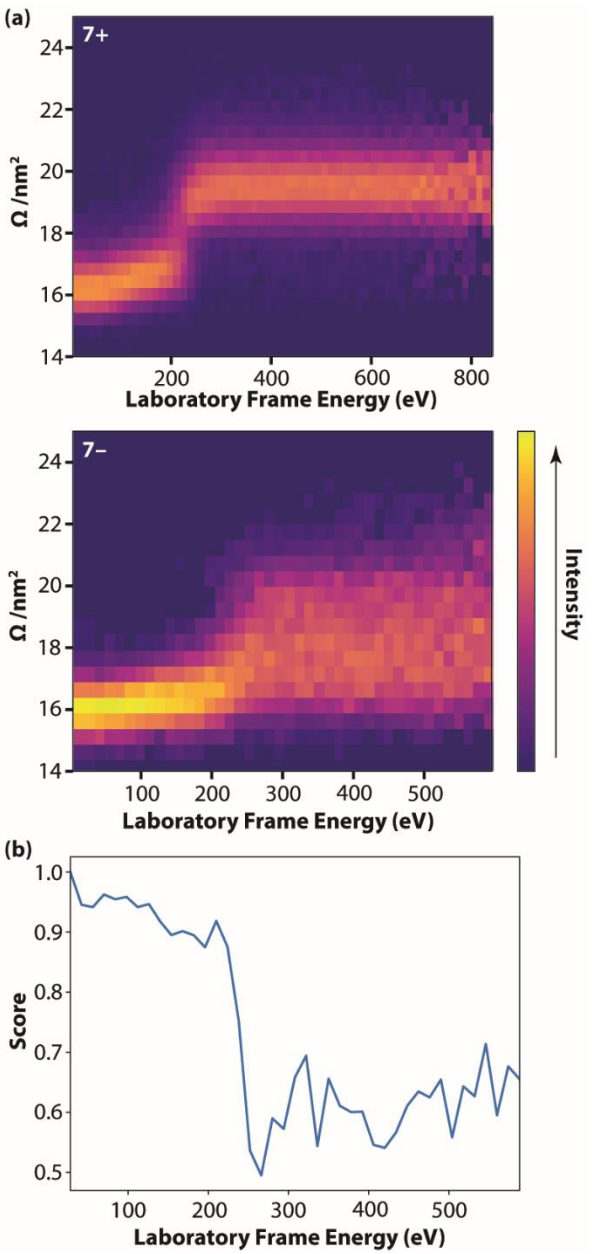

Figure S3.9. (a) CIU of 7+ and 7– β-lactoglobulin monomer. **Ω** distributions of the 7+ and 7– β-lactoglobulin monomer are shown as a function of laboratory frame energy. (b) Similarity score based on the results in (a).

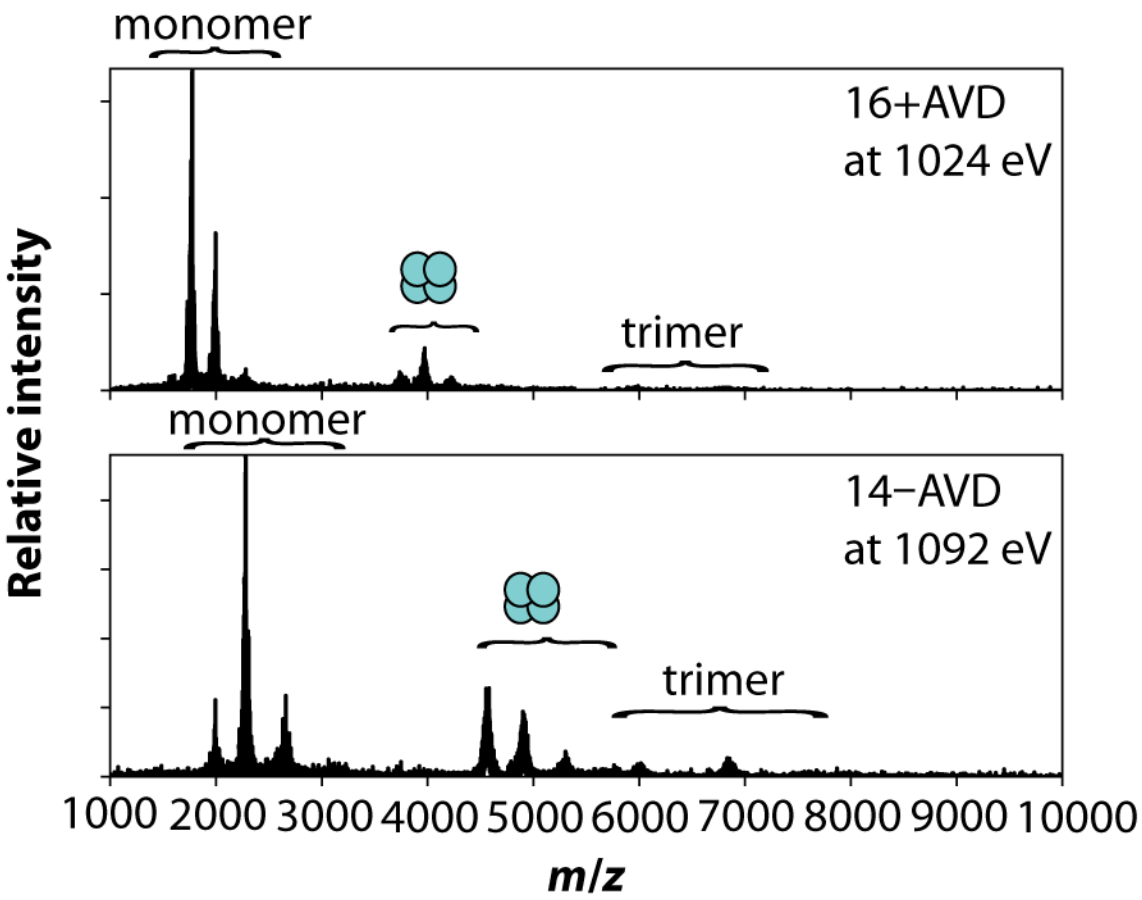

Figure S3.10. Collision-induced dissociation spectra acquired for 16+ avidin at (*top*, laboratory frame energy of 1024 eV) and 14– avidin (*bottom*, laboratory-frame energy of 1092 eV).

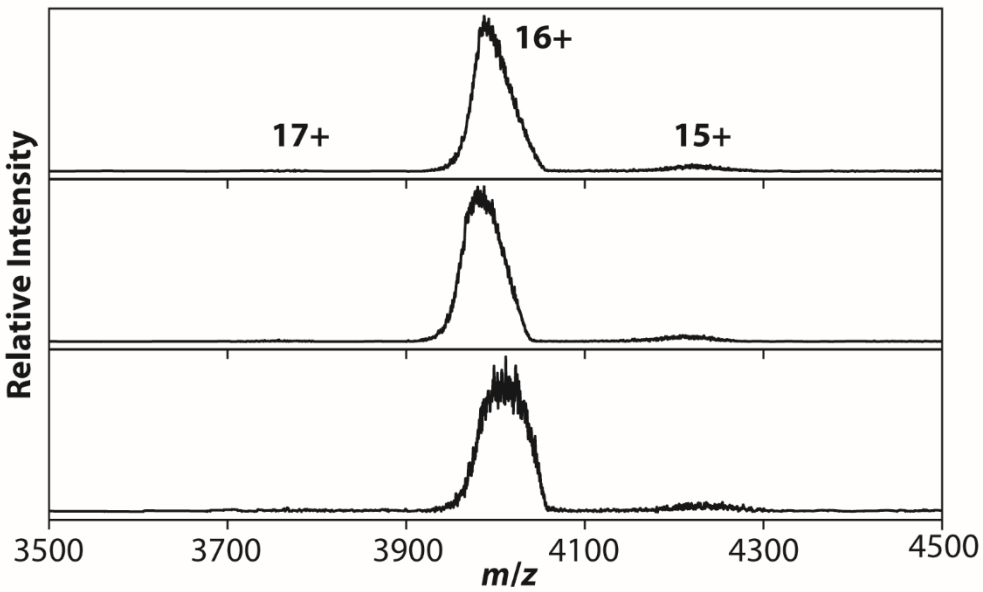

Figure S3.11. Quadrupole-selected 16+ avidin at low laboratory frame energy (320 eV). Each spectrum is an independent technical replicate.

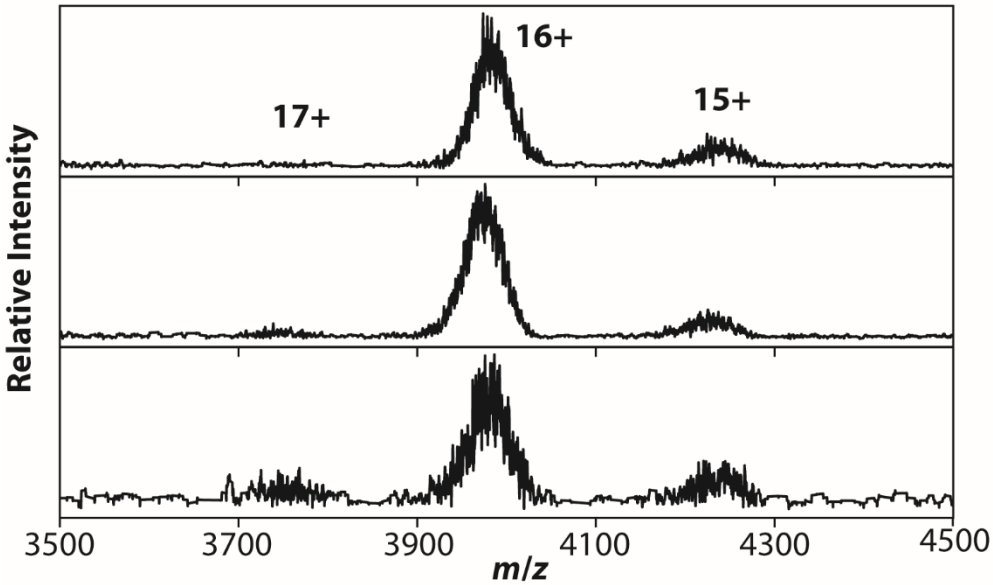

Figure S3.12. Quadrupole-selected 16+ avidin at high laboratory frame energy (1024 eV). Each spectrum is an independent technical replicate.

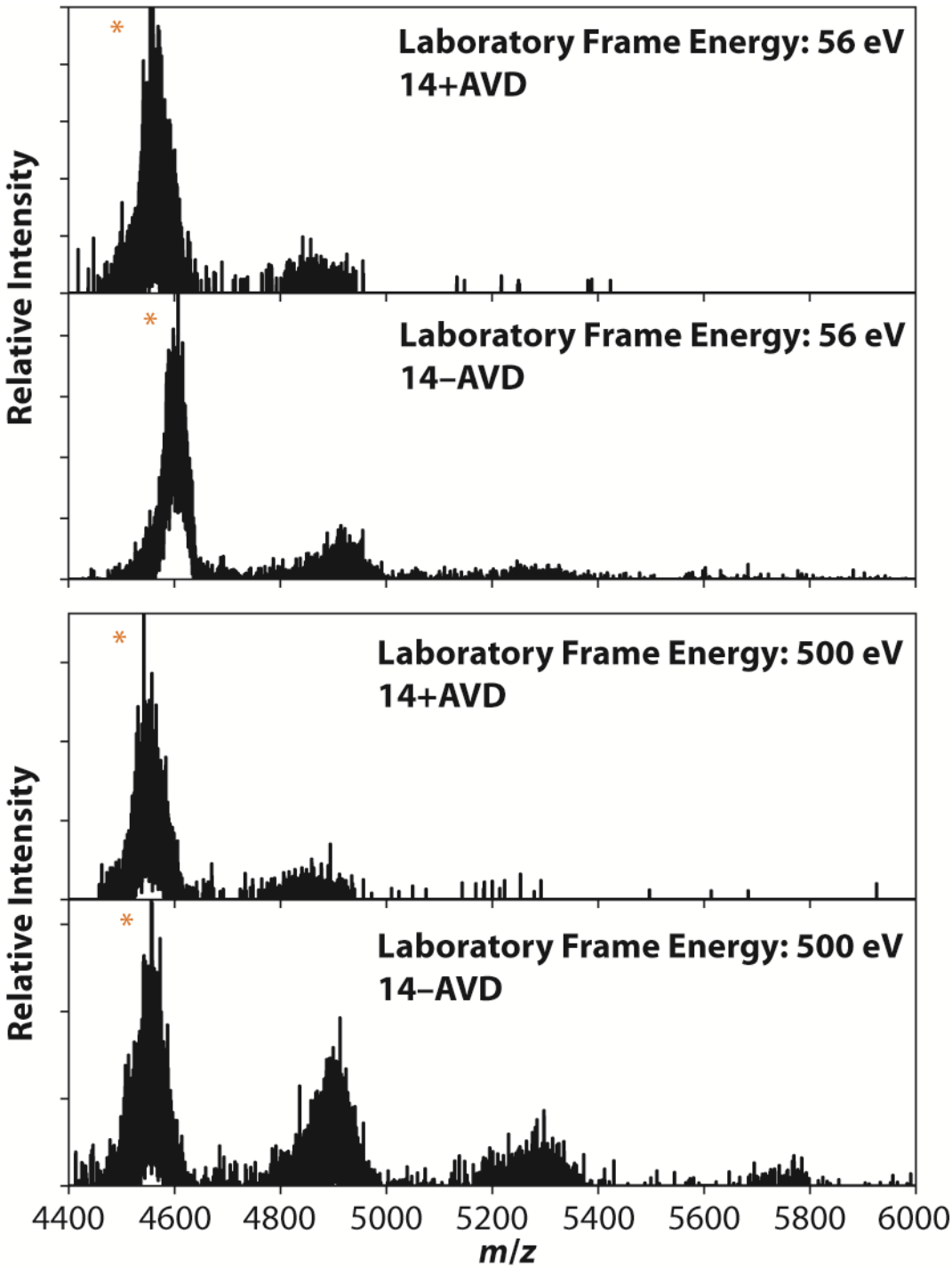

Figure S3.13. Mass spectra of 14+ and 14– avidin at 56 (top) and 500 (bottom) eV laboratory frame energy. The 14+ and 14– avidin ions are indicated with "*". Varying extents of charge-stripped avidin ions are also observed.

Appendix C

Supplemental Information for Chapter 4

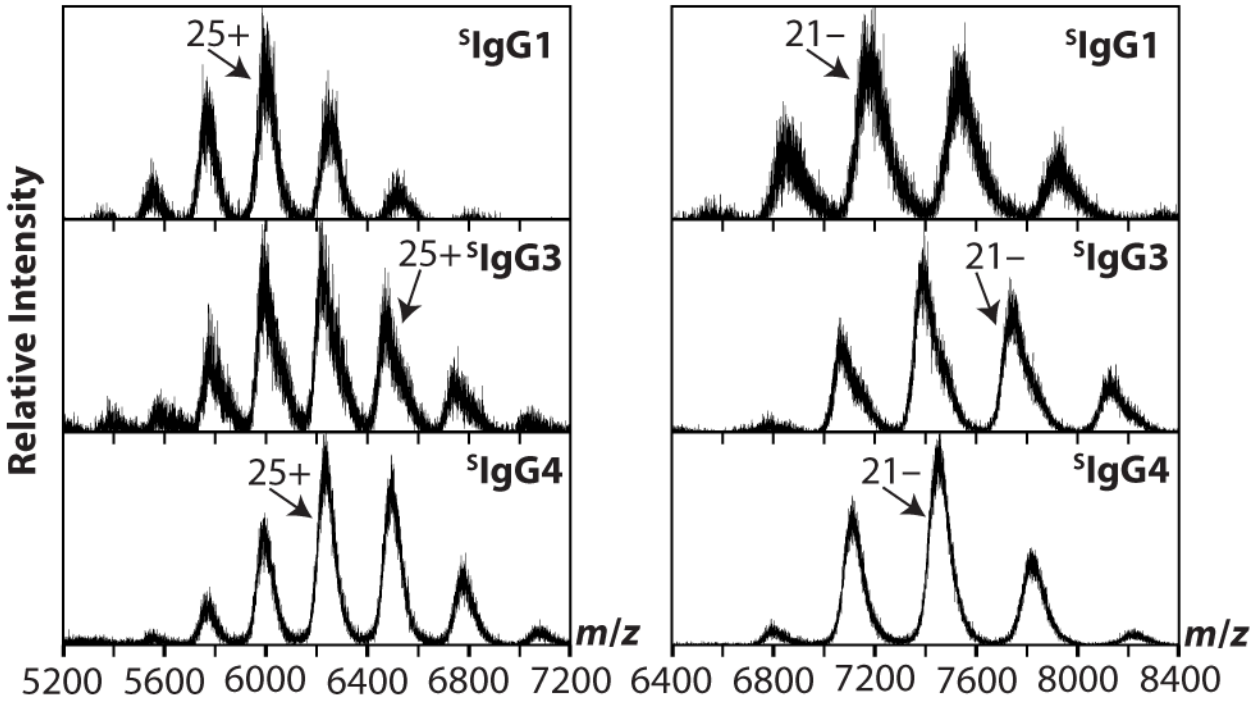

Figure S4.1. Native Mass of ^{S}IgG1, ^{S}IgG3 and ^{S}IgG4 in the positive (left) and negative (right) ion mode. The apparent mass of ^{S}IgG1, ^{S}IgG3 and ^{S}IgG4 correspond to 149, 162 and156 kDa respectively.

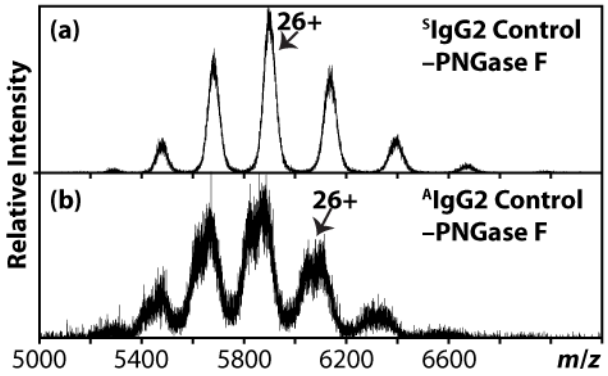

Figure S4.2. Control Mass Spectra of Deglycosylation of (a) ^{S}IgG2 and (b) ^{A}IgG2. The control samples of ^{S}IgG2 and ^{A}IgG2 were prepared using the same conditions for the deglycosylation (Figure 4.2) except the presence of PNGase F.

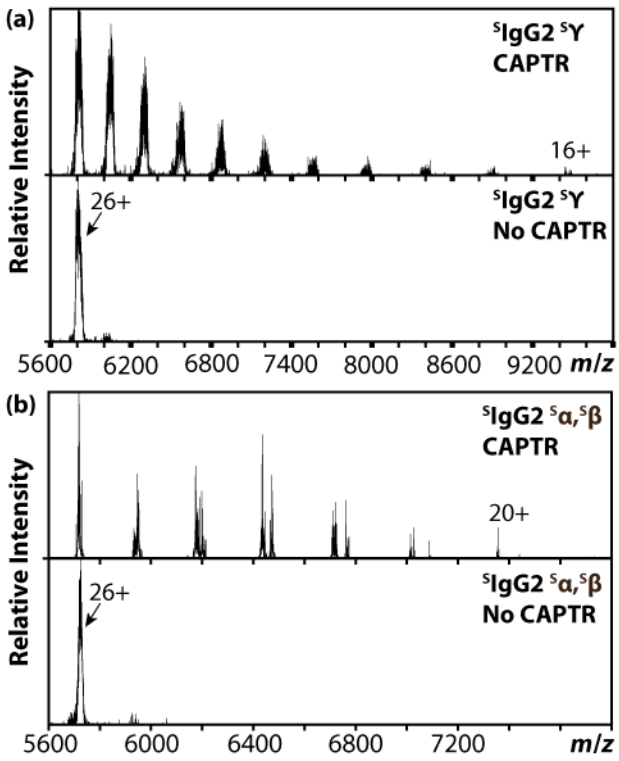

Figure S4.3. CAPTR MS of ^{S}IgG2. The top spectra of (a) and (b) correspond to the CAPTR spectrum of (a) * and (b) ● and ○ respectively. The bottom spectra demonstrate the selection of the precursor peaks for the CAPTR of (a) * and (b) ● and ○ respectively.

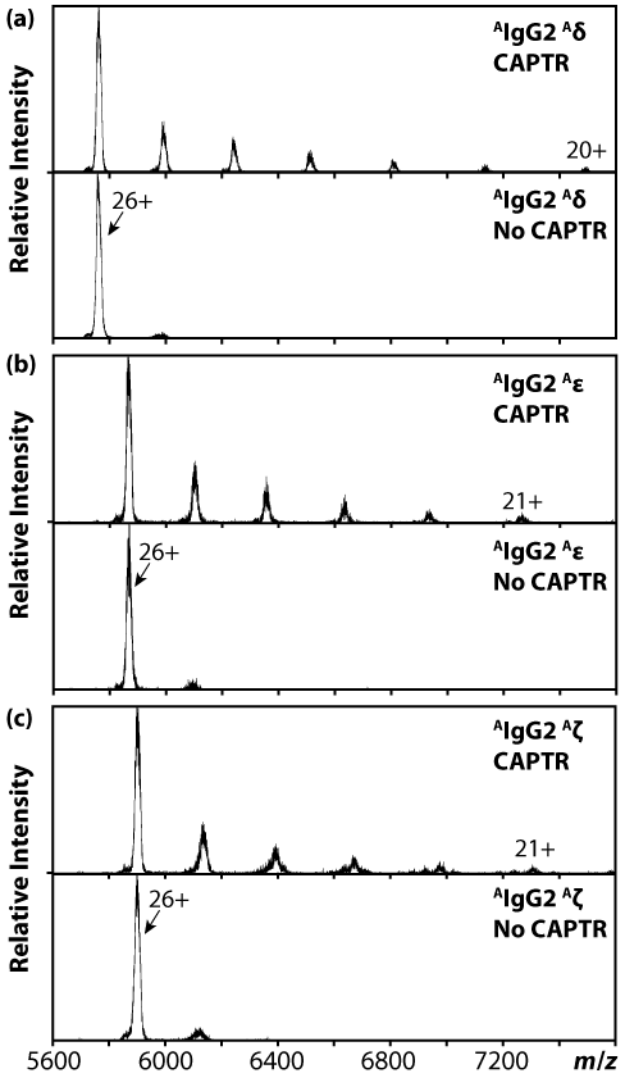

Figure S4.4. CAPTR MS of ^{A}IgG2. The top spectra of (a), (b) and (c) demonstrate the CAPTR spectra of #, Δ and ◊ respectively. The bottom spectra indicate the selection of the CAPTR precursors for the respective top spectra.

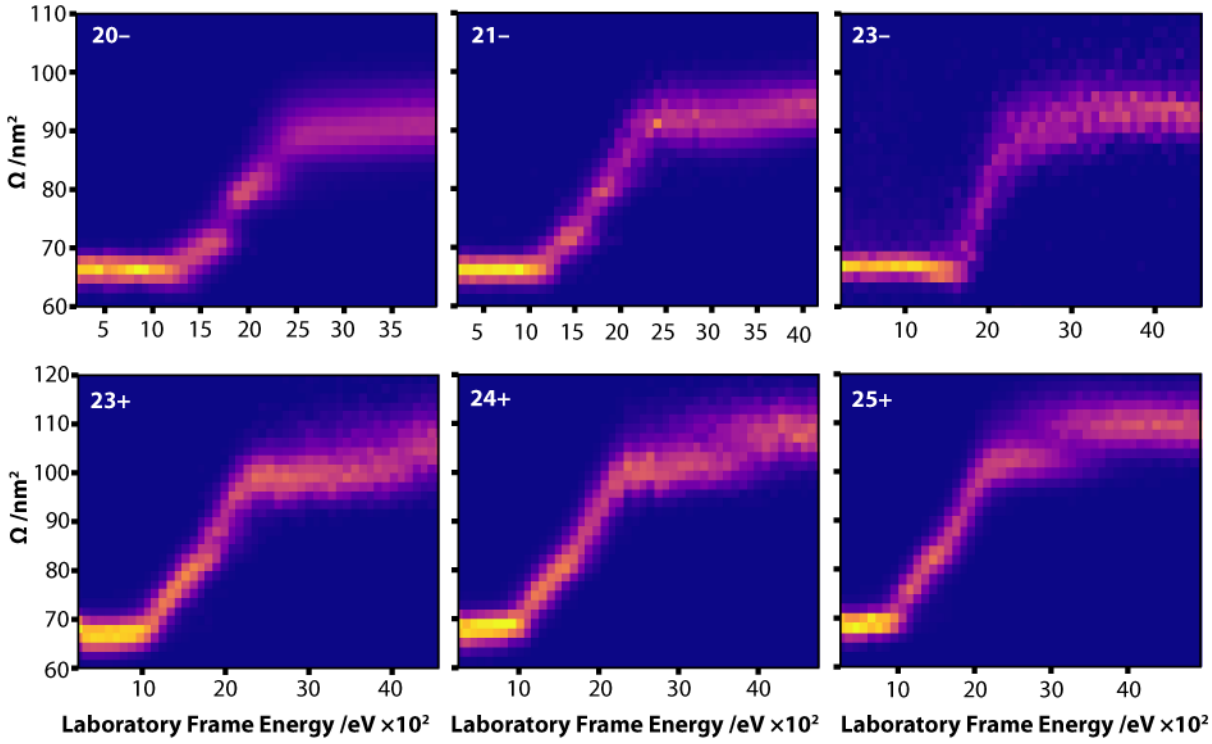

Figure S4.5. CIU of native ADH. The heatmap exhibits apparent Ω distributions as a function of laboratory frame energy in 4 V increment from 10 – 198 V.

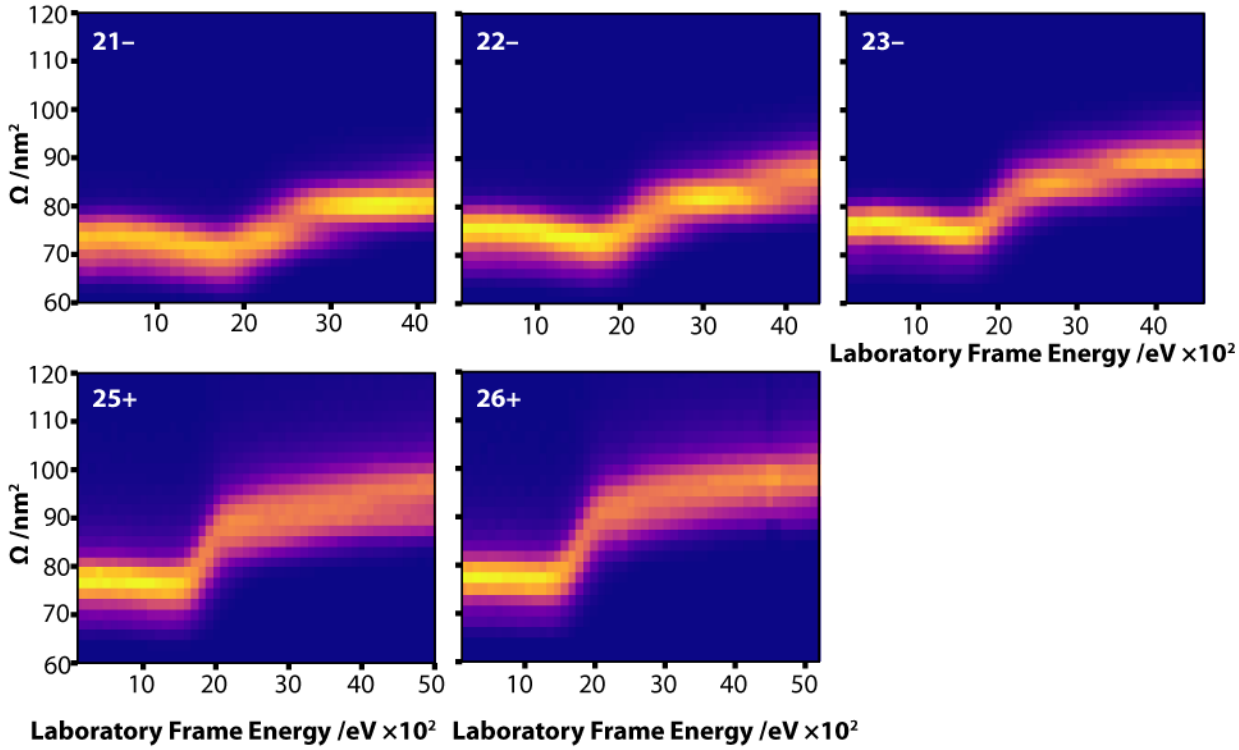

Figure S4.6. CIU of native-like ^{A}IgG2. The heatmap exhibits apparent **Ω** distributions as a function of laboratory frame energy in 4 V increment from 4 – 200 V.

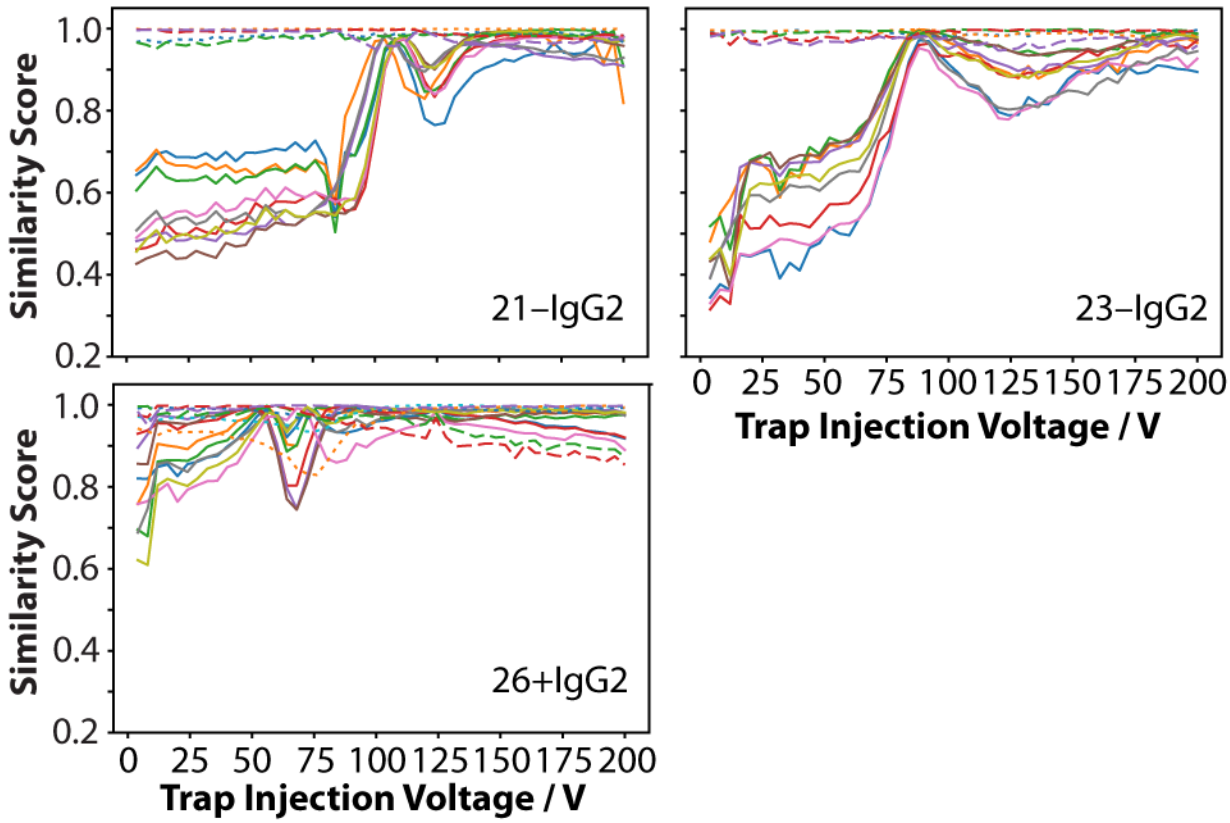

Figure S4.7. Similarity score of 21−, 23− and 26+ ^{S}IgG2 and ^{A}IgG2. The comparison between ^{S}IgG2 and ^{A}IgG2 are indicated by the solid lines. The technical replicates of ^{S}IgG2 and ^{A}IgG2 are indicated by dashed (---) and dotted (···) lines respectively.

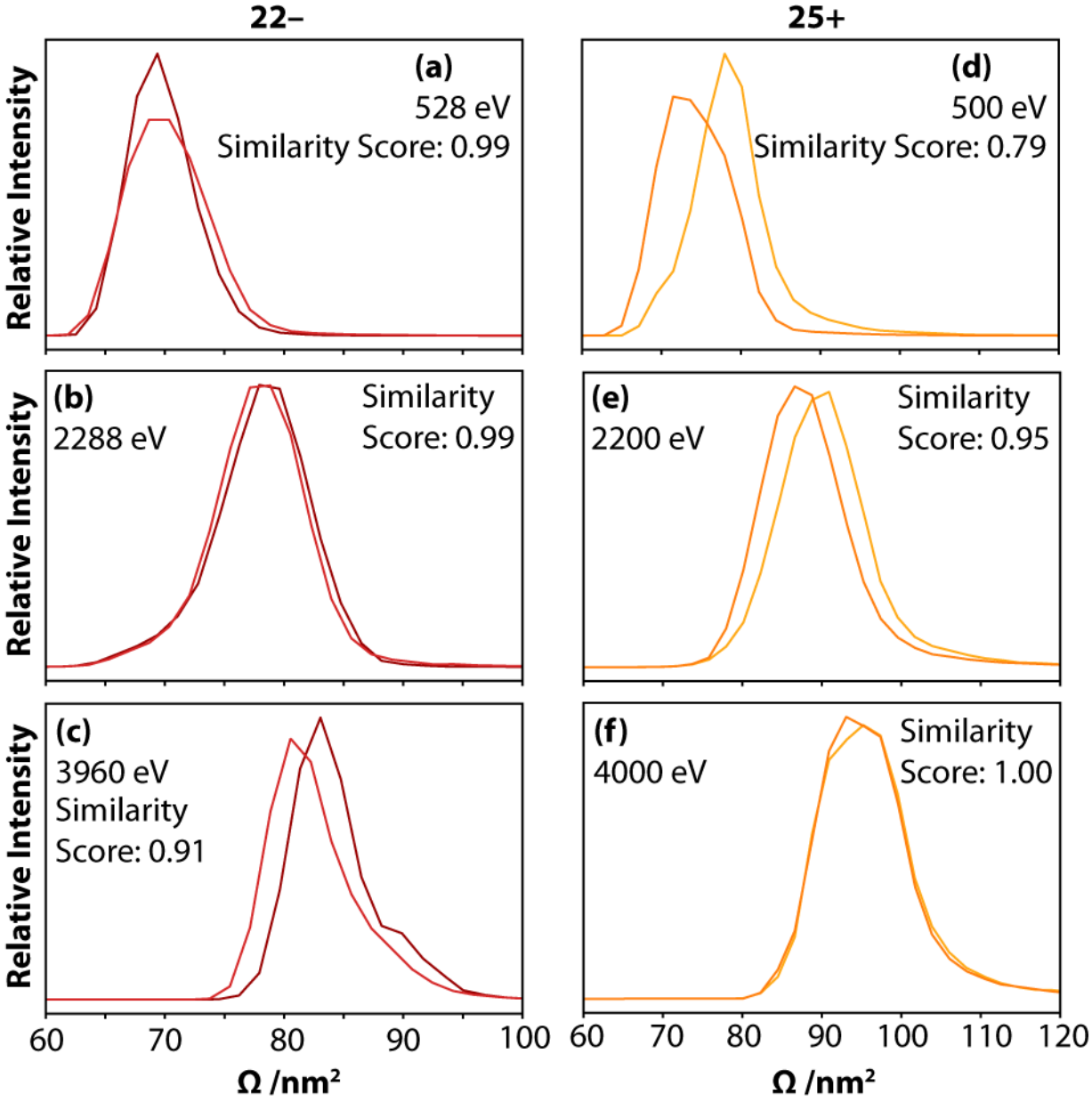

Figure S4.8. (a – c) the individual Ω distributions of the technical replicates of ^{S}IgG2 (---) that exhibited decrease in the similarity score at the high energy range (Figure 4.6a). (d – f) the individual Ω distributions of the technical replicates of ^{A}IgG2 (---) that exhibited the lowest similarity score amongst the comparisons of replicates at the low energy range (Figure 4.6b).

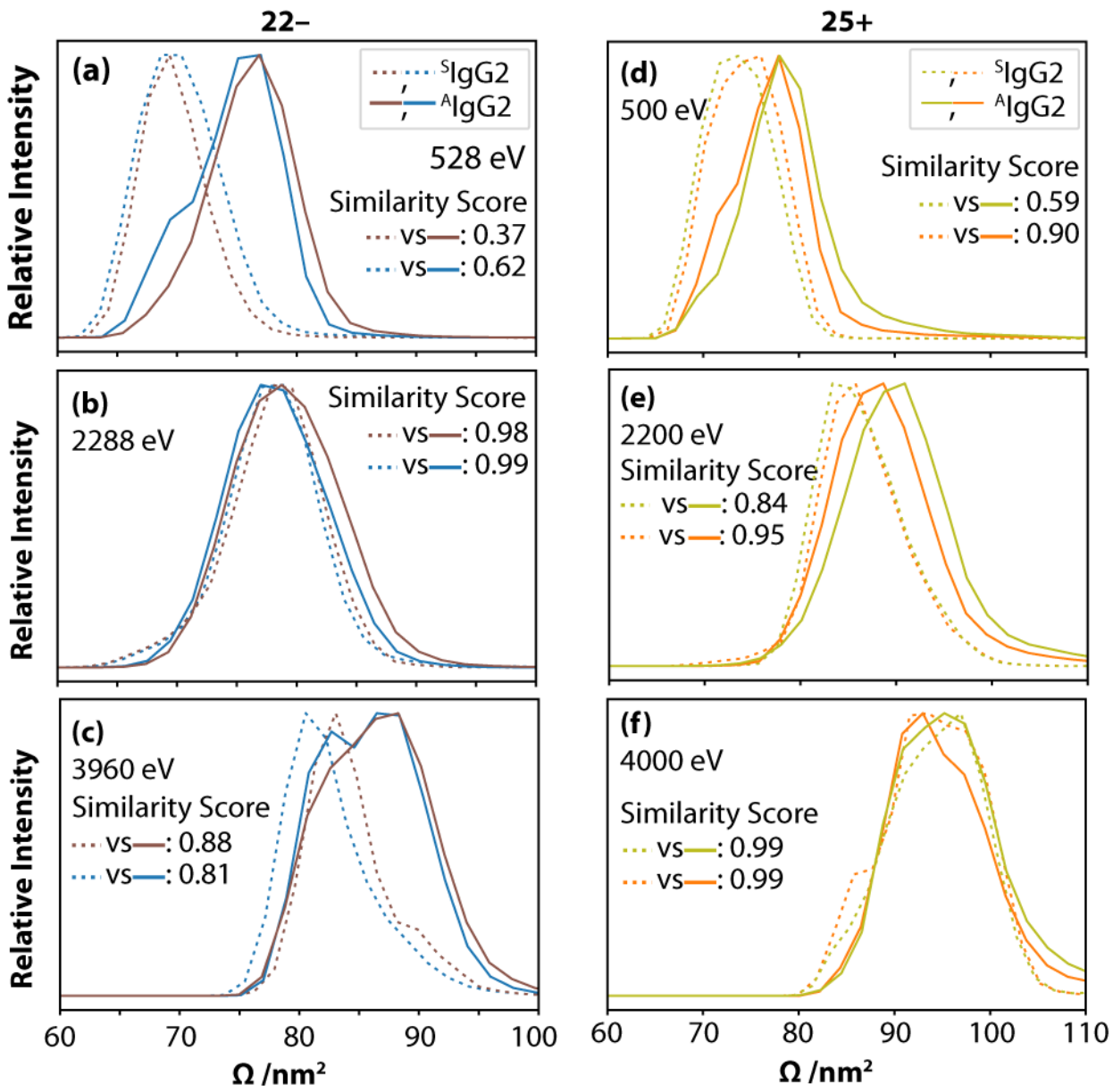

Figure S4.9. (a – c) Individual Ω Distributions Comparing 22– ^{S}IgG2 and ^{A}IgG2 corresponding to the lowest and highest similarity score (Figure 4.6a). (d – f) Individual Ω Distributions Comparing 25+ ^{S}IgG2 and ^{A}IgG2 corresponding to the lowest and highest similarity score (Figure 4.6b).

Appendix D

Supplemental Information for Chapter 5

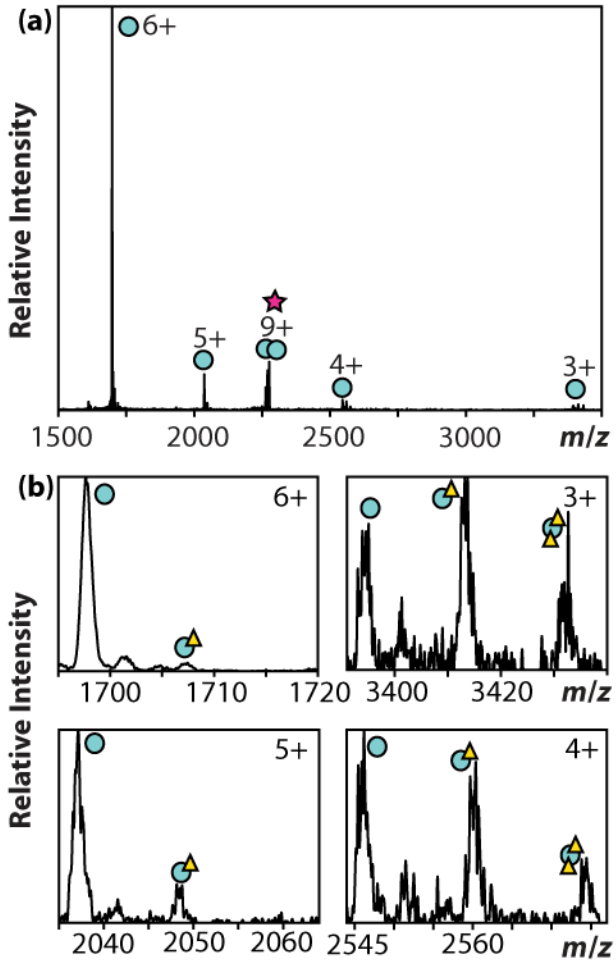

Figure S5.1. (a) The overall mass spectrum during the CID of the 9+ ACD dimers (●●) at 495 eV. (b) The 6+ and 3+ and 5+ and 4+ product monomers (●) generated by the CID of the precursor at 495 eV. Intact Ni(II) ions are indicated with by ▲.